**TECHNISCHE
UNIVERSITÄT
WIEN**
Vienna | Austria

Dissertation

A Density Functional Theory Study Of Defects In Large Gap Insulators

Ausgeführt zum Zwecke der Erlangung des akademischen Grades eines Doktors der Naturwissenschaften unter der Leitung von

Ao.Univ.Prof.i.R. Dipl.-Ing. Dr.techn. Peter Mohn und
Univ.Prof. Dipl.-Phys. Dr.rer.nat. Thorsten Schumm

am Center for Computational Materials Science

eingereicht an der Technischen Universität Wien
Fakultät für Physik

von

Dipl.-Ing. Martin Pimon

am 7. Oktober 2021

Acknowledgements

My sincere appreciations go to all who supported me on the journey towards finishing this thesis. First and foremost my supervisors Peter Mohn and Thorsten Schumm were perpetually aiding me in my physical understanding and also encouraging me to persevere. I always felt to be in good hands and for that I am truly thankful. I am also grateful for all my colleagues and friends in the office who made the working environment exciting and fun, especially Alex, Dilan, Jakub, Johannes, Matthias, Michael, Niklas, Paul, Thomas and Wernfried, and for the collaboration with Brenden and Georgy. When the pandemic caused a sudden and drastic change to our work habits my friend Visa helped me continuously in finding novel workflows. In addition I want to thank my whole family for their support, in particular my parents Edith and Norbert, my fiancée Esther and our son Emil. I consider myself very lucky to be able to count on such a strong network of caring people.

On a technical note, my acknowledgements go to the TU Wien and the VSC team for providing reliable research and computing infrastructure, to the VASP team for producing their excellent simulation package, to Stack Exchange for answering (almost) every question anyone can ever have and to all developers contributing to free and open source software, where the small selection in the following was used extensively and some being indispensable for the production of this thesis: Manjaro Linux, Vim, Python, GFortran, Taskwarrior, Firefox, Libreoffice, VESTA, GIMP and LaTeX including many of its countless and useful packages, notably TikZ and PGFPlots.

Abstract

For the experimental realization of a novel type of nuclear clock we investigate the large gap insulators MgF_2, CaF_2 and $LiCaAlF_6$ with density functional theory. In particular we determine possible charge compensation mechanisms when doped with thorium and estimate the band gap size, which we find to be in range of the thorium-229 isomer energy for $Th:CaF_2$ and for $Th:LiCaAlF_6$. To establish an assessment on the transition rate of a proposed electron-bridge mechanism, we reconstruct the all-electron Kohn-Sham wave functions for the most probable charge compensating configurations of these two compounds. For $Th:CaF_2$, lattice vibrations at finite temperatures were also taken into account and we include an analysis when doped with the more accessible heavy elements actinium, cerium and neptunium and calculate the electric field gradient on these dopants. For $Th:LiCaAlF_6$, we furthermore train the structure to energy mapping with an artificial neural network using atom centered symmetry functions.

Kurzfassung

Für die experimentelle Realisierung einer neuartigen Atomuhr untersuchen wir die Materialien MgF_2, CaF_2 und $LiCaAlF_6$ mit Hilfe der Dichtefunktionaltheorie. Insbesondere bestimmen wir mögliche Ladungskompensationsmechanismen bei einer Dotierung mit Thorium und schätzen die Größe der Bandlücke, die wir im Bereich der Anregungsenergie des Thorium-229 Isomers für $Th:CaF_2$ und $Th:LiCaAlF_6$ befinden. Um eine Einschätzung für die Übergangsrate eines möglichen Elektronen-Brücken Mechanismus zu ermöglichen, rekonstruieren wir die vollelektronischen Kohn-Sham Wellenfunktionen für die wahrscheinlichsten Ladungskompensationsmechanismen dieser beiden Verbindungen. Für $Th:CaF_2$ werden auch Gitterschwingungen bei erhöhten Temperaturen berücksichtigt und wir analysieren Dotierungen mit den leichter zugänglichen schweren Elementen Actinium, Cer und Neptunium und berechnen den elektrischen Feldgradienten an diesen Dotanden. Für $Th:LiCaAlF_6$ trainieren wir außerdem die Struktur-zu-Energie Beziehung mittels eines neuronalen Netzwerks mit Hilfe von atomzentrierten Symmetriefunktionen.

Contents

Chapter 1

Introduction

Measuring time to high accuracy is a central demand of modern physics.[1–3] With setups where electronic excitations are used as frequency standards, recent developments made time measurements with unprecedented uncertainties possible.[4] However, by exploiting the low energy isomer excitation of the ^{229}Th nucleus, a novel nuclear clock has been proposed, that may outperform even the most accurate time measurements to date.[5,6] This is because the active atom is implanted in a crystalline lattice of a large gap insulator, which will allow for longer and more stable measurements, while at the same time the electronic environment shields the nucleus from external perturbations. Recent measurements estimate an energy difference of 8.10(17) eV to the ground state, which is in reach of modern optical laser spectroscopy methods making its excitation potentially experimentally viable.[7] A critical component for the feasibility is that the host crystal's band gap exceeds the predicted isomer energy.

In the present thesis we study the electronic structure and optical properties of thorium atoms (and a number of other heavy elements) introduced into large gap insulators like MgF_2, CaF_2 and $LiCaAlF_6$.[8–12] These numerical simulations are performed with the Vienna Ab-initio Simulation Package (VASP).[13–17]

A systematic study of impurities and the necessary charge compensation mechanisms requires the calculation of enthalpies for all possible compounds of the constituents which appear along the chemical pathways when introducing one or more atoms into a crystal and simultaneously removing atoms to provide charge neutrality.

To this end we perform a large number of convergence studies testing various versions of pseudopotentials and phases at different levels of density functional theory (DFT). These convergence studies include the numerical accuracy of the VASP calculations, the convergence of the grid in reciprocal space and the calculation of the equilibrium geometries.

Our study on $LiCaAlF_6$ (LICAF) represents a peculiar case. As a quaternary compound with a trigonal lattice structure,[18] any straightforward strategy to scan for possible charge compensation mechanisms is doomed to fail due to the laws of combinatorics. To overcome these problems we study the potential application of artificial neural networks to sort out unlikely configurations. We follow a previously devised approach to calculate a unique atomic fingerprint in the chemical environment, which we modify to enhance the accuracy in a crystal lattice.[19]

In the case of $Th:CaF_2$ we also study the influence of finite temperature effects on its optical properties via the calculation of the phonon spectrum.

A possibility to excite the isomer transition is the electron-bridge mechanism. The idea behind is that parts of the wave functions reach all the way to the nucleus such that an electronic excitation can transfer its energy. We thus calculate the respective wave functions which we provide for the research group of Adriana Pálffy at the Max-Planck-Institut für Kernphysik in Heidelberg, who perform the calculations of the above mentioned scheme.[20,21]

Finally, we provide calculations of the electric field gradient at the thorium site to facilitate experiments with nuclear quadrupole resonance spectra, which allow to discriminate between the ground state and the excited state of the thorium nucleus.

Part I

Theory

Chapter 2

Insulating Crystals

2.1 Bloch Waves

In the early twentieth-century, diffraction experiments with X-rays revealed that crystals show a periodic atomic structure. This discovery was so significant, that two subsequent Nobel prizes were awarded in 1914[22] and 1915.[23]

In nature, most elements and inorganic compounds are solids at ordinary temperatures and a great majority of those also show a periodic structure in space,[24] in the same way as crystals do. The periodicity is given by the three lattice vectors $\mathbf{a}_1$, $\mathbf{a}_2$ and $\mathbf{a}_3$. Naturally, physical quantities with spatial dependence show the same periodicity with respect to $\mathbf{R} = n_1\mathbf{a}_1 + n_2\mathbf{a}_2 + n_3\mathbf{a}_3$, $n_i \in \mathbb{Z}$. For example, the crystal potential energy is invariant under translations $V(\mathbf{r}) = V(\mathbf{r} + \mathbf{R})$. Because of this periodicity, the potential can be expanded into a Fourier series

$$V(\mathbf{r}) = \sum_{\mathbf{K}} V_{\mathbf{K}} e^{i\mathbf{K}\cdot\mathbf{r}}, \tag{2.1}$$

where $\mathbf{K} = \eta_1\mathbf{b}_1 + \eta_2\mathbf{b}_2 + \eta_3\mathbf{b}_3$, $\eta_i \in \mathbb{Z}$ is an integer multiple of the reciprocal lattice vectors $\mathbf{b}_1$, $\mathbf{b}_2$ and $\mathbf{b}_3$ and $V_{\mathbf{K}}$ are the expansion coefficients.

In the following we consider the solution to the Schrödinger equation

$$\left(-\frac{\hbar^2}{2m_e}\nabla^2 + V(\mathbf{r})\right)\Psi_n(\mathbf{r}) = E_n\Psi_n(\mathbf{r}). \tag{2.2}$$

For a given potential V we want to obtain the electronic wave function for a fixed point in time. This case is sufficient as is discussed within the Born-Oppenheimer approximation in section 2.3.

A general ansatz to solve the Schrödinger equation for the given periodic

potential is to expand the wave function into plane waves

$$\Psi_n(\mathbf{r}) = \sum_{\mathbf{k}} C_{\mathbf{k}} e^{i\mathbf{k}\cdot\mathbf{r}}, \tag{2.3}$$

where the $\mathbf{k}$ vectors are determined by the boundary conditions. Plugging both Equation 2.1 and Equation 2.3 into Equation 2.2 results in

$$\left(\frac{\hbar^2 k^2}{2m_e} - E\right) C_{\mathbf{k}} + \sum_{\mathbf{K}} V_{\mathbf{K}} C_{\mathbf{k}-\mathbf{K}} = 0, \tag{2.4}$$

after short calculation.[25,26] Each solution for $\mathbf{k}$ has a coupling of coefficients of $C_{\mathbf{k}}$ and all those which differ by a reciprocal lattice vector $C_{\mathbf{k}-\mathbf{K}}$, $C_{\mathbf{k}-\mathbf{K}'}$, $C_{\mathbf{k}-\mathbf{K}''}$, etc. With this information, we can re-write Equation 2.3 as

$$\begin{aligned}\Psi_{\mathbf{k}}(\mathbf{r}) &= \sum_{\mathbf{K}} C_{\mathbf{k}-\mathbf{K}} e^{i(\mathbf{k}-\mathbf{K})\cdot\mathbf{r}} \\ &= u_{\mathbf{k}}(\mathbf{r}) e^{i\mathbf{k}\cdot\mathbf{r}}.\end{aligned} \tag{2.5}$$

This result is known as Bloch's Theorem, which states that the electronic wave functions in crystals are plane waves multiplied by a function, which has the same periodicity as the crystal $u(\mathbf{r}) = u(\mathbf{r} + \mathbf{R})$ since it can be seen as a Fourier expansion with the reciprocal lattice vectors $\mathbf{K}$.

One of many implications of Bloch's Theorem is that

$$\Psi_{\mathbf{k}+\mathbf{K}}(\mathbf{r}) = \Psi_{\mathbf{k}}(\mathbf{r}). \tag{2.6}$$

Thus, values of $\mathbf{k}$ are not unique and may be chosen such that they are within the first Brillouin zone. Consequently, the energies are periodic with respect to the reciprocal lattice

$$E_n(\mathbf{k}) = E_n(\mathbf{k} + \mathbf{K}_n). \tag{2.7}$$

The periodicity of energy states in reciprocal space combined with the quantization of energy levels result in so-called energy bands, where certain ranges of energies are populated by electrons while other ranges are not. These forbidden energy regimes are called band gaps. The collective energy bands form the band structure of a material.[25,27] In a first approximation, a mathematical origin for the band gaps is derived in section 2.2.

2.2 Band Structure

Interpreting band structures requires knowledge of the physical mechanisms which can occur in the material. As an example, we first look at a potential

5

which is periodic but infinitely small. In this approximation, the electrons are free and non-interacting. Using Equation 2.7, the dispersion relation for free electrons in the crystal is

$$E_n(\mathbf{k}) = \frac{\hbar^2}{2m_e}k^2 = E_n(\mathbf{k} + \mathbf{K}_n) = \frac{\hbar^2}{2m_e}|\mathbf{k} + \mathbf{K}_n|^2. \qquad (2.8)$$

Thus, we can always find a vector $\mathbf{K}$ which maps the dispersion relation into the first Brillouin zone.
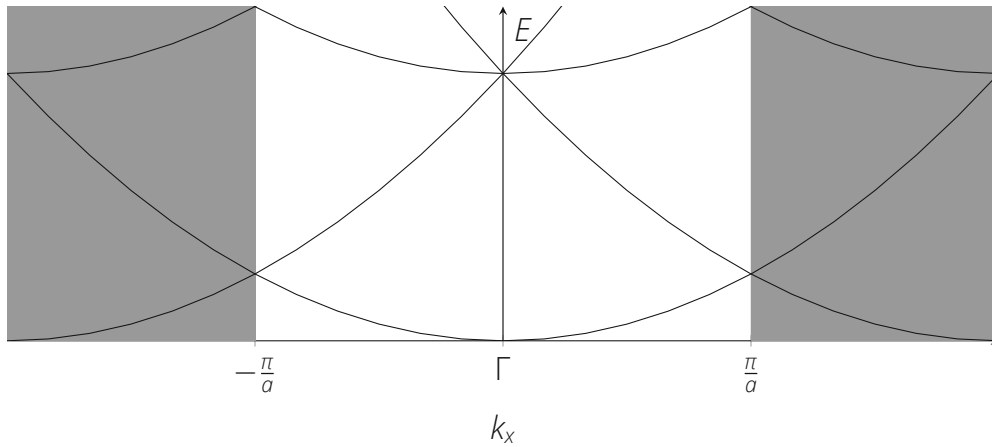

Figure 2.1: Band structure of non-interacting electrons in a simple cubic lattice in k_x direction. The region outside of the first Brillouin zone is shaded. The different energy bands originate from writing $\mathbf{K}_n$ in terms of Miller indices.[25]

Even in this most simple approximation, the band structure appears as quite complex, as can be seen when visualizing the free electron band structure for various paths in $\mathbf{k}$-space, such as the one in Figure 2.2.

As a next step we investigate a periodic potential that is non-zero, but still small, and assume that the Fourier expansion of the potential in Equation 2.1 is adequately described by only a single component $V_\mathbf{K}$.[25] Translation of a reciprocal lattice vector in Equation 2.4 yields[29]

$$\left(E - \frac{\hbar^2}{2m_e}|\mathbf{k} - \mathbf{K}'|^2\right)C_{\mathbf{k}-\mathbf{K}'} = \sum_\mathbf{K} V_\mathbf{K} C_{\mathbf{k}-\mathbf{K}'-\mathbf{K}} = \sum_{\mathbf{K}''} V_{\mathbf{K}''-\mathbf{K}'}C_{\mathbf{k}-\mathbf{K}''}, \qquad (2.9)$$

where we substituted $\mathbf{K}'' = \mathbf{K} + \mathbf{K}'$ on the right hand side.[25] In a first approximation, we seek a solution for the coefficients

$$C_{\mathbf{k}-\mathbf{K}'} = \frac{\sum_{\mathbf{K}''} V_{\mathbf{K}''-\mathbf{K}'}C_{\mathbf{k}-\mathbf{K}''}}{\left(E - \frac{\hbar^2}{2m_e}|\mathbf{k} - \mathbf{K}'|^2\right)} \qquad (2.10)$$
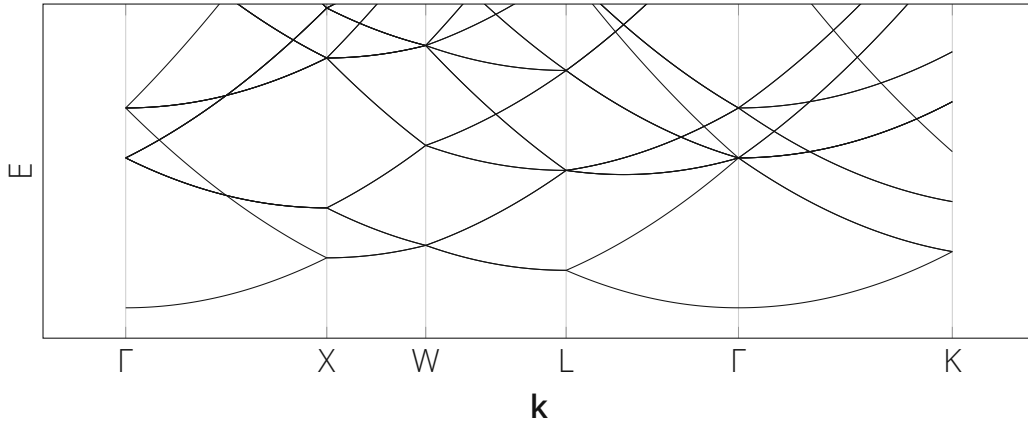
6

Figure 2.2: Band structure of the free electron approximation for the fcc-lattice along the path Γ-X-W-L-Γ-K.[27,28]

with the largest values. Substitution of E with the free electron energy of Equation 2.8 shows that the coefficient is largest when the denominator in Equation 2.10 vanishes. This is the case precisely when either $k^2 \approx |\mathbf{k} - \mathbf{K}'|^2$ or $\mathbf{K}' = 0$. The largest coefficients are therefore $C_{\mathbf{k}}$ and $C_{\mathbf{k}-\mathbf{K}'}$. In both cases, the sum in the numerator reduces to a single value. The solution of the resulting system of two coupled equations is[25,27,29]

$$E^{\pm} = \frac{1}{2}(E_{\mathbf{k}-\mathbf{K}'} + E_{\mathbf{k}}) \pm \sqrt{\frac{1}{4}(E_{\mathbf{k}-\mathbf{K}'} - E_{\mathbf{k}})^2 + |V_{\mathbf{k}}|^2}. \qquad (2.11)$$

The degeneracy at the parabola intersections is lifted by a factor of $2|V_{\mathbf{k}}|$ when $E_{\mathbf{k}-\mathbf{K}'} \approx E_{\mathbf{k}}$, as can be seen in Figure 2.3.

The interactions between electrons are therefore responsible for energy gaps in the band structure. In practice, the band structure can deviate quite substantially from the free electron case. A method to treat the case where the potential can no longer assumed to be weak is presented in section 2.3.

2.3   Kohn-Sham Equations

In the previous section we have studied the properties of a single electron affected by the weak periodic potential in a cubic lattice. In general of course, the structures may be more complex and the introduction of additional electrons may result in strong correlation effects. The numerical analysis of materials poses a significant challenge and many different approximations have been developed to form the foundations of the broad field of materials modeling.[30]
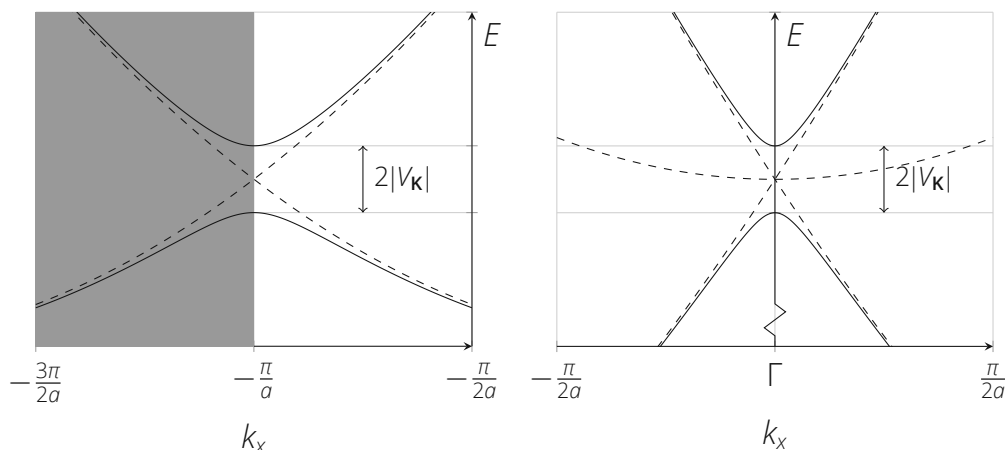
7

Figure 2.3: The origin of band gaps is explained by the introduction of a weak potential and observation of the dominant Fourier coefficients. On the left the region at the border of the first Brillouin zone and on the right the center of the Brillouin zone is shown. The dashed lines correspond to the free electron approximation in Figure 2.1. In both cases, the degeneracy is lifted in the presence of a weak periodic potential and an energy gap appears.

In quantum chemistry, a rough categorization of approaches may be done according to the strength of correlations: If the potential V is large then often the Hamilton operator is modeled to account for particular types of interactions, as it is done in the Hubbard- or Heisenberg model for example. If the potential V is not as large, usually the Hamilton-operator is retained but restrictions on the wave functions are imposed. The latter class also goes by the name of *ab-initio* methods.[30,31]

A particularly often used *ab-initio* method is Density Functional Theory (DFT), due to its outstanding compromise between chemical accuracy and computational demand.[32] Its ongoing development was started in the second half of the twentieth-century[30,33,34] and its significance was already acknowledged by the award of the Nobel prize in 1998.[35] DFT is also the principal method used in this work.

The centerpiece of DFT are the Kohn-Sham equations, which represent the Schrödinger equation within the imposed approximations. While a brief introduction demonstrating the most important concepts is given in the following, more thorough introductions can be found in the textbooks and articles cited in this section.

The foundation of DFT lies in the Hohenberg-Kohn theorem, which states that for the ground state, the wave function $\Psi(\mathbf{r}_1, \dots, \mathbf{r}_N)$ of N identical particles

in an external potential $V(r)$ can be uniquely represented by the particle density of the ground state $n_g(\mathbf{r})$[36,37]

$$\Psi_g(\mathbf{r}_1, \ldots, \mathbf{r}_N) = \Psi[n_g].\qquad(2.12)$$

This astonishing property evidently simplifies handling the wave function significantly. Any observable is also defined by the particle density

$$\langle\Psi|\hat{O}|\Psi\rangle = O[n_g],\qquad(2.13)$$

including the energy. Equation 2.12 is only exact for the ground state, although for low enough temperature, it may still be valid as an approximation. In the following we will only be concerned with the (near) ground state and will drop the corresponding index i.e. $n_g(\mathbf{r}) = n(\mathbf{r})$.

Additionally, Equation 2.12 is only valid when the particles are moving in an external potential. To satisfy this condition in a solid state, we require that the electrons move in the electromagnetic field generated by the nuclei, which are kept at fixed positions. Because the nuclei are much heavier, their movement takes place on timescales separated from the electronic part so that the ionic and electronic wave functions decouple

$$|\Psi\rangle = |\Psi_n\rangle \otimes |\Psi_e\rangle.\qquad(2.14)$$

Thus, we first solve the electronic part, and then use the energy for the ionic part

$$\hat{H}_e |\Psi_e\rangle = E_e |\Psi_e\rangle,\qquad(2.15)$$
$$\hat{H}_n |\Psi_n\rangle = E_n |\Psi_n\rangle,\qquad(2.16)$$

where the contributions of the Hamiltonians are

$$\hat{H}_e = \hat{T}_e + \hat{V}_{e-e} + \hat{V}_{n-e},\qquad(2.17)$$
$$\hat{H}_n = \hat{T}_n + \hat{V}_{n-n} + \hat{H}_e.\qquad(2.18)$$

This approach is known as the Born-Oppenheimer approximation[31,38] and is valid for almost all practical applications. Only in the case of hydrogen some care has to be applied.

We now focus solely on the electronic part in Equation 2.15 and Equation 2.17. The *external* interaction between electrons and nuclei can be calculated with the Coulomb attraction, and its functional with respect to the particle density is straightforwardly obtained

$$V_{n-e}[n] = V_{C,n-e}[n] = \int d^3\mathbf{r}\, n(\mathbf{r}) V_{C,n}(\mathbf{r})\qquad(2.19)$$

9

where

$$V_{C,n}(\mathbf{r}) = \frac{1}{4\pi\varepsilon_0} \sum_{i=1}^{N_n} \frac{Z_i q_e^2}{|\mathbf{r_i} - \mathbf{r}|} \qquad (2.20)$$

is the Coulomb potential.

For the electron-electron interaction, we proceed in the same manner as before but since the interaction is more intricate due to *exchange* contributions resulting from repulsion of electrons with equal spin due to the Pauli principle, the energy that is left out by the Coulomb interaction is accounted for by an extra term

$$V_{e-e}[n] = V_{C,e-e}[n] + E_X[n], \qquad (2.21)$$

with

$$V_{C,e-e}[n] = \frac{1}{2} \int \mathrm{d}^3\mathbf{r} \int \mathrm{d}^3\mathbf{r}' n(\mathbf{r}) V_{C,e}(\mathbf{r} - \mathbf{r}') n(\mathbf{r}'), \qquad (2.22)$$

where

$$V_e(\mathbf{r}) = \frac{1}{4\pi\varepsilon_0} \frac{q_e^2}{|\mathbf{r}|} \qquad (2.23)$$

is the Coulomb kernel.

$E_X[n]$ may for example be calculated by means of the Local Density approximation (LDA), or alternatively using the non-local approach of Hartree-Fock theory, but which method to choose depends on the specific problem as each approach has its strengths and weaknesses and chemical accuracy versus computational time has to be taken into account.

The final task is finding a functional form for the kinetic energy $\hat{T}_e$. Unfortunately, a straightforward expression does not exist. However, assuming that the kinetic energy can be separated into a non-interacting and an interacting contribution, it is possible, with the introduction of single particle orbitals $\Psi_s(\mathbf{r})$, to add a term which includes energetic contributions from *correlations*

$$T_e[n] = T_s[n] + E_C[n], \qquad (2.24)$$

with

$$T_s[n] = T_s[\{\Psi_s(\mathbf{r})\}] = -\frac{\hbar^2}{2m_e} \sum_{i=1}^{N_n} \int \mathrm{d}^3\mathbf{r}\, \Psi_{s,i}(\mathbf{r}) \nabla^2 \Psi_{s,i}(\mathbf{r}). \qquad (2.25)$$

Correlation energy contributions E_C originate from the fact that the motion of an individual electron is not only influenced by the external potential of the other electrons, but additionally there is a coupled movement: The individual electron interacts via Coulomb repulsion with the other electrons simultaneously. In particular, consider the joint probability density $\rho_{ab}(\mathbf{r}_a, \mathbf{r}_b)$ to find two

electrons a and b in some volume. Strong correlation means that it is not possible to separate this probability density for the two electrons as an approximation

$$\rho_{ab}(\mathbf{r}_a, \mathbf{r}_b) \approx \rho_a(\mathbf{r}_a)\rho_b(\mathbf{r}_b). \tag{2.26}$$

In conclusion, the functional form of the total energy is[37]

$$E_e[n] = T_s[n] + V_{C,e-e}[n] + V_{C,n-e}[n] + E_{XC}[n], \tag{2.27}$$

where $E_{XC}[n] = E_X[n] + E_C[n]$ is the *exchange-correlation* functional, which, along with $\{\Psi_s\}$, is still to be determined. Finding an expression for $E_{XC}[n]$ is not a trivial task and many approximations may be found in the literature.[39,40] In general, the most important distinction of different DFT calculations is the choice of an expression for the exchange-correlation functional.

With the single particle orbitals $\{\Psi_s\}$ we can calculate the corresponding particle density

$$n_s(\mathbf{r}) = \sum_{i=1}^{N_n} |\Psi_{s,i}(\mathbf{r})|^2. \tag{2.28}$$

This particle density is equal to the ground state density when minimizing the total energy in Equation 2.27:

$$0 = \left.\frac{\delta E_e[n_s]}{\delta n_s}\right|_{n_s=n} = \frac{\delta T_s[n_s]}{\delta n_s} + v_{e-e}(\mathbf{r}) + v_{n-e}(\mathbf{r}) + v_{XC}(\mathbf{r}) \tag{2.29}$$

$$= \frac{\delta T_s[n_s]}{\delta n_s} + \int \mathrm{d}^3\mathbf{r}'\, n_s(\mathbf{r}')V_{C,e}(\mathbf{r} - \mathbf{r}') + V_{C,n}(\mathbf{r}) + v_{XC}(\mathbf{r}), \tag{2.30}$$

where we used a lower case v for the result of a functional derivative $v(\mathbf{r}) = \delta V[n]/\delta n$. Minimization in this way may also be done on the single particle functional

$$0 = \frac{\delta E_{e,s}[n_s]}{\delta n_s} = \frac{\delta T_s[n_s]}{\delta n_s} + v_s(\mathbf{r}), \tag{2.31}$$

where n_s can be found by solving the Schrödinger equation for the single particle orbitals

$$\left(-\frac{\hbar^2}{2m_e}\nabla^2 + v_s(\mathbf{r})\right)\Psi_{s,i}(\mathbf{r}) = E_{s,i}\Psi_{s,i}(\mathbf{r}) \tag{2.32}$$

and using Equation 2.28. A comparison of Equation 2.30 with Equation 2.31 shows that we can construct an auxiliary single particle Schrödinger equation as in Equation 2.32 when

$$v_s(\mathbf{r}) = v_{e-e}(\mathbf{r}) + v_{n-e}(\mathbf{r}) + v_{XC}(\mathbf{r}) \tag{2.33}$$

$$= \int \mathrm{d}^3\mathbf{r}'\, n(\mathbf{r}')V_{C,e}(\mathbf{r} - \mathbf{r}') + V_{C,n}(\mathbf{r}) + v_{XC}(\mathbf{r}). \tag{2.34}$$

11

The system of equations in Equation 2.32 with the potential in Equation 2.33 is known as the Kohn-Sham equations. Solving these equations iteratively and self-consistently is the main procedure in DFT applications. The converged density is the ground state density as it is required for the total energy in Equation 2.27.

Strictly speaking, the Kohn-Sham eigenvalues $E_{s,i}$ have no physical meaning. A relation to the electronic energy E_e can be found as follows. The total Kohn-Sham energy is

$$E_{e,s}[n] = \sum_{i=1}^{N_n} E_{s,i} = T_s[n] + \int d^3\mathbf{r}\, v_s(\mathbf{r})n(\mathbf{r}). \tag{2.35}$$

Solving Equation 2.35 for the kinetic energy and plugging the result together with the potential in Equation 2.33 into the total energy in Equation 2.27 yields[41]

$$\begin{aligned} E_e[n] = &\sum_{i=1}^{N_n} E_{s,i} \\ &- \frac{1}{2} \int d^3\mathbf{r} \int d^3\mathbf{r}'\, n(\mathbf{r}')V_{C,e}(\mathbf{r} - \mathbf{r}')n(\mathbf{r}) \\ &- \int d^3\mathbf{r}\, v_{XC}(\mathbf{r})n(\mathbf{r}) + E_{XC}[n]. \end{aligned} \tag{2.36}$$

With the electronic part of the problem solved, we can move on to the ionic part. Due to the large mass of the nuclei, a quantum calculation is usually unnecessary. The ionic positions as required in the external potential in Equation 2.20 can be updated by moving along the total force vector as generated by the electrons. After the nuclei are displaced, the particle density no longer represents the ground state and it needs to be minimized again. In an ionic relaxation, this procedure is repeated until the forces become smaller than an externally defined threshold.

In a nutshell, the initial approach in quantum chemistry is to decouple the ionic and the electronic problem. Then, in DFT the all-electron wave function is replaced by a particle density, which is only valid for the ground state, and all observables become functionals of this density. In the Kohn-Sham scheme, the kinetic energy functional is then again expressed in terms of single-particle wave functions and the electron-electron interaction is modeled to be due to coulomb repulsion. This neglect of correlations and quantum interactions is treated by the type of exchange-correlation functional, which has to be chosen for the simulation. The singe particle Kohn-Sham orbitals are obtained by solving an auxiliary Schrödinger equation self consistently. The eigenvalues and

the converged particle density is finally used to obtain the total electronic energy.[37,42]

It is appropriate to note, that apart from the Born-Oppenheimer approximation, DFT would in fact be an exact theory.[34] The only deviation from the result of the many-body Schrödinger equation originates solely from the exchange-correlation functional, where no exact expression is known. Thus, if DFT is a suitable choice for the simulation of a particular material greatly depends on how the exchange-correlation functional is useful to the problem.

2.4   Phonons

In section 2.3 we have seen that it is in principle possible to calculate the electronic ground state given an external potential V. However, atomic positions change due to temperature, not arbitrarily, but along certain modes. Various properties of solid state systems originate from this collective displacement of atomic positions. For instructive reasons, we start with simple systems and eventually treat the general case.

2.4.1   Classical Approach

The simplest system consists of an atomic chain in one dimension x with a single atom in its unit cell. The unit cells, as well as their containing atoms are labeled with the indices i and j. The displacement of an atom from its equilibrium position in unit cell j is denoted by u_j. The force on each atom may be calculated with classical mechanics because of the Born-Oppenheimer theorem. For small displacements, the interatomic potential may be approximated by the harmonic oscillator and the force acting on an atom in i is obtained by

$$F_j = \sum_i \zeta_{ji}(u_j - u_i), \tag{2.37}$$

where ζ_{ji} is the coupling constant

$$\zeta_{ji} = -\frac{\partial^2 V(x)}{\partial x_j \partial x_i}. \tag{2.38}$$

This being the case, the system can be thought of mass points connected by springs.

We can choose an index $p = j - i$ and rewrite $\zeta_{ji} = \zeta_p$ where $p \in \mathbb{Z}$. We additionally assume that the interaction only acts on neighboring sites, hence

the forces can be expressed as

$$F_j = \sum_{p=-1}^{1} \zeta_p \left(u_{j+p} - u_j\right),$$

(2.39)

where the symmetry can again be used to express $\zeta_{-p} = \zeta_p$ and

$$F_j = \zeta_1 \sum_{p=-1,1} \left(u_{j+p} - u_j\right).$$

(2.40)

The equations of motions as given by Newton's second law

$$m\frac{\partial^2 u_j(t)}{\partial t^2} = F_j$$

(2.41)

pose the challenge of having to solve n-coupled differential equations. An ansatz for the solution of the problem is

$$u_{j+p} = A \operatorname{Re}\left\{e^{i(q(j+p)a - \omega t)}\right\},$$

(2.42)

where A is the amplitude, q is the wave number and ω the frequency of the harmonic motion. Plugging the ansatz into the equations of motions and setting $j = 0$ for simplicity we obtain

$$-m\omega^2 A e^{-i\omega t} = \zeta_1 \sum_{p=-1,1} \left(A e^{i(qpa - \omega t)} - A e^{i\omega t}\right)$$

(2.43)

$$\Rightarrow \omega^2 = -\frac{\zeta_1}{m}\left(e^{iqa} + e^{-iqa} - 2\right)$$

(2.44)

$$= \frac{2\zeta_1}{m}(1 - \cos qa)$$

(2.45)

$$= \frac{4\zeta_1}{m}\sin^2\frac{qa}{2},$$

(2.46)

Since the negative solution is non-physical for a periodic motion, the dispersion relation results in[43–45]

$$\omega(q) = \sqrt{\frac{4\zeta_1}{m}}\left|\sin\frac{qa}{2}\right|,$$

(2.47)

as is shown in Figure 2.4.

For a unit cell containing two atoms we proceed with the same approximations as in the previous case and label the two different atoms with α and
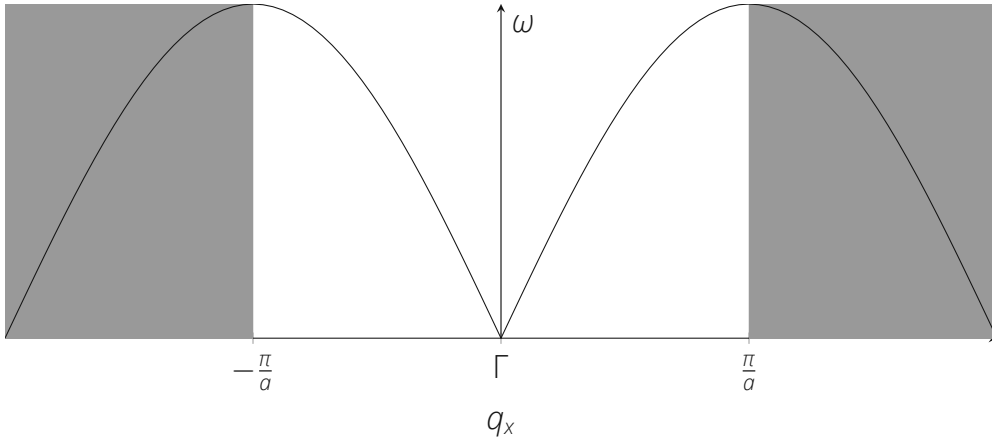
Figure 2.4: Dispersion Relation for a 1D atomic chain with a single atom in the unit cell.

β. Since we have only nearest neighbor interactions, the coupling constant is again ζ_1. There are two sets of equations of motion

$$m_\alpha \frac{\partial^2 u_{j\alpha}}{\partial t^2} = \zeta_1 \left(u_{j-1\beta} - u_{j\alpha} \right) + \zeta_1 \left(u_{j\beta} - u_{j\alpha} \right) \tag{2.48}$$

$$m_\beta \frac{\partial^2 u_{j\beta}}{\partial t^2} = \zeta_1 \left(u_{j\alpha} - u_{j\beta} \right) + \zeta_1 \left(u_{j+1\alpha} - u_{j\beta} \right) \tag{2.49}$$

We use the same ansatz as before

$$u_{j\alpha} = \text{Re} \left\{ A_\alpha e^{i(qja - \omega t)} \right\} \tag{2.50}$$

to obtain by considering nearest-neighbor interactions and setting $j = 0$

$$-m_\alpha \omega^2 A_\alpha = \zeta_1 \left(A_\beta e^{-iqa} - A_\alpha \right) + \zeta_1 \left(A_\beta - A_\alpha \right), \tag{2.51}$$

$$-m_\beta \omega^2 A_\beta = \zeta_1 \left(A_\alpha - A_\beta \right) + \zeta_1 \left(A_\alpha e^{iqa} - A_\beta \right). \tag{2.52}$$

This is a linear system of equations

$$A_\alpha \left(m_\alpha \omega^2 - 2\zeta_1 \right) + A_\beta \zeta_1 \left(1 + e^{-iqa} \right) = 0, \tag{2.53}$$

$$A_\alpha \zeta_1 \left(1 + e^{iqa} \right) + A_\beta \left(m_\beta \omega^2 - 2\zeta_1 \right) = 0, \tag{2.54}$$

and after some linear algebra and discarding the two negative frequencies, the solutions are[43,46,47]

$$\omega^2 = \frac{\zeta_1}{m_\alpha m_\beta} \left(m_\alpha + m_\beta \pm \sqrt{ \left(m_\alpha + m_\beta \right)^2 - 4 m_\alpha m_\beta \sin^2 \frac{qa}{2} } \right). \tag{2.55}$$

15

Here we end up with two solutions, depending on the sign, ω_+ and ω_-. The physical interpretation is that the lower frequencies correspond to motions of α and β in phase, whereas the higher frequencies oscillate in antiphase. The latter case creates stronger dielectric fields, since the atoms move closer together. Thus, these oscillations can be excited by low-frequency electromagnetic waves, hence this dispersion relation is called optical mode. In contrast, the lower frequency does not show this behavior and is called acoustic mode.
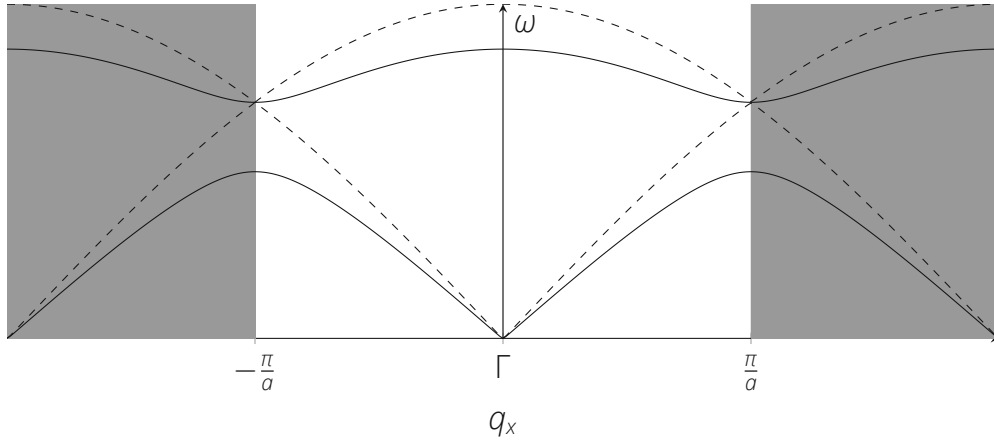

Figure 2.5: Optical and acoustic mode in a 1-D atomic chain with two atoms in the unit cell. The solid line represents the dispersion relation when $m_\alpha = 2m_\beta$, while the dashed line represents the case when $m_\alpha = m_\beta$.

In principle, the approach in two and three dimensions is the same. The equations of motions are generalized when $l = x, y, z$ is the spatial dimension

$$m_\alpha \frac{\partial^2 u_{j\alpha l}}{\partial t^2} = -\sum_{j'\alpha'l'} \zeta_{j\alpha l}^{j'\alpha'l'} u_{j'\alpha'l'}. \tag{2.56}$$

We are always free to choose the origin, thus $j = 0$. In the 1D case, the spatial coordinate $l = x$ could be dropped. In the single atomic unit cell the index $\alpha = \alpha'$ could also be dropped, in the two atomic case $\alpha, \alpha' = \{\alpha, \beta\}$. We only considered nearest neighbor interactions so $j' = \{1, -1\}$ and further $\zeta_1 \equiv \zeta_0^1 = \zeta_0^{-1}$

The wave ansatz in two or three dimensions contains a scalar product in the exponent

$$\mathbf{u}_{j\alpha} = \mathbf{A}_\alpha e^{i(\mathbf{q}\cdot\mathbf{a}_j - \omega t)}. \tag{2.57}$$

For 2D lattices, this leads to a dispersion relation $\omega(\mathbf{q}) : \mathbb{R}^2 \to \mathbb{R}$, whereas for 3D lattices $\omega(\mathbf{q}) : \mathbb{R}^3 \to \mathbb{R}$ may be visualized with a band structure in complete analogy to section 2.2.

16

In practice however any real system makes analytic solutions challenging to solve. For example in 3D, the equations are sixth order in ω and while a cubic lattice containing one atom with only nearest neighbor interaction has relatively compact solutions, next nearest neighbor interactions already include lengthy expressions for the coefficients, which is not helpful considering the solutions of these sixth order equations are also quite extensive themselves.[48]

2.4.2 Quantum Approach

Since lattice modes have an assigned frequency and wave length, the wave-particle duality can be applied to study phonons as the respective quasiparticles in the quantum picture.

The 1D chain with one-atomic unit cells is again the starting point for our considerations. In the harmonic approximation, the Hamilton-Operator reads

$$H = \sum_n \left[\frac{1}{2m} p_j^2 + \frac{1}{2}\zeta\left(x_{j+1} - x_j\right)^2 \right]. \tag{2.58}$$

A Fourier transform to phonon-coordinates for the displacement and momentum operators has to be performed

$$x_j = \frac{1}{\sqrt{N}} \sum_q X_q e^{iqja}, \tag{2.59}$$

$$p_j = \frac{1}{\sqrt{N}} \sum_q P_q e^{-iqja}. \tag{2.60}$$

This means for the momentum part of the Hamiltonian

$$\sum_j p_j^2 = \frac{1}{N} \sum_{j,q,q'} P_q P_{q'} e^{-i(q+q')ja} \tag{2.61}$$

$$= \sum_{j,q,q'} P_q P_{-q'} \delta(-q, q') \tag{2.62}$$

$$= \sum_q P_q P_{-q} \tag{2.63}$$

and for the position part

$$\sum_n \left(x_{j+1} - x_j\right)^2 = \frac{1}{N} \sum_{j,q,q'} X_q X_{q'} e^{i(q+q')a} \left(1 + e^{-i(q+q')a} - e^{iq'a} - e^{iqa}\right) \tag{2.64}$$

$$= 2 \sum_q X_q X_{-q} (1 - \cos qa) \tag{2.65}$$

$$= 4 \sum_q X_q X_{-q} \sin^2 \frac{qa}{2}. \tag{2.66}$$

$$\tag{2.67}$$

Introducing the dispersion relation

$$\omega_q = \sqrt{\frac{4\zeta}{m}} \sin^2 \frac{qa}{2}, \tag{2.68}$$

the Phonon Hamiltonian is

$$H = \sum_q \left(\frac{1}{m} P_q P_{-q} + \frac{1}{2} m \omega_q^2 X_q X_{-q}\right). \tag{2.69}$$

The equations of motion are obtained by the time evolution in the Heisenberg picture

$$i\hbar \dot{X}_q = [X_q, H] = i\hbar \frac{P_{-q}}{M}. \tag{2.70}$$

It is instructive to look at the second derivative as well

$$i\hbar \ddot{X}_q = \left[\dot{X}_q, H\right] = \frac{1}{M}[P_{-q}, H] = i\hbar \omega_q^2 X_q. \tag{2.71}$$

Thus, the equations of motion are

$$\ddot{X}_q + \omega_q^2 X_q = 0, \tag{2.72}$$

which are the equations of motion for the harmonic oscillator with frequency ω_q. This is a standard problem and its energy eigenvalues are known to be

$$E_q = \hbar \omega_q \left(n_q + \frac{1}{2}\right), \quad n_q \in \mathbb{N}. \tag{2.73}$$

Since phonons are bosonic quasiparticles, they follow the Bose-Einstein statistics, where the average occupation number of a mode is expected to be

$$\langle n_q \rangle = \frac{1}{e^{\hbar \omega_q / k_B T} - 1}, \tag{2.74}$$

for a state with energy E_q at temperature T with the chemical potential μ.[49]

18

2.5 Impurities in Insulators

As we have shown in section 2.2, interactions create gaps in the electronic band structure. Materials can be classified as conducting and insulating via the position of the Fermi level. If it lies within a band, the electrons can respond to external fields and transfer current through a collective momentum, since the band is only partially occupied.[50]

If the Fermi level lies within a band gap, electrons lose the ability for collective motion and the material is insulating. In particular, the band gap becomes large when the valence electrons completely fill the outer shell. Insulators can therefore be classified via the dominant type of chemical bonding.[51]

1. Molecular Insulators: As an example of this class, the solid form of noble gases show extreme tight-binding via the Van-der-Waals interaction with the orbitals remaining largely in their atomic configuration and thus localized around the nuclei. Since these elements have a completely filled shell, a lot of energy is required for an electron to be promoted into the conduction band.

2. Ionic Insulators: Here the electronic charge distribution is also localized around the nuclei but the material is composed of atomic species with sharply different electronegativity. Thus the atoms become ionized by donating or accepting some electrons to accommodate a full shell. Examples are binary compounds consisting of elements from group I or II in a bond with elements from group VI or VII.

3. Covalent Insulators: In a covalent bond the electrons are not localized near the nuclei but in a region in between. An atom may share their electrons with other atoms such that each can fill up their shell. A well known covalent insulator is diamond, where each C atom shares four electrons with its nearest neighbors in the interstitial space.

Note that the while the distinction between metallic and insulating is done in momentum space, the classification of insulators is done by analyzing the particle density in real space. While the former is more precise and quantitative, the latter may help us further in understanding the material qualitatively.

So far, we have described materials by choosing an infinite periodic atomic structure. Evidently, this is only an idealized picture. For one thing, there is the obvious omission of the materials surface. Its microscopic study is an extensive topic in itself and is not part of this work. The only property of the surface we want to keep in mind is that there is in general an energy barrier with regards to the exchange of particles with the environment.

Apart from that, the lattice structure itself usually shows distortions in its periodicity. On the one hand there might be grain boundaries, where two or more rotated periodic structures meet. Macroscopic crystals with no such boundary are rarely found in nature but can be grown in artificial conditions in a laboratory.

On the other hand, a common occurrence are crystals where there are defects or impurities in their lattice structure. On defect sites there is either a vacancy or an interstitial placement of an atom that forms the lattice. Impurities denote the presence of an external atom which is not part of the original arrangement. These two irregularities are often important for the physical characteristics of the material, such as thermal conductivity by scattering phonons or optical properties.[52]

Impurities and defects are imperfections that are energetically unfavorable to the original structure, however they cannot overcome the various internal energy barriers and the surface for the material to relax into its ground state.

In the following we focus on impurities in insulators. Impurity atoms will be situated either on an interstitial position in the lattice, or they substitute atoms on their lattice position. In any case, the impurity is usually the cause of a charge imbalance in its local environment*. For the shell to remain completely filled, particles will be positioned on a location near the impurity atom. Thus, not only the impurity itself, but also the specific types of charge compensation determine the alternation of the material's properties. Hence impurities are not necessarily undesirable but can in fact be actively introduced to the crystal as a dopant.

Numerical simulations can be made to study the microscopic compensation mechanism. A realistic approach would be to simulate the diffusion of the atoms taking part in the impurity during charge compensation formation through the surface as well as inside the bulk. Unfortunately, a quantum treatment of this problem is, as of this date, mostly prohibited by the huge computational cost, even when using efficient methods such as DFT.

However, it is possible to alleviate this issue by considering the static possible final states of the system, forgoing the diffusion aspect. By evaluating the total energy of the material and the impurity constituents, the microscopic compensation mechanism can be studied. A comparison of the total energy of different realizations of the charge compensation yields a statistical average of the occurrence for the respective scheme.

In this approach the first and most significant step is to carefully determine

---

*The only exception where this effect is minor is substitutional doping with an element in the same group in the periodic table. This trivial case should not require any sophisticated treatment and is therefore not specifically mentioned in the following discussions.

the possible charge compensation schemes by studying the atoms required for the impurity formation processes. This ensures that the outcome of the study is not erroneous due to the involuntary oversight of a specific scheme. An example is shown in Figure 2.6. Next, total energies may be calculated for each scheme, keeping in mind that the number of particles has to stay the same for a valid comparison. The number of possible charge compensation schemes is generally large, hence it is useful to rule out several nonphysical realizations beforehand.

When the dopant has donated its valence electrons to the crystal and charge compensation atoms, often the next excited state lies within the band gap. Because the impurity is non-periodic, these states are immobile and localized. They retain their quasi atomistic properties and do not interact with the conduction band electrons.

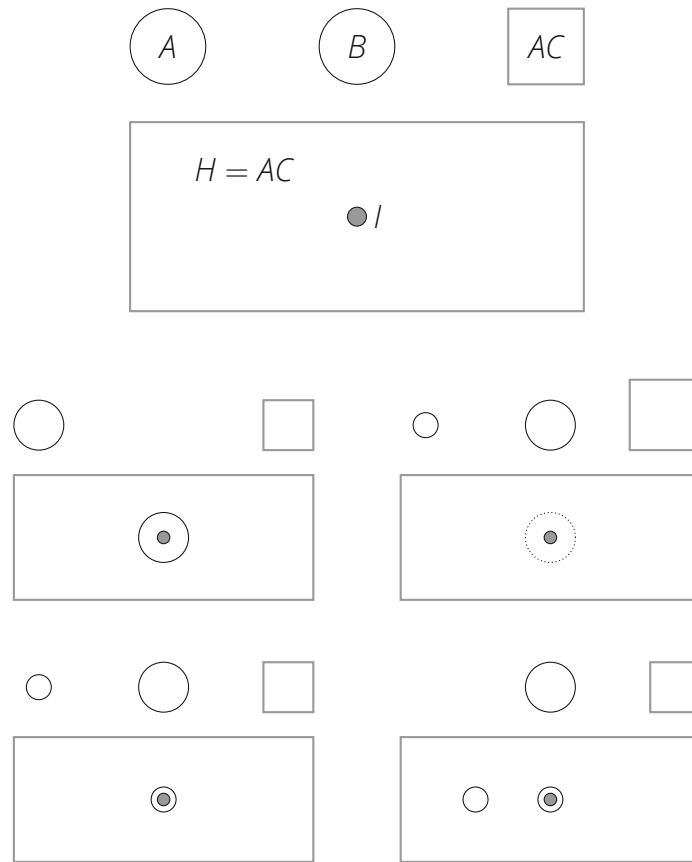A B AC

$H = AC$

$\bullet\,I$

Figure 2.6: An example for charge compensation schemes. Top: All possible constituents that may take part in the impurity are depicted. There are three allotropes A, B and C, where the circles are meant to be non-periodic and outside the host in the gas phase in their respective preferred formation at standard conditions. A square indicates a periodic lattice. Below, the periodic host crystal H shall be composed of $H = AC = nA + mC$. The dopant has been introduced to the host crystal, either as an interstitial or a substitutional placement forming an impurity I. Next, several different possibilities for charge compensation mechanisms are depicted. The labels are omitted for visual clarity. Middle, left: I absorbs B. Middle, right: C leaves behind a vacancy in I and together with A forms a new unit cell of AC. Bottom left: a part of A is at I, while its other part remains gaseous. Bottom row, right: a part of A is at I while its other part creates another defect somewhere else in H. This list is not exhaustive, as there may even be more cases to be considered. The complexity can increase additionally when there are possibilities with other species D, E, etc.

22

Chapter 3

Computational Methods

3.1 Exchange Correlation Potential

3.1.1 Local Density Approximation

The methods introduced in section 2.3 require a functional form for the exchange and correlation energy with respect to the particle density. A useful starting point is the homogeneous interacting electron gas with N_e electrons in a box with volume Ω and Born-von Karman periodic boundary conditions. In this case, the exchange energy can be explicitly calculated.

The main idea behind the Local Density Approximation (LDA) is that regions in space each behave locally as a homogeneous electron gas such that the exchange energy density $\varepsilon_X = E_X/N_e$ can be obtained by spatial integration

$$E_X = \int \mathrm{d}^3\mathbf{r}\, n(\mathbf{r})\varepsilon_X(n). \tag{3.1}$$

The derivation of ε_X is briefly shown in the following.

First, the total exchange energy is by definition calculated within the Hartree-Fock approximation[53–56]

$$E_X = -\frac{1}{2}\frac{e^2}{4\pi\varepsilon_0}\sum_{\substack{i,j=1\\i\neq j}}^{N_e}\iint_\Omega \mathrm{d}^3\mathbf{r}_1\mathrm{d}^3\mathbf{r}_2\frac{\Psi_i(\mathbf{r}_1)\Psi_i^*(\mathbf{r}_2)\Psi_j^*(\mathbf{r}_1)\Psi_j(\mathbf{r}_2)}{|\mathbf{r}_1-\mathbf{r}_2|}. \tag{3.2}$$

The wave functions

$$\Psi_j(\mathbf{r}) = \frac{e^{i\mathbf{k}_j\cdot\mathbf{r}}}{\sqrt{\Omega}} \tag{3.3}$$

are obtained by solving the stationary Schrödinger equation for the potential well with a volume of Ω.[54,56] After plugging this result into the Hartree-Fock

approximation, the exchange energy is

$$E_X = -\frac{e^2}{8\pi\varepsilon_0\Omega^2} \sum_{\substack{i,j=1 \\ i\neq j}}^{N_e} \iint_\Omega d^3\mathbf{r}_1 d^3\mathbf{r}_2 \frac{e^{i(\mathbf{k}_i-\mathbf{k}_j)\cdot(\mathbf{r}_1-\mathbf{r}_2)}}{|\mathbf{r}_1-\mathbf{r}_2|}. \tag{3.4}$$

To solve the integral, the following result can be used:[57]

$$\int d^3\mathbf{r} \frac{e^{i\mathbf{k}\cdot\mathbf{r}}}{|\mathbf{r}|} = \frac{4\pi}{|\mathbf{k}|^2}. \tag{3.5}$$

Additionally reducing the two spatial integrals with a transformation $\mathbf{r}' = \mathbf{r}_1 - \mathbf{r}_2$ to

$$\iint_\Omega d^3\mathbf{r}_1 d^3\mathbf{r}_2 \rightarrow \Omega \int d^3\mathbf{r}', \tag{3.6}$$

gives a simple expression for the exchange energy

$$E_X = \frac{e^2}{2\varepsilon_0\Omega} \sum_{\substack{i,j=1 \\ i\neq j}}^{N_e} \frac{1}{|\mathbf{k}_i-\mathbf{k}_j|^2}. \tag{3.7}$$

Further, instead of taking the sum over all electrons, it is equivalent to sum over all wave vectors. In this approximation, the number of electrons N_e needs to be large enough such that the states $\mathbf{k}_i$ are almost continuously occupied up until the Fermi wave vector $\mathbf{k}_F$. Hence the sum can be replaced by an integral according to the relation[58]

$$\sum_i \rightarrow \frac{\Omega}{(2\pi)^3} \int d^3\mathbf{k} \tag{3.8}$$

and the exchange energy is

$$E_X = -\frac{e^2\Omega}{\varepsilon_0 2^7\pi^6} \iint_0^{\mathbf{k}_F} \frac{d^3\mathbf{k}_i d^3\mathbf{k}_j}{|\mathbf{k}_i-\mathbf{k}_j|^2}. \tag{3.9}$$

With the substitution of $\mathbf{k}' = \mathbf{k}_i - \mathbf{k}_j$ such that

$$\iint_0^{\mathbf{k}_F} d^3\mathbf{k}_i d^3\mathbf{k}_j \rightarrow \mathbf{k}_F^3 \int_0^{\mathbf{k}_F} d^3\mathbf{k}', \tag{3.10}$$

and performing the integration in spherical coordinates, the integral results in

$$\iint_0^{\mathbf{k}_F} \frac{d^3\mathbf{k}_i d^3\mathbf{k}_j}{|\mathbf{k}_i-\mathbf{k}_j|^2} = 4\pi^2\mathbf{k}_F^4. \tag{3.11}$$

24

Thus the total exchange energy is

$$E_X = -\frac{e^2 \Omega}{\varepsilon_0 2^5 \pi^4} \mathbf{k}_F^4. \tag{3.12}$$

It can be shown that for the uniform electron gas[54,59]

$$\mathbf{k}_F = \left(3\pi^2 n\right)^{\frac{1}{3}} \tag{3.13}$$

and consequently, the exchange energy per electron is after some simplifications

$$\varepsilon_X = \frac{E_X}{N_e} = -\frac{3e^2}{2^5 \varepsilon_0 \pi} \left(\frac{3n}{\pi}\right)^{\frac{1}{3}}. \tag{3.14}$$

The exchange energy contribution follows from the antisymmetry of the wave function. For this reason it can be viewed as a *correlation* of electronic spins. Note that the actual term "correlation" energy is ambiguously reserved for the quantity of the difference between the total energy and the Hartree-Fock exchange energy where the basis set is assumed to approach completeness[53]

$$E_C = E - E_{HF}. \tag{3.15}$$

Also note that in the Hartree-Fock formalism, the energy is composed of an electrostatic Coulomb term, denoted by lowercase c, and an exchange term $E_{HF} = E_c + E_X$.

Contrary to the electron exchange energy, an analytic density functional for the correlation of the homogeneous electron gas is not known. Finding a suitable parametrization is deeply rooted in Møller-Plesset perturbation theory or configuration interaction methods.

Near exact Quantum Monte Carlo calculations for the correlation energy have been performed[60] and consequently, multiple different parametrizations for interpolating the data points have been published.[39,40] A particularly simple functional form was found in 2016[61] with only two parameters

$$\varepsilon_c(r_s) = a \ln\left(1 + \frac{b}{r_s} + \frac{b}{r_s^2}\right), \tag{3.16}$$

where

$$\frac{4\pi r_s^3}{3} = \frac{1}{n} \tag{3.17}$$

is the local Seitz radius, defined to be the radius of a sphere which contains exactly one electron.
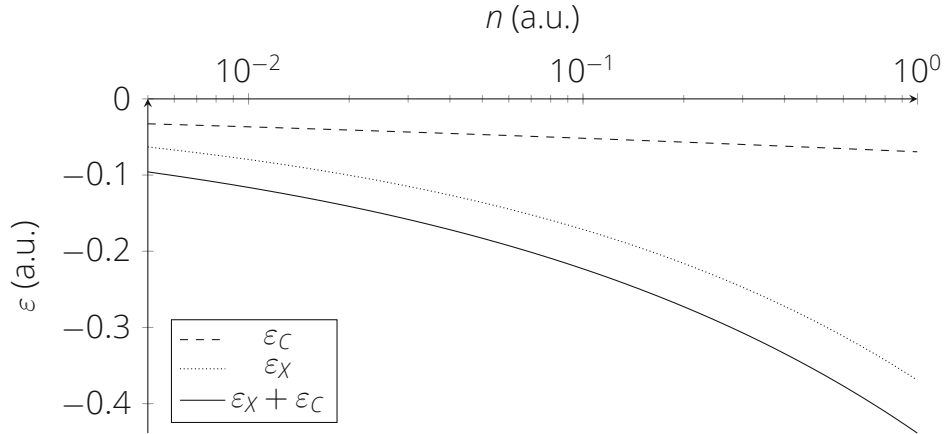
Figure 3.1: Exchange and correlation energy densities of the uniform electron gas with respect to the particle density in atomic units. Both curves meet at the origin.

3.1.2 Generalized Gradient Approximation

Due to its close relation to the uniform electron gas, LDA may be a suitable approximation for systems where the electron density varies relatively little. In the case of strongly varying density, a possibility to improve on LDA is to take information of the density gradient ∇n into account

$$E_{XC}[n] = \int \mathrm{d}^3\mathbf{r}\, f(n, \nabla n), \tag{3.18}$$

which is called *generalized gradient approximation* (GGA).

The most widely used GGA is the one devised by Perdew, Burke and Ernzerhof (PBE).[62] It is remarkable due to the fact that it is derived only by first principles and as such turned out to be suitable for a wide range of different systems.

The ansatz for both the exchange and correlation functionals is that they should converge to the result of the uniform electron gas in the limit of a vanishing density gradient. Otherwise they are modified by an attenuation function

$$E_X[n] = \int \mathrm{d}^3\mathbf{r}\, n(\mathbf{r}) \varepsilon_X^{\mathrm{unif}}(n) F_X(n, \nabla n), \tag{3.19}$$

$$E_C[n] = \int \mathrm{d}^3\mathbf{r}\, n(\mathbf{r}) \left(\varepsilon_C^{\mathrm{unif}}(n) + H(n, \nabla n) \right). \tag{3.20}$$

One of the immediate successes of GGA was the description of the ground state of magnetic iron. While LDA favors FCC iron, the application of a gradient

corrected functional correctly gives the BCC structure as the ground state in when magnetism is considered.

3.1.3 Meta-Generalized Gradient Approximation

Even more information about the degree of variation of the electron density can be obtained by considering its second derivative. The inclusion of the orbital kinetic energy densities

$$\tau = \sum_i^{N_e} \frac{1}{2m_e} \left| \nabla^2 \Psi_{s,i} \right| \tag{3.21}$$

defines the meta-Generalized Gradient Approximation (mGGA)

$$E_{XC} = \int d^3 \mathbf{r} \, n(\mathbf{r}) \varepsilon_{XC}(n, \nabla n, \tau). \tag{3.22}$$

A recently developed mGGA which satisfies all known exact constraints is the Strongly Constrained and Appropriately Normed (SCAN) functional.[63] Generally it can be expected to increase on chemical accuracy in comparison with PBE.

It is appropriate to note, that LDA, PBE and SCAN are all similar methods in a sense that they all use roughly the same amount of computational resources, although the predictive capabilities can vary significantly. For this reason, systematic errors of (semi-)local DFT like the underestimation of the band gap cannot be adequately avoided.

Using other non-local methods than DFT, e.g. the HF-approximation, or hybrid functionals such as HSE,[64] help to overcome these systematic errors but at the price of an increase in computational demand of several orders of magnitude.

3.2 The Projector Augmented Wave Method

In chemistry, interactions between atoms solely take place between valence electrons. Considering the core electrons with the same effort is thus not necessary. However, in the bonding region the wave function is smooth, whereas close to the nucleus it becomes highly oscillating due to the large attractive forces. Unfortunately, resolving highly oscillating wave functions numerically requires a finer grid and a larger basis set. As such even more computational effort would be necessary for the core electrons. Historically this problem has led to two different approaches.[65]

The Augmented Plane Wave (APW) method tackles this issue by separating the space into two regions and within these regions describe the wave function with a suitable basis set. Near the nucleus the wave functions are nearly atomic and thus expanded into spherical harmonics analogously to a partial wave expansion. This spherical region around the nucleus position is defined by a cutoff radius r_C. Outside this sphere the potential is weak and the wave functions may be expanded into plane waves. For the wave function to be continuous at the cutoff radius, the coefficients of the spherical harmonics can be expressed in terms of the coefficients of the plane waves.

In the pseudopotential approach the goal is to make the wave functions near the core smooth by replacing the Coulomb-potential with a pseudopotential which shows no singularity at the nucleus position. Again, at the cutoff radius, the smooth pseudo wave function should coincide with the standard wave function.
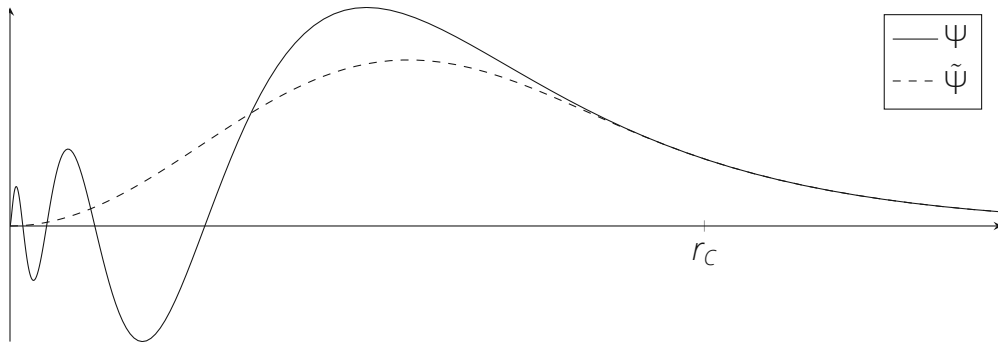

Figure 3.2: Illustration of the pseudopotential approach. The dashed line represents the wave function as obtained from the pseudopotential, whereas the solid line is a wave function following the Coulomb potential. Outside the cutoff radius, both functions overlap.

The Projector Augmented Wave (PAW) method[66] demonstrates a relationship between both ideas in a concise formalism. It requires a transformation between the KS wave function $|\Psi\rangle$ and the pseudo wave function $|\tilde{\Psi}\rangle$ in terms of a linear operator $\mathcal{T}$

$$|\Psi\rangle = \mathcal{T}|\tilde{\Psi}\rangle. \tag{3.23}$$

The wave functions should only be augmented near the nuclei within some augmentation sphere with radius r_C. The transformation operator reads

$$\mathcal{T} = 1 + \sum_{\alpha=1}^{K} \mathcal{T}_\alpha, \tag{3.24}$$

28

where each of the $\mathcal{T}_\alpha$ only acts in the augmentation sphere of nucleus α. This region separates the local electrons $|\varphi_i\rangle$ from the valence electrons, where the pseudo and all-electron wave functions are equal.
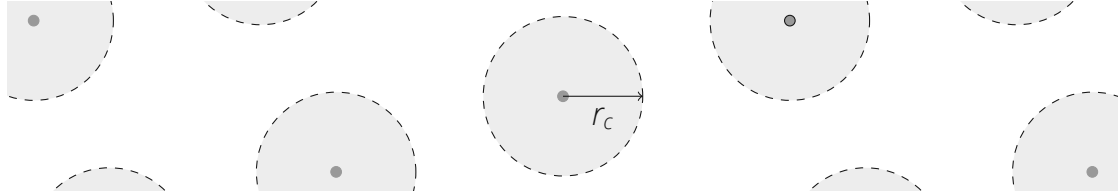

Figure 3.3: Illustration of the augmentation regions in the Projector Augmented Wave approach. Inside the cutoff radius r_c, the wave function is modified to decrease computational demand with minimal loss of chemical accuracy.

Because of Equation 3.24, it is also possible to construct pseudized core states

$$|\varphi_i\rangle = (1 + T_a) |\tilde{\varphi}_i\rangle \tag{3.25}$$

In this region, the KS wave functions $|\Psi\rangle$ as well as the pseudo wave functions $|\tilde{\Psi}\rangle$ are expanded into partial waves, i.e. into their core states $|\varphi_i\rangle$ and $|\tilde{\varphi}_i\rangle$, where i denotes a composite index of the quantum numbers n, l, m_l and m_s

$$|\Psi\rangle = \sum_i |\varphi_i\rangle c_i, \tag{3.26}$$

$$|\tilde{\Psi}\rangle = \sum_i |\tilde{\varphi}_i\rangle c_i, \tag{3.27}$$

with the same expansion coefficients c_i. As mentioned before, the transformation is required to be linear in $|\tilde{\Psi}\rangle$. Thus, the expansion coefficients need to be written as a scalar product

$$c_i = \langle p_i | \tilde{\Psi} \rangle, \tag{3.28}$$

with so-called projector functions $\langle p_i|$. When plugging this expression for c_i into the partial wave expansion for the pseudo wave function in Equation 3.27, it can be seen that $\sum_i |\tilde{\varphi}_i\rangle\langle p_i| = 1$ and hence

$$\langle p_i | \tilde{\varphi}_j \rangle = \delta_{ij}. \tag{3.29}$$

It is now possible to find an expression for the operator $\mathcal{T}$ by calculating

$$
\begin{aligned}
|\Psi\rangle &= |\tilde{\Psi}\rangle - |\tilde{\Psi}\rangle + |\Psi\rangle \\
&= |\tilde{\Psi}\rangle - \sum_i |\tilde{\varphi}_i\rangle c_i + \sum_i |\varphi_i\rangle c_i \\
&= |\tilde{\Psi}\rangle + \sum_i (|\varphi_i\rangle - |\tilde{\varphi}_i\rangle) c_i.
\end{aligned}
\tag{3.30}
$$

Together with Equation 3.28 and Equation 3.23, this means that

$$\mathcal{T} = 1 + \sum_i \left(|\varphi_i\rangle - |\tilde{\varphi}_i\rangle \right) \langle p_i| . \tag{3.31}$$

It is evident that three quantities are needed in order to construct $\mathcal{T}$.

$|\varphi_i\rangle$: As in APW approaches, these functions are the true KS-states in the augmentation region. They are obtained by solving the Schrödinger equation for the free atom. To account for the oscillations, their values are calculated on a radial grid.

$|\tilde{\varphi}_i\rangle$: Again, these functions are the solutions to the Schrödinger equation of the free atom, but with a pseudopotential $\tilde{V}_{n-e}$ instead of the Coulomb potential $V_{C,n-e}$. Constructing accurate pseudopotentials is a complex task that is described elsewhere.[67]

$\langle p_i|$: The projector functions follow from the orthogonality relation in Equation 3.29. The most general form for the projector functions is[66]

$$\langle p_i| = \sum_j \left(S^{-1} \right)_{ij} \langle f_j| , \tag{3.32}$$

where $S = \{ \langle f_k | \tilde{\varphi}_l \rangle \}$.

In a nutshell, the PAW-method combines earlier APW and PP approaches into a single framework. This method allows for faster calculations, since the core electrons are treated with less accuracy than valence electrons.

3.3 Neural Network Potentials

The introduction of the single-particle Kohn-Sham orbitals φ_i is necessary because a good approximation for an explicit functional of the kinetic energy operator with respect to the electron density n has not been found, i.e. $T_e \neq T_e[n]$ but $T_e \approx T_s[\{\Psi_s(\mathbf{r})\}]$. This results in a computational bottleneck to solve the Schrödinger equations with Kohn-Sham orbitals.

Because of the recent advancements made in the field of artificial intelligence and machine learning, scientists became aware of its extraordinary capabilities.[68] One of its tools are neural networks,[69] which are essentially a sophisticated way to fit an unknown function through data. Once a suitable fit has been obtained, its extrapolation capacities may be explored.

The idea of enhancing DFT with neural networks is straightforward:[19] First, the total energies are calculated for a sufficiently large dataset. The atomic positions and chemical species act as the input data, which in principle have a direct mapping to the total energy. In the second step, the neural network is trained on the data. Third, the total energy of new structures can be obtained by the neural network, without the need to solve the KS-equations, reducing the computational time by a large amount. It is hoped that the total error made by the extrapolation can be neglected.

It is advantageous to represent the input coordinates to the neural network in a smart way. While it would be possible to simply use the Cartesian coordinates of all the atoms, the network would have poor transferability to new structures, since the Cartesian coordinates cannot represent symmetries of the system.[19]

To account for this, the Cartesian coordinates may be transformed with a set of so-called symmetry functions. The assumption is that, in leading order, short range interactions contribute the most to the total energy and long range interactions are neglected.[19] The local surrounding of the atom is probed by parametrized symmetry functions multiplied with a cutoff function f_{ij}, which is defined to vanish outside of the cutoff radius r_c and inside it is monotonically decreasing. We choose

$$f_{ij} = \tanh^3 \left(1 - \frac{r_{ij}}{r_c} \right), \tag{3.33}$$

for atom i and neighbor j, the distance is $r_{ij} = |\mathbf{r}_i - \mathbf{r}_j|$.

By using a set of different parameters, an atomic "fingerprint" (AFP) can be calculated, which is a vector of real numbers representing the local surrounding of an atom. Each set of individual parameter values generates one dimension of the AFP.

Every atom has its corresponding neural network, where the weights and biases are trained for each chemical species respectively. After all neural networks predict an energy E_i, the total energy is taken as the sum of the individual energies

$$E = \sum_i^N E_i. \tag{3.34}$$

In this work we used weighted atom-centered symmetry functions[70] and apply a slight alteration to the approach to enhance its capabilities in crystal lattices. There are two types of symmetry functions:

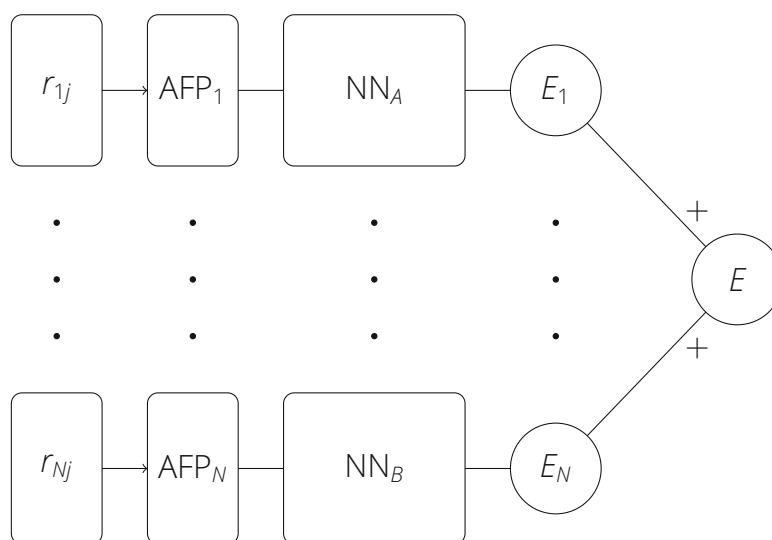- Radial symmetry functions probe only the distance between the nearest

Figure 3.4: The structure of the neural network potential is depicted. Vertically, there are N paths corresponding to each atom i in the system. At the very left the nearest neighbors are determined. Then, a unique atomic fingerprint (AFP) is calculated, which serves as the input to the neural network (NN), where each chemical species is represented by a NN with its weights, biases and structure. In this example, there are two chemical species labeled A and B. All N paths converge as the sum of the single output neurons E_i to yield the total energy E.

neighbors with parameters η and μ

$$W_i^{\text{rad}} = \sum_{j \neq i}^{N} g_{ij} e^{-\eta(r_{ij} - \mu)^2} f_{ij}. \tag{3.35}$$

For the weight function g_{ij} we calculate differences of oxidation numbers $g_{ij} = \max\{0.5, |ox_i - ox_j|\}$ and ox_i is the oxidation number of atom i. We choose this weight function because we assume the difference in oxidation state to be of great importance to the strength of the bond. μ and η control the center and the width of the Gaussians. Setting $\mu = 0$ and varying η generates central radial symmetry functions, while varying μ and η generates displaced Gaussians.
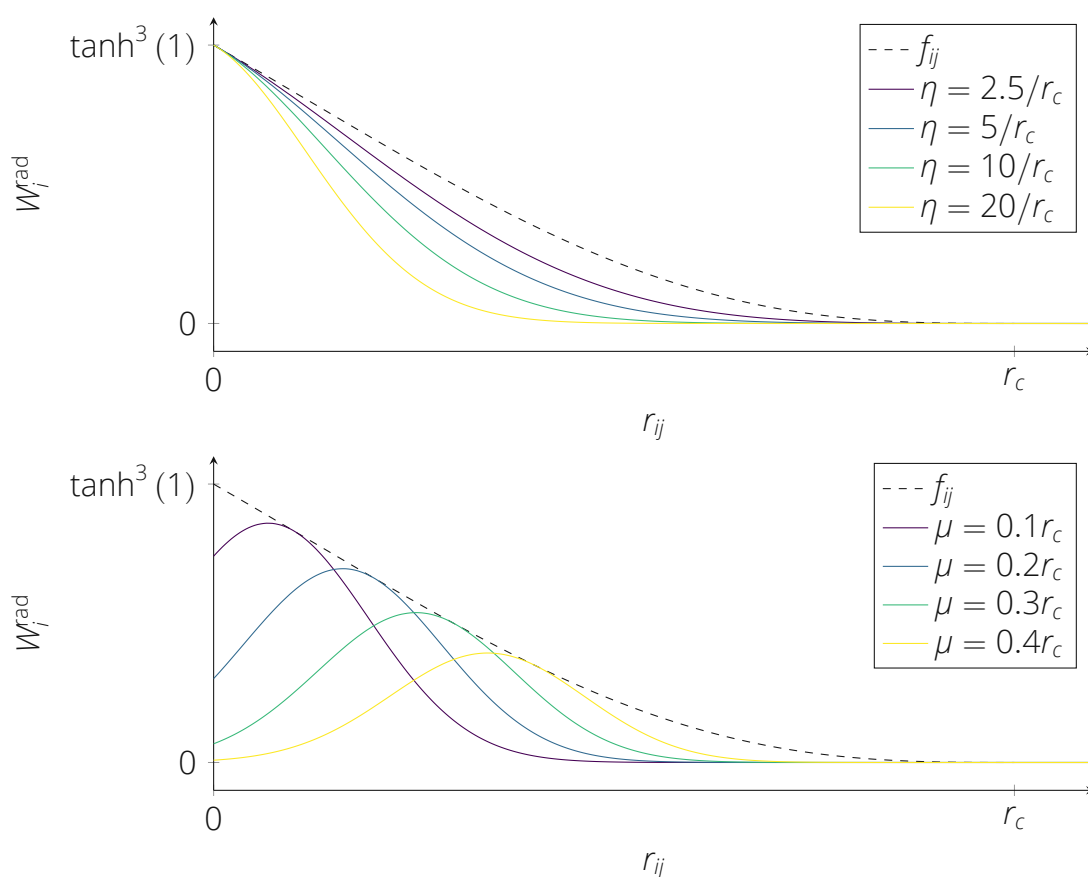
Figure 3.5: The radial symmetry functions and the cutoff function are shown. The cutoff function shows an almost linear decrease from $r_{ij} = 0$ with a smooth transition to the final value 0 after the cutoff radius r_c. Top: $\mu = 0$ (atom-centered) and η varies. Bottom: μ varies and η is fixed.

- Angular symmetry functions give information about the relative position-ing of two nearest neighbor atoms. The rotational symmetry of the angle θ_{ijk} is taken into account by using the cosine, the respective distances are again modeled by Gaussians

$$W_i^{\text{ang}} = 2^{1-\zeta} \sum_{j \neq i}^{N} \sum_{k \neq i,j}^{N} \tilde{g}_{ijk} \left(1 + \max\left\{\cos\left(\theta_{ijk} - \varphi\right), \cos\left(\theta_{ijk} + \varphi\right)\right\}\right)^{\zeta} \times$$

$$e^{-\eta\left(r_{ij}-\mu\right)^2} e^{-\eta(r_{ik}-\mu)^2} f_{ij} f_{ik}. \tag{3.36}$$

Here we adapt the weight function from the radial AFP to be the mean value for atoms i and j as $\tilde{g}_{ijk} = \frac{g_{ij}+g_{ik}}{2}$.
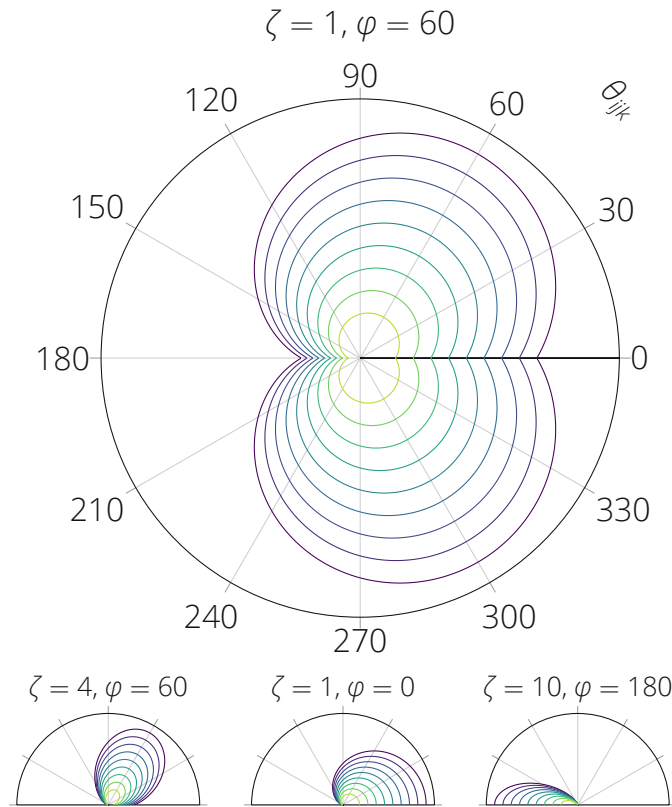

Figure 3.6: Angular symmetry functions in a polar plot are shown. The radial distances to the center are equal to their magnitude. The different levels cor-respond to several different distances r_{ij}. As ζ increases, the symmetry function becomes more directed towards the angle φ.

34

Part II

Results

Chapter 4

Magnesium Fluoride

4.1   Single Crystal

Magnesium Fluoride (MgF_2) occurs in nature as the mineral sellaite.[71] It has a tetragonal structure (rutile, space group 136) with lattice constants $a = 4.62\,\text{Å}$ and $c = 3.05\,\text{Å}$ making the ratio $c/a = 0.66$.[72] Mg occupies the position $(0, 0, 0)$ and F sits at $(0.30, 0.30, 0)$ thus the F anions form a distorted octahedron, with a distance to the closest cations of approximately $2\,\text{Å}$.[73]
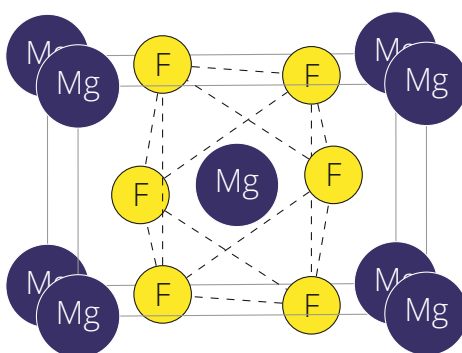

Figure 4.1: The conventional unit cell of MgF_2 is depicted. F anions form an octahedron around a Mg site, whose edges are also shown.

MgF_2 features strong ionic bonds, making it optically transparent. It demonstrates transmittance above at the Ly-α line at $10.20\,\text{eV}$ and beyond.[8] We calculate its band structure with the SCAN mGGA functional[63] and obtain a band gap of $\Delta = 8.03\,\text{eV}$, which shows the systematic underestimation of band gap energies within DFT.[74–76] A slice through the charge density is also shown in Figure 4.2.

36

It is often the case that the form of the electronic bands is not notably influenced by level of theory applied, only the size of the band gap changes, as we find in the next section on CaF_2. An estimate for the true size of the band gap can thus be given by multiplying the DFT gap by the experiment/DFT ratio for the band gap in the unit cell.[77,78] We make use of this method throughout this work when we want to emphasize possible experimental applications. Naturally, many body effects may alter the size of the band gap and as such cation is advised when interpreting these values.
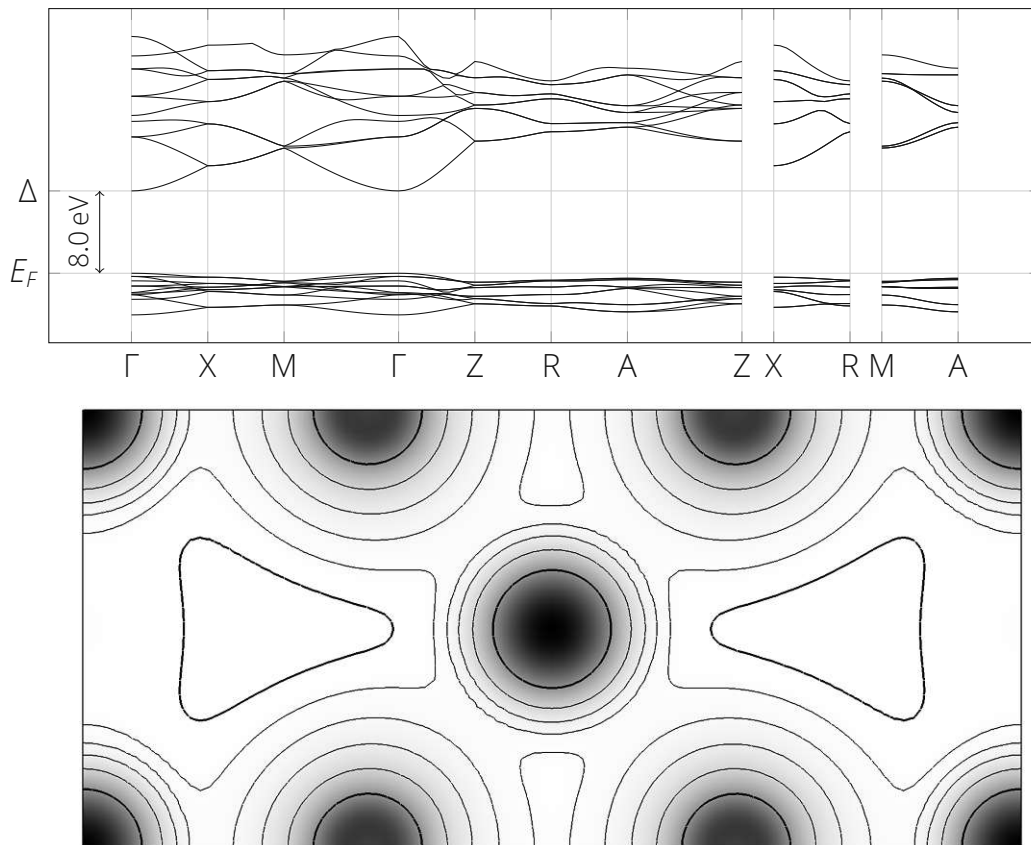

Figure 4.2: Electronic structure of MgF_2 in reciprocal and real space calculated with SCAN. Top: Band structure with the lowest global band gap at Γ. Bottom: Contour lines of the charge density through the $(1\bar{1}0)$ plane. In the very center and the corners are Mg cations, the rest are F anions.

4.2 Thorium Doping

4.2.1 Introductory Remarks

We have studied Th doped MgF_2 previously but made an important lapse concerning the charge compensation mechanism. In Appendix C.1.4 of Pimon [42] we did not consider a formation of additional MgF_2 ("crystal reference") for the Mg vacancy case and instead used the single crystal and gaseous variants $Mg + F_2$ ("atomic reference"). Naturally, the energy balance favors $E(MgF_2) < E(Mg + F_2)$, however the enthalpy of formation is experimentally obtained as $-12.7\,eV$ which is among the largest of the materials featured in the CODATA key values for thermodynamics.[79] Even though we obtain $-11.7\,eV$ with our choice of pseudopotentials, the overall energy balance is tipped in favor of the Mg vacancy instead of the published +2F interstitial configuration.

In a subsequent publication on the same topic, these considerations were also studied and the same conclusion was obtained.[80] However, there were two key differences in the computational parameters: 1. Their choice was a $2 \times 2 \times 2$ super cell, where $c = 6.1\,Å$. In our calculations, the distance between the Th and the Mg vacancy is about $2.4\,Å$ in **c** direction, meaning that in this case the impurity makes up a significant proportion of the whole cell. 2. They used LDA for the determination of charge compensation.

To get rid of doubt, we increased the accuracy of our previous SCAN calculations with a $4 \times 4 \times 4$ super structure by using an even higher energy cutoff of $1300\,eV$ and a similar convergence criterion for forces as in Barker [80]. These results were published elsewhere.[81] In agreement with Barker [80] we found the Mg vacancy to be energetically preferred.
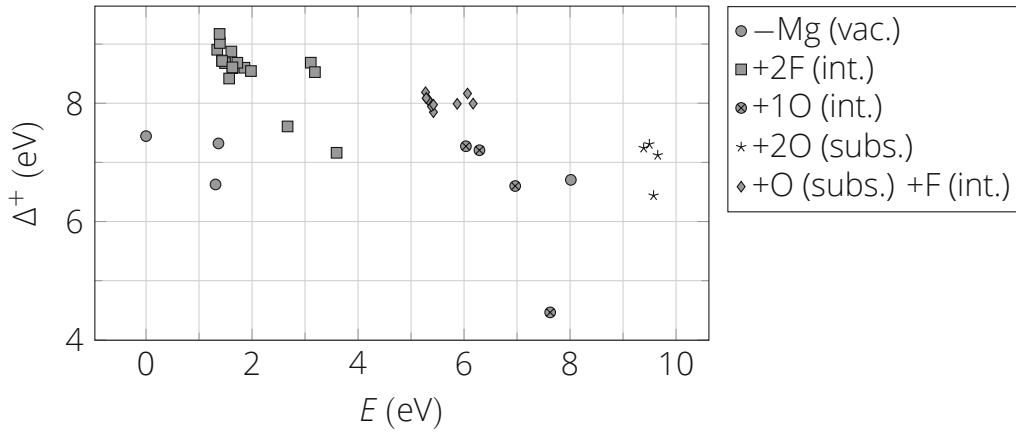
Unfortunately, some time after publication we discovered that the pseudopotential files were erroneously labeled on the VSC cluster*. Consequently, the Th potential we used didn't contain the necessary kinetic energy densities required for SCAN calculations. Thus we repeated our published calculations but used the `F_GW_new` pseudopotential and a lower cutoff of $500\,eV$ to greatly decrease computational demand. At the same time we took the opportunity to also consider configurations where an O atom replaces an F atom and more chemical pathways including the MgO crystal, both of which has not been done previously. The results are still consistent with the published findings and are shown in the following.

---

*This issue has been immediately resolved by the VSC team (Jun. 18th 2021)

4.2.2 Charge Compensation Study

Since the oxidation state of Th is 4+ in a broad range of compounds[80] and Mg is 2+, we consider different types of charge compensation mechanisms, which compensate for two electrons when Th substitutes Mg: A Mg vacancy, +2F interstitial, +1O interstitial, +2O substitutional and +1O substitutional and +1F interstitial. Favorable chemical pathways outside of the crystal are molecular F_2 and O_2 as well as solid Mg, MgO and MgF_2 crystals. We neglect phases which we do not expect to occur at room temperature such as e.g. F or O crystals or gaseous Mg.

The Mg vacancy is energetically favored but has a lower band gap compared to +2F interstitial doping types. It is also very unlikely that oxygen plays a role for charge compensation in Th:MgF_2.

Figure 4.3: The total energy E and the respective scaled band gap $\Delta^+ = \frac{10.20}{8.03}\Delta_{DFT}$ for calculated configurations is compared. Note that the different stoichiometries inside the crystal have been accounted for in the total energy E. Off the chart are Th interstitial placements with +4F (int.) at 12.0 eV and +2O (int.) at 19.7 eV respectively.

atom exchange				
in	out	E (eV)	Δ^+ (eV)	Path
	-2Mg	0.0	7.4	$2MgF_2 + O_2$
$+2$F	-1Mg	1.3	8.9	$MgF_2 + O_2$
$+1$O	-1Mg	5.3	7.9	$MgF_2 + F_2 + {}^1/2O_2$
$+2$O	-2F -1Mg	9.4	7.2	$MgF_2 + 2F_2$
$+4$F		12.0	7.9	O_2
$+2$O		19.7	5.3	$2F_2$

Table 4.1: Details for the most favorable configurations of each stoichiometry in a chemical environment containing the MgF_2 crystal and additional $2\,F_2$, $1\,O_2$ and 1 Th is shown. This set of compounds should represent the system when the dopant is introduced via ThF_4. The first two columns denote the extra or vacant atoms around the impurity omitting Th. Next follow the relative energies and scaled band gap values. The rightmost column shows the energetically preferred chemical path for compensation outside of the crystal. Added together we consider 42 different configurations.

Chapter 5

Calcium Fluoride

5.1 Single Crystal

Calcium Fluoride (CaF_2) occurs in nature as the abundant mineral fluorite. It shows a face centered cubic (FCC) structure (space group 225), with a lattice constant of 5.46 Å where the ion Ca occupies the position $(0, 0, 0)$ and F anions are at (¼,¼,¼) and (¼, ¼, ¾), making the Ca – F bond length 2.37 Å.[82,83]
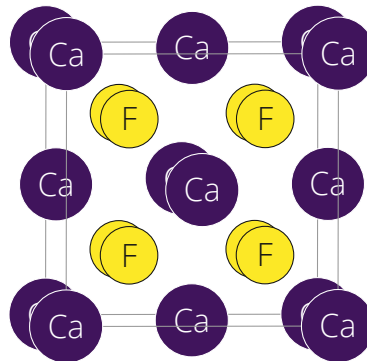
Figure 5.1: Conventional fcc unit cell of CaF_2.

Because of the different electronegativities of Ca and F, the crystal exhibits ionic bonding and is an insulator,[84,85] which is visualized by the analysis of the charge density in Figure 5.2 and the band structure in Figure 5.3. Its experimentally measured band gap ranges from 10 eV to 12 eV.[9,10]
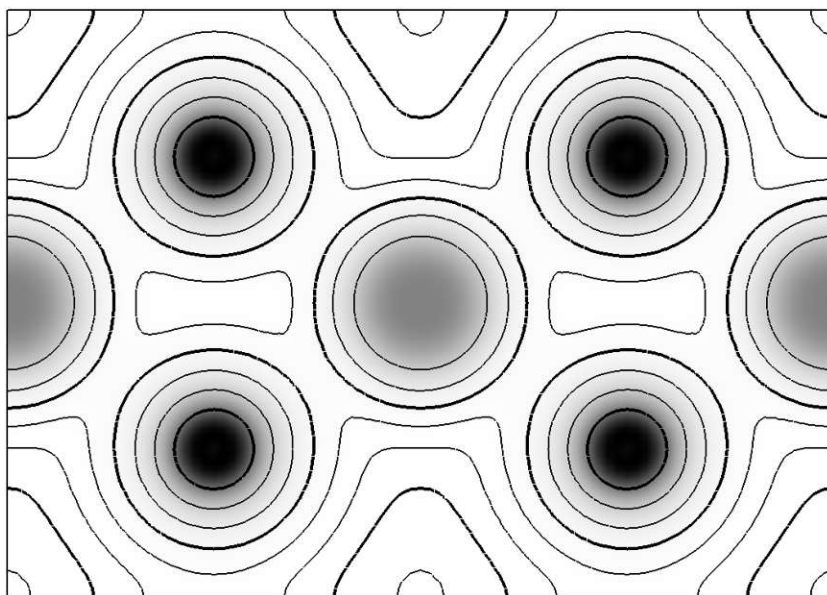
Figure 5.2: Slice of the charge density with isosurfaces along the (1$\bar{1}$0) plane. Darker regions represent more charge at the position of the F atoms, gray regions is less charge at the Ca atoms. Due to the localized density with small overlap and the charge distribution, the strong ionic character of the bonds is evident.
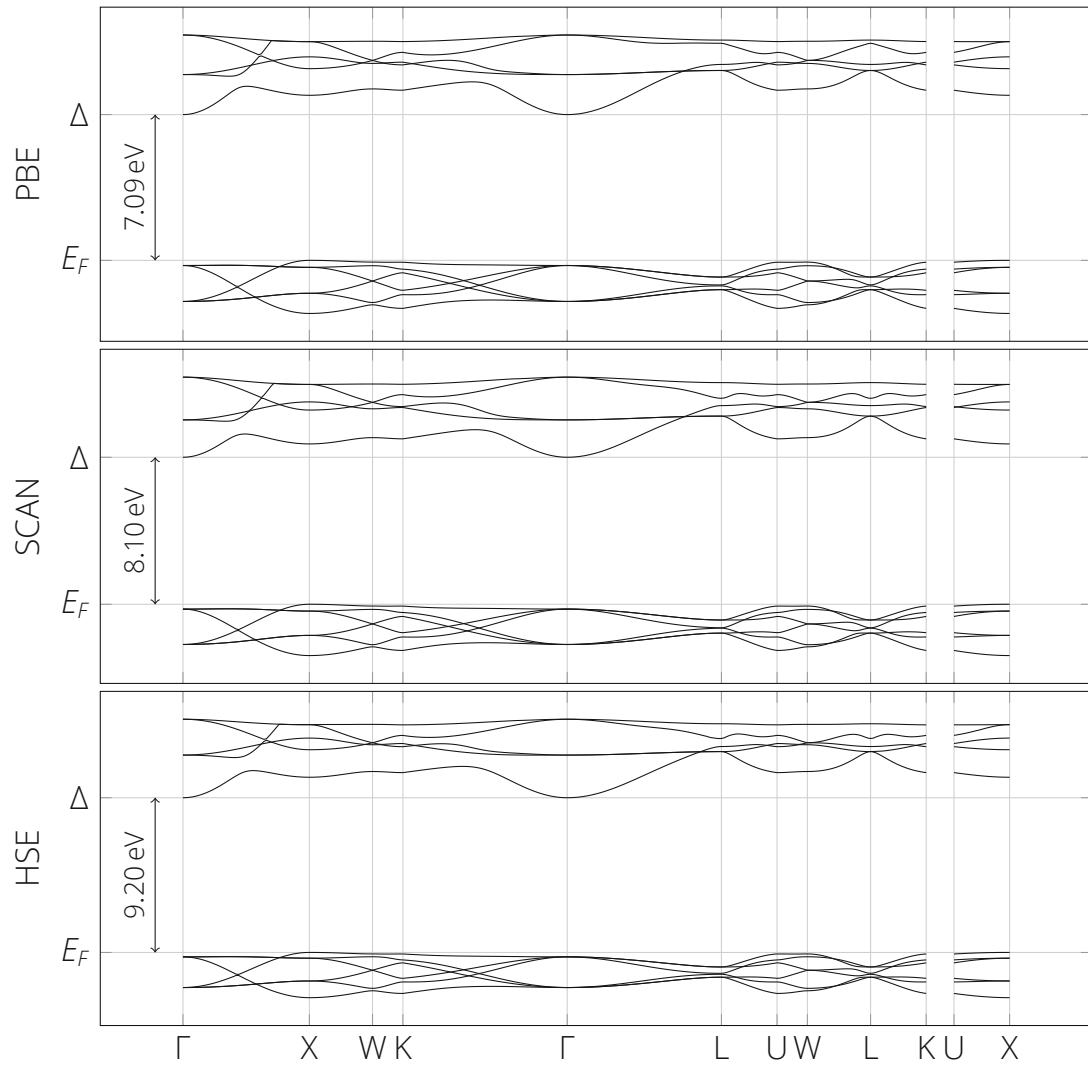
Figure 5.3: The band structures for CaF_2 calculated with different levels of theory are shown. The qualitative form of the bands stays the same while only the Gap Δ changes in size. The material shows an indirect band gap from $X \rightarrow \Gamma$.

5.2   Thorium Doping

5.2.1   Charge Compensation Mechanism

Because of its high band gap, CaF_2 is a suitable candidate as a host crystal for a potential nuclear clock. In the same manner as MgF_2, Th creates a charge imbalance when doped into CaF_2 due to the different oxidation numbers of Th and Ca.[86,87]

In a previous study, the most probable configuration for Th:CaF_2 was determined to include two interstitial fluorines, where Th substitutes a Ca atom. The two fluorines would be in the vicinity, with an unrelaxed configuration of a 90° angle. Note that after relaxation the angle changes. The study was performed with both HSE and PBE xc-potentials and a $2 \times 2 \times 2$ unit cell.[88]

We aim to improve this calculation by choosing a lower doping concentration with one Th per $3 \times 3 \times 3$ unit cells and more chemical pathways to compare the individual types of compensation. The different mechanisms investigated are a vacancy of calcium, 2 interstitial fluorine, 2 oxygens substitute fluorines, and 1 interstitial oxygen.

In addition, we consider more chemical pathways outside of the crystal including molecular F_2, O_2 and OF_2 as well as solid Ca, CaO and CaF_2 crystals. This set of elements should resemble the chemical composition during crystal growth. We neglect phases which we do not expect to occur at room temperature such as e.g. F or O crystals or gaseous Ca.
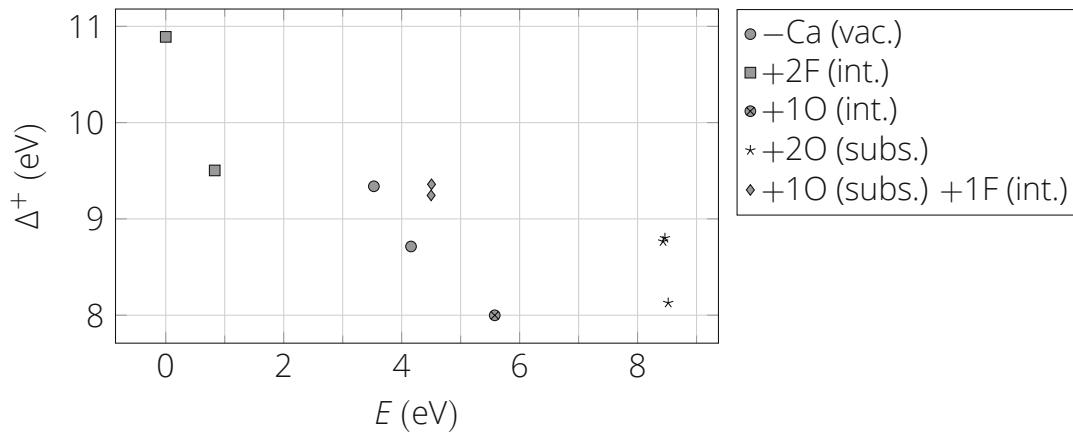

Figure 5.4: This plot depicts scaled gap sizes $\Delta^+ = \frac{11.8}{7.09}\Delta_{DFT}$ and energies of the investigated configurations. Coincidentally, the most probable configuration also shows the largest gap size. In Th:CaF_2, the gap size tends to get smaller the less probable a configuration is.

| atom exchange | | | | |
in	out	E (eV)	Δ^+ (eV)	Path
+2F		0.00	10.89	O_2
	−1Ca	3.53	8.71	$CaF_2 + O_2$
+1O		4.50	8.00	OF_2
+2O	−2F	8.68	8.80	$2F_2$

Table 5.1: Details for the energetically lowest configuration in each stoichiometry in a chemical environment containing the Th:MgF_2 crystal (substitutional doping) and additional 1 F_2, 1 O_2 is shown. This set should resemble the system when the dopant is introduced via ThF_4, since the substitutional Ca can be assumed to join with F_2 to produce CaF_2. The first two columns denote the change in atomic number with respect to a Th:CaF_2 crystal, that has substitutional doping of thorium for calcium and no charge compensation. Next follow the energies and scaled band gap values. The rightmost column shows the preferred chemical path for compensation outside of the crystal. Added together we consider 10 different configurations.

We confirm that two interstitial Fluorines are energetically favorable. Remarkably, these systems also show the highest band gap. The final arrangement of the two interstitial fluorines shows a 71.09° F–Th–F angle and a Th–F distance of 2.30 Å.
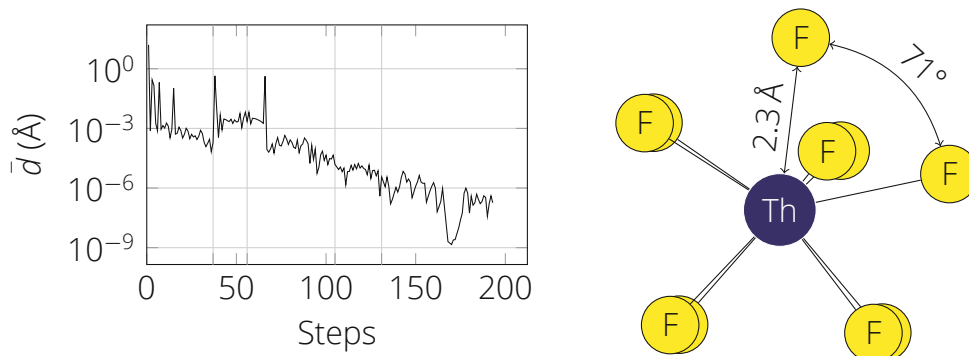

Figure 5.5: Relaxation of the impurity in Th:CaF_2. Left: The average ionic displacement per ionic step. Right: Final configuration. Note that the perspective is slightly turned out of the axis of symmetry to visualize all 10 F ions. In order to make room for the two interstitial F ions, there is a shift in positions of the original arrangement with the closest F ions being pushed outwards.

5.2.2 Fluorine Defects

So far we considered CaF_2 doping via melting the crystal and adding ThF_4 compounds. Now we choose a more general approach of considering ThF_n compounds but only 2 F are required for charge compensation leaving $n - 2$ F unaccounted for. In the following, we aim to find the energetically most favorable configuration of these surplus F anions inside the crystal as additional defect and determine the energy balance compared to gaseous F_2.

Even for high doping concentrations there are many more CaF_2 unit cells available than there are surplus F atoms. We consider it therefore to be sufficient to compare cases for $2 \times 2 \times 2$ unit cells where $n_F = 1, 2, 3, 4, 5, 6$ interstitial F atoms surround a Ca atom.

Interstitial positions before the relaxations are in vacant spaces between the lattice sites. These can be imagined as the face centers of a cube with the same orientation as the unit cell and with an edge length of $2 \times$ Ca−F distance and Ca in its body center. Due to the high symmetry of the lattice, we need only consider one configuration for the +1F, +5F and +4F cases, two configurations in the +2F case ($\angle$F−Ca−F = $\{90°, 180°\}$) and two configurations for the +3F and +4F cases. For both latter defects, one configuration has all interstitial fluorines on one plane, while the other has one interstitial fluorine perpendicular to the plane of the other interstitials.

A way to arrive at comparable energies is to add these $2 \times 2 \times 2$ structures with and without the defect, such that the amount of particles is the same in all cases. The total number of cells to add is computed by the least common multiple (lcm) of the set of surplus F, in this case $lcm(1, 2, 3, 4, 5, 6) = 60$. First, $m = 60/n_F$ CaF_2 cells with the defect are added such that there are a total of 60 interstitial Fluorines and subsequently $60 - m$ cells without defects are summed to arrive at the same number of particles. We divide the result by 60 to get an energy equivalent per surplus F.

We find that it is energetically favorable for 3 surplus F atoms to group up in the Ca vicinity. From their highly symmetric starting positions forming 90° angles respectively as measured from the central Ca atom, they relax in a configuration where, together with a fluorine from the original lattice, they form a regular tetrahedron with an edge length of 2.69 Å. This tetrahedron is located in between four Ca lattice positions which also form a regular tetrahedron with an edge length of 3.80 Å, such that, if one would make a compound of these two tetrahedra, the F and Ca atoms would alternately occupy the vertices of an (irregular) cuboid, because each F−Ca−F angle is 69.51° and the Ca−F−Ca angle is 107.16°.

In any case, the energy difference of solid F:CaF_2 and molecular F is 0.40 eV, corresponding to a Boltzmann-Factor of $e^{-\beta\Delta E} = 94.34\%$ at the crystallization

#F	1	2	3	4	5	6
E (eV)	0.21	0.12	0.00	0.19	0.06	0.15
E_+ (eV)	—	0.12	0.00	0.05	0.05	0.00
E_G (eV)	0.61	0.52	0.40	0.45	0.45	0.40

Table 5.2: Relative energies of a varying number of surplus Fluorine atoms. The first row displays the energy differences for $2 \times 2 \times 2$ super cells of CaF_2, where all n_F surplus Fluorines are in the vicinity of a central Ca atom. The second row shows the energy balance when we allow combinations of different n_F configurations to reach the same number of particles. The change in values for 4, 5, and 6 F atoms is due to the low energy of the +3F configuration, which enables the energetically lower $(1 + 3)$F, $(2 + 3)$F and $(3 + 3)$F arrangements to spread out over two super cells. The third row corresponds to the second, however the energy reference is molecular F_2, which is always preferred.

point $T = 1691$ K. Since the constituents of a defect originate from the lattice, the band gap is not notably reduced.
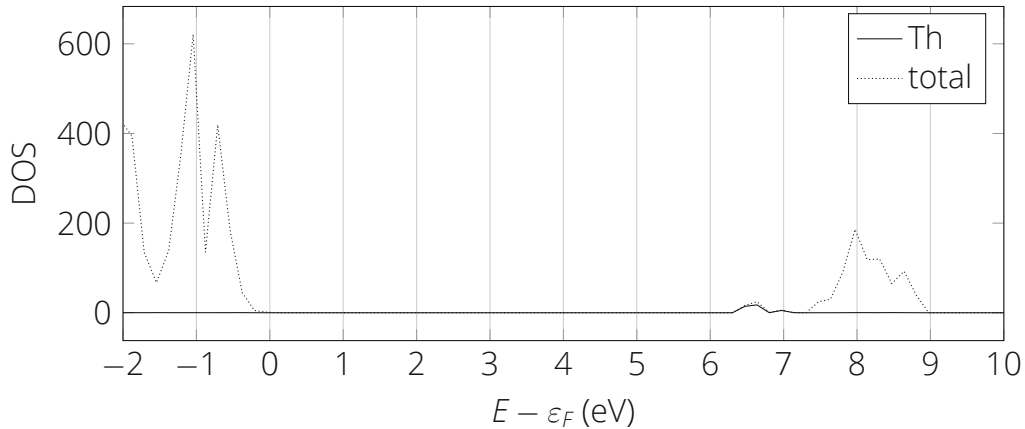
5.2.3 AE-KS Wave Function

Figure 5.6: Electronic density of states for the most probable Th:CaF_2 configuration. Localized Th-states are at the upper edge of the band gap.

Th:CaF_2 is currently under investigation as a host crystal for the application of a nuclear clock.[89] However, from both the uncertainties of DFT's band gap and the energy level of the Th isomer state, it is not clear whether the nucleus

47

can be excited by a laser pulse. In any case, the electronic and the nuclear levels might be energetically very close together. This could trigger a mechanism called electron-bridge, where an electron transfers its energy to the nucleus instead of dissipating a VUV photon.

Due to the very weak periodicity of the dopant in the crystal lattice, there will be atomic-like f-states at the edge of the band gap localized around the Th nucleus. Naturally these will be also composed of a mixture of spherical harmonics, including s-states, which have a non-vanishing probability density at the nucleus.

In case an excited electron occupies one of these valence states, we speculate that there is a possibility that it will in turn excite the nucleus via a virtual electronic state, which has the isomer energy. Thus it is of interest to obtain the wave function of the thorium electronic states overlapping with the crystal conduction band states.

Since VASP uses the PAW-method,[66] the resulting pseudo wave function cannot be directly applied to the above mentioned mechanism. The next step was thus to try to calculate these wave functions with all-electron DFT codes (CP2K, pySCF)[90–92] but unfortunately we were not able to converge the electronic states. We also tried out GPAW which provides an all-electron wave function reconstructed from the pseudo wave function, however in the open source version thorium pseudopotentials were not available.[93,94] We thus had to return to VASP and modified the source code in order to calculate the required all electron wave functions from their pseudized counterpart.[95]

However, we had to accept three limitations from our approach, which are a direct result from our modifications to VASP's code: 1. We cannot use spin-orbit coupling. 2. We can only do a calculation at the Γ-point while using VASP's `complex` version. 3. We must perform the calculation on a single core (on some architectures a single node may be possible).

Because of Th's relatively high charge, point 1 is especially notable. The other two points are dependent on each other: Since we only have one core for the SCF loop, we are restricted in size of the system, which in turn lowers the validity of a Γ-only choice.

As a compromise, we use a $2 \times 2 \times 2$ super structure, with the +2F (int.) charge compensating configuration. Because we want to calculate the structure with the HSE functional and the pseudopotential for F is mainly responsible for the high energy cutoff requirements in our previous calculations, we use the soft `F_s` pseudopotential and set the cutoff to 400 eV.

To prioritize accuracy around the nucleus we calculate the wave function on a radial grid. We use the grid points in **r** direction as specified by the partial waves in VASP's `POTCAR` file. These grid points start at about 10^{-5} Å from the

nucleus and increase in exponentially spaced distances (from approximately 10^{-5} Å to 10^{-1} Å) to about 4.30 Å from the Th position. Note that this is far larger than the actual PAW-sphere which is given in the pseudopotential as being 1.80 Å.

As the grid is very dense around the nucleus, a simple linear interpolation is used between each grid point. However, in order to get wave function values arbitrarily close the nucleus, we have to extrapolate from the calculated data.

Reminiscent of the radial solutions of Schrödinger's equation for the hydrogen atom, our extrapolation function is $f(r) = \Psi_0 \exp(-ar)$, corresponding to states similar to $l = 0$, which can have a non-vanishing value at the nucleus. Ψ_0, the value of the wave function at the origin, and a are parameters. For each pair of (θ, φ), we perform an extrapolation in $\mathbf{r} \to 0$ direction.

However, with increasing distance the fit function becomes less representative, thus the number of data points used for the fit is also a parameter. We determine this systematically by adding an uncertainty on each data point which is proportional to r^n and optimize for the number n under the condition that the fits in all directions coincide at the origin as best as possible. As it turns out, the number n is usually quite large, suggesting that almost all of the s-character of the wave function is given by the closest couple of grid points.

To verify that we did the AE-KS reconstruction of Ψ correctly, we compare the two products $\Delta\Psi = \langle\widetilde{\Psi}_i|S|\widetilde{\Psi}_i\rangle - \langle\Psi_i|\Psi_i\rangle \overset{!}{=} 0$, where the product with the overlap operator $S = 1 + \sum_{ij} |\widetilde{p}_i\rangle \left(\langle\varphi_i|\varphi_j\rangle - \langle\widetilde{\varphi}_i|\widetilde{\varphi}_j\rangle \right) \langle\widetilde{p}_j|$ does not depend on the reconstructed AE-KS states.

To summarize the results in Table 5.3, the extrapolation works well when values of the probability density at the nucleus Ψ_0^2 are large. Out of 7 localized Th-states, we identify one which has a relatively large contribution at the nucleus position. The overall electron-bridge transition-rates also depend on the overlap with the conduction band states and their energy differences. In two publications, these rates were calculated and discussed using the wave functions provided.[20,21]

5.2.4 Lattice Vibrations

Under experimental conditions, the material may be subject to moderate temperatures and lattice vibrations may alter the optical properties of the crystal. These effects can be studied by calculating phonon modes of the super structure. As described previously, 3D lattices include a great number of interactions and in particular long range interactions spanning more than one unit cell may become important. Therefore, it is imperative to calculate phonons on large
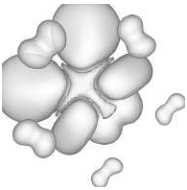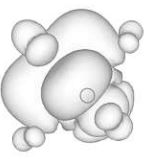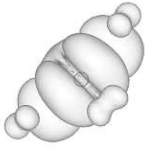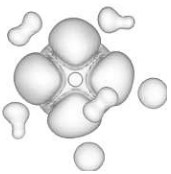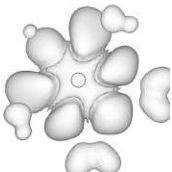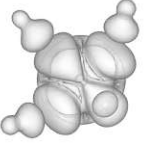
Band	v_1	v_2	v_3	v_4
E (eV)	6.190	6.637	6.696	6.703
Loc. (%)	95	95	97	97
$\rho(\mathbf{r})$				
$\Psi_0^2(\text{Å}^{-3})$	7.75e−5	9.35e−2	3.35e−6	9.83e−4

Band	v_5	v_6	v_7	
E (eV)	6.777	6.809	6.851	
Loc. (%)	96	96	94	
$\rho(\mathbf{r})$				
$\Psi_0^2(\text{Å}^{-3})$	3.39	5.04e−5	6.19e−4	

Table 5.3: Energies, localizations, band decomposed charge densities and extrapolation results for the HSE calculation of the favorable +2F (int) configuration in Th:CaF$_2$ are shown. The Th nucleus is illustrated as a circle and surrounding p-states originate from neighboring F-positions.
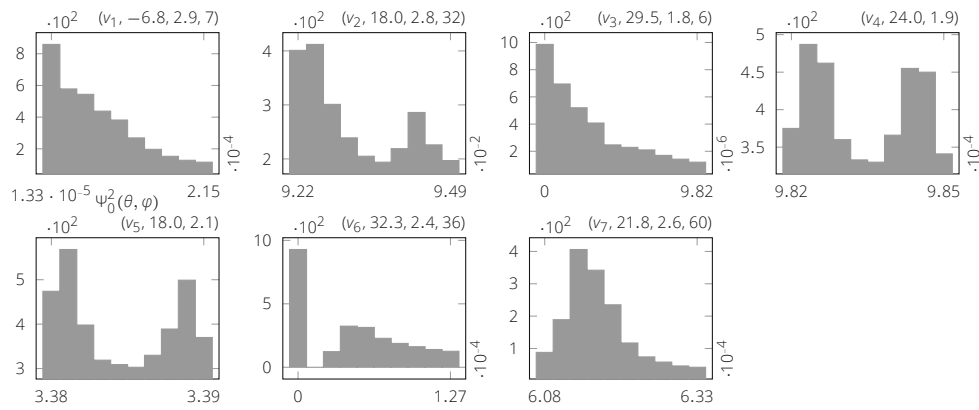
Figure 5.7: Numerical tests to estimate the uncertainty of the AE-KS reconstruction (Table 5.3) are shown. The figures are histograms for the wave function value at the origin Ψ_0^2 for the selected valence states on Th, where individual values are obtained from extrapolations along each (θ, φ) direction. Angular spacing is such that $\Delta\theta = \Delta\varphi = 2°$. Brackets on top of each plot are to be read as: (state label, uncertainty exponent n, $100 \times \Delta\Psi$). For some states, the fourth number measures the percentage of extrapolations in (θ, φ) directions which do not coincide at the origin and are omitted in the histogram. We find that v_5 dominates the result being at least two orders of magnitude larger than all the others. Note that for v_5 all extrapolations coincide.

cells. However the caveat is of course that the number of displacements for the numerical analysis is directly dependent on the number of atoms.

We consider the 3×3×3 super structure as the best compromise that is possible with respect to the computational limits. We use the code phonopy[96] to generate the displacements, VASP to calculate the configurations and phonopy again to analyze the results. Displacements are determined using phonopy's default parameters for symmetry detection. In total we calculate 1032 displacements.

We assume that the greatest impact on the optical properties are modes where the Th and a neighboring atom oscillate in anti-phase. For each q-point and each band, we analyze the eigenvectors of Th and its neighboring atoms and assign each mode a dimensionless value

$$\text{Score} = \left| \frac{\|\mathbf{d}_{ij}\|}{\|\mathbf{r}_{ij}\|} - 1 \right|, \tag{5.1}$$

where $\mathbf{d}_{ij}$ is the difference between the real parts of the phonon eigenvectors $\mathbf{x}$ for Th and the neighboring atom plus their spatial positions respectively, i.e. $\mathbf{d}_{ij} = \mathbf{r}_i - \mathbf{r}_j + \mathbf{x}_i - \mathbf{x}_j$ and $\mathbf{r}_{ij} = \mathbf{r}_i - \mathbf{r}_j$ is the distance vector between the atoms. This score should represent a measure for the relative difference of the atomic positions at rest and in the vibration mode.

The modes with the largest score lie around 9.80 THz and 10.10 THz. Their occupation can be avoided if the sample is cooled (see Figure 5.8).

5.3   Electric Field Gradients on other Dopants

An experimental way to determine whether the Th nuclei are in fact in the excited isomer state is nuclear quadrupole resonance (NQR) spectroscopy. The non-spherical charge distribution of the bonding valence electrons create an electric field gradient (EFG) at the nucleus, which interacts with the nuclear quadrupole moment Q, causing a level splitting in nuclear states depending on Q, which has a different value for the nuclear ground state and the excited state.

However, the ^{229}Th isotope is rare and thus not feasible for calibrating and testing the experimental setup. More readily available elements are Ac, Ce, Np and U, which offer the additional advantage that there exist values for Q for some of the isotopes in the literature.[97] The EFG on U:CaF$_2$ has been determined previously,[98] as such we focus on Ac, Ce and Np. As a first step, we need to affirm the oxidation state of the doped ions in the CaF$_2$ crystal. Because of the studies performed for Th doping, we assume an interstitial F configuration
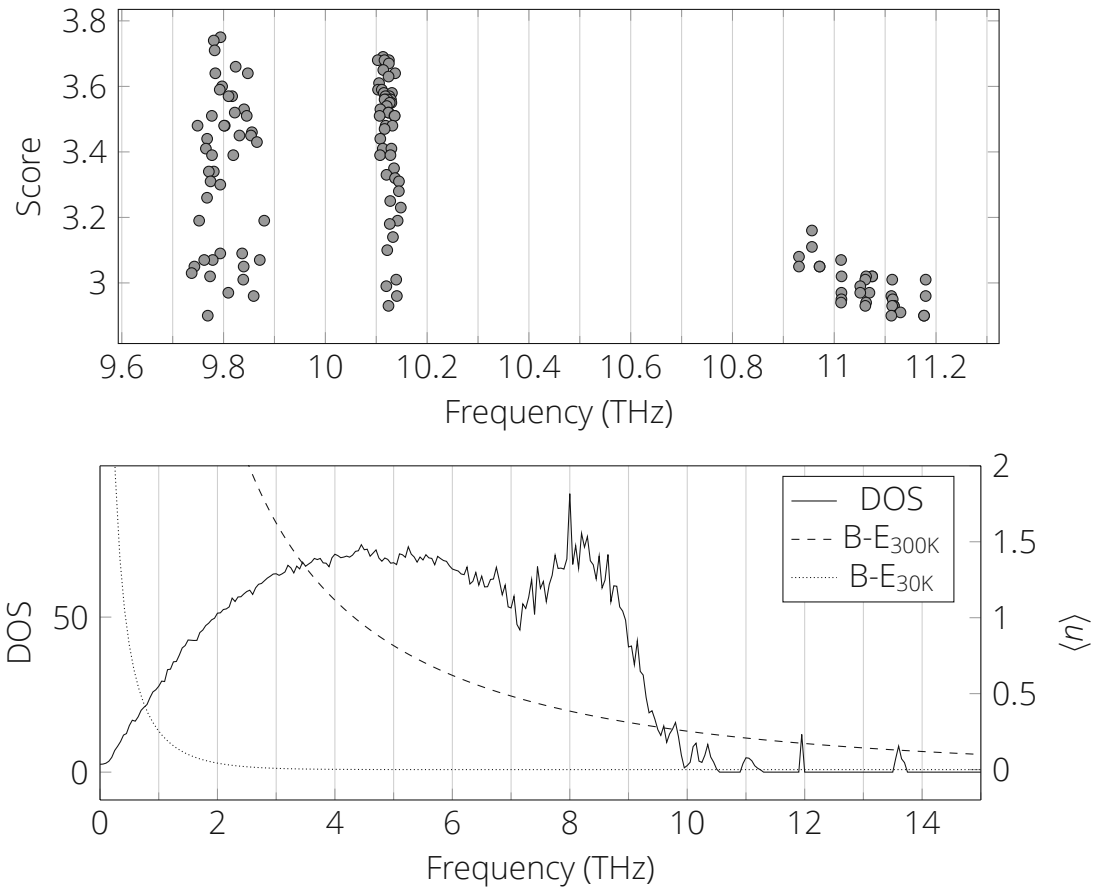
52

Figure 5.8: Top: Estimated impact of selected phonon modes over frequency. Displayed are 130 of the modes with the highest score as described in the main text. There are a few outstanding modes around 9.80 THz and a little above 10.10 THz. Bottom: Phonon density of states (DOS, solid line, left axis) and Bose-Einstein statistics (B-E, dashed line, right axis) at 300 K and 30 K.

and vary the number of interstitial atoms. In the experiment, the doping concentration can be higher than with [229]Th, as such the case of a $2 \times 2 \times 2$ CaF$_2$ super structure is sufficient.

	2+	3+	4+	5+	6+	7+
Ac	5.86	0				
Ce	7.87	2.40	0			
Np	10.15	4.87	1.50	0	0.15	0.48

Table 5.4: Determination of oxidation states of heavy elements based on a +F (int.) charge compensation analysis on a $2 \times 2 \times 2$ super structure of doped CaF$_2$ with values given in eV.

The most probable configurations are +1F, +2F and +3F interstitials for the dopants Ac, Ce and Np respectively. For these configurations, the electric field gradient reads:

	V_{zz} (V/Å^2)	η
Ac	-222.211	0.000
Ce	115.807	0.158
Np	329.064	0.751

Table 5.5: EFG values for doped CaF$_2$ on the dopant for the most favorable charge compensating configuration. Calculations were performed with PBE and symmetry switched off.

Level	V_{zz} (V/Å^2)	η
SCAN	301.054	0.871
B3LYP	319.021	0.765
PBE0	318.381	0.757
HSE06	316.827	0.757

Table 5.6: For the +3F Np configuration we also compute the EFG for different levels of theory: mGGA SCAN and hybrid functionals B3LYP, PBE0 and HSE.[63,64,99–102]
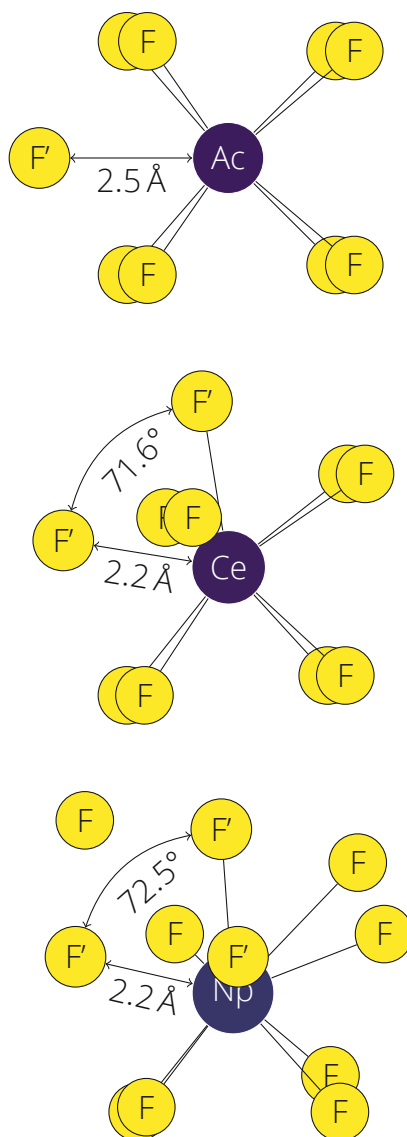
Figure 5.9: Relaxed structures for three heavy elements doped into CaF_2 with the energetically lowest charge compensation mechanism. Interstitial F anions are marked as F′. Top: Ac (one excess electron) doped into CaF_2. Middle: Ce (two excess electrons) is in the same group as Th and also the charge compensation mechanism is similar. Bottom: Np (three excess electrons) has three interstitial F ions that relax in a peculiar configuration. The final structure is reminiscent of a +2F configuration like in Ce or Th doped CaF_2, but with the exception that an original F atom is pushed outwards (upper left corner). The distance from Np to this F anion is 3.8 Å, arguably too far away for meaningful bonding but still relevant for the compensation energy.

Chapter 6

LiCaAlF$_6$

6.1   Single Crystal

LiCaAlF$_6$ (LICAF) does not appear naturally but instead was developed for use as the active medium of an UV tunable solid-state laser.[103] We find experimental band gap sizes to be at 12.7 eV and 11.1 eV.[11,12] Indeed, the band structure in Figure 6.2 features extremely flat bands. The material shows a relatively elaborate trigonal crystal system with a ratio of $c/a \approx 1.9$ in the unit cell.[18]
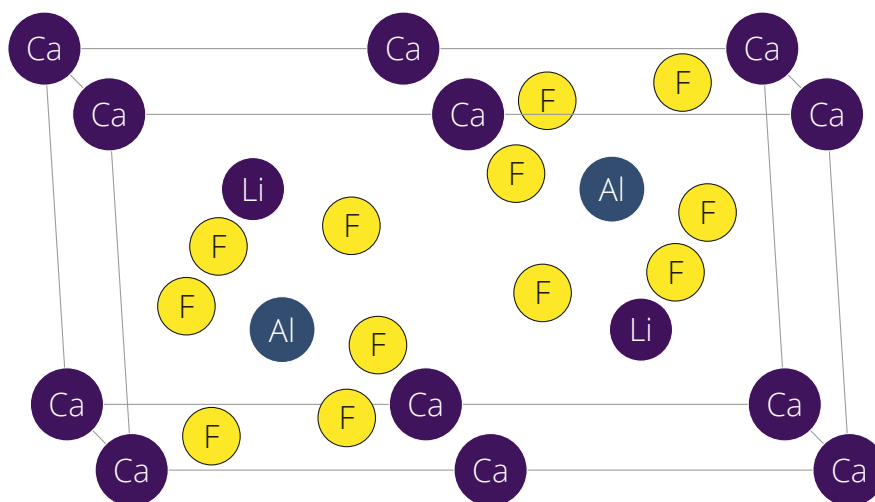

Figure 6.1: This unit cell of LICAF contains 12 F anions and 2 Li, Ca, Al cations respectively.
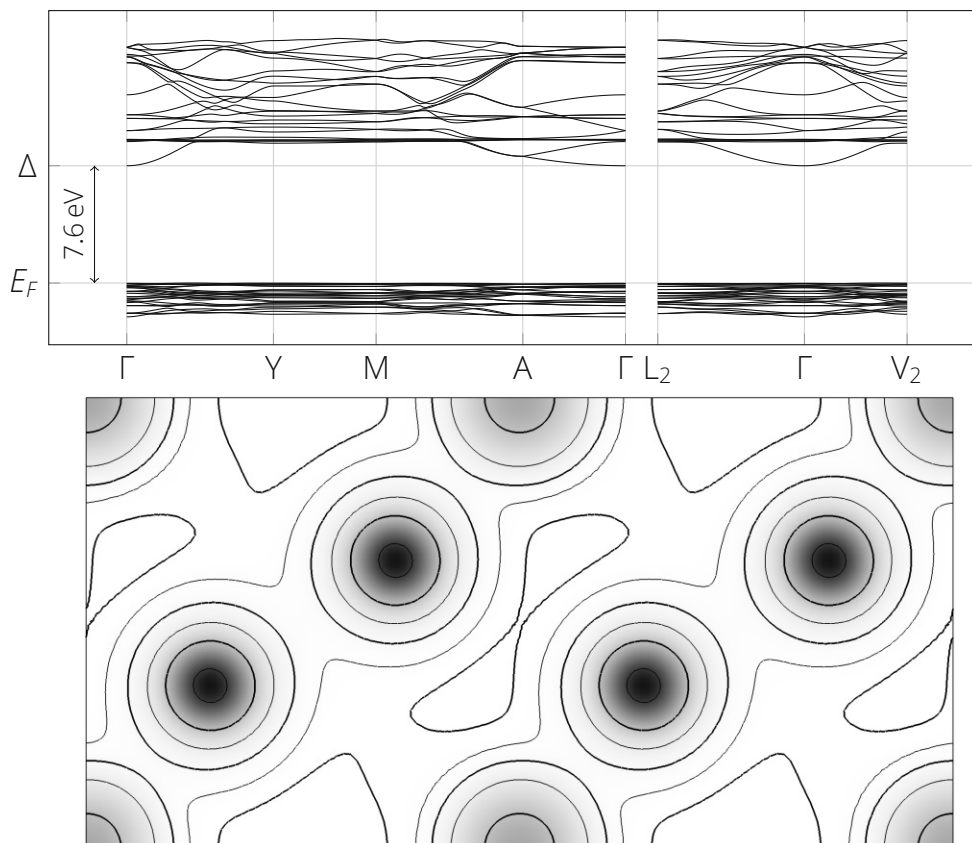
Figure 6.2: Top: The band structure of LICAF as computed with PBE is depicted. Even some of the valence bands exhibit localization as illustrated by their flatness. Bottom: Slice through the charge density in the (1$\bar{1}$1) plane with contour lines.

6.2 Thorium Doping

6.2.1 Determining Structures

LICAF is also a candidate as a host crystal for a Th nuclear clock.[104] Due to its complex structure, a quantum mechanical treatment for the impurity is as of yet outstanding. While for the simpler materials Th:CaF_2 and Th:MgF_2 possible compensation mechanisms could easily be guessed, this is now no longer the case. We tackle this problem by recursively constructing configurations which are effectively neutral in charge. For this the assumption is made that the oxidation states are +1, +2 and +3 for Li, Ca and Al respectively.[86,87]

Further, we assume that thorium either takes an interstitial position in the lattice, or it substitutes either cations Li, Ca or Al. In particular, it is not assumed that Th substitutes an F anion. Now, depending on the type of doping there is a charge imbalance of $+3, +2, +1$ for the replacement of Li, Ca and Al respectively or $+4$ in an interstitial scenario.

To account for this we allow each chemical species to be introduced to the system or to leave the cell. We define the impurity inside the crystal as a sphere with radius r_I containing all irregular atoms, be it interstitials, substitutionals or vacancies.

Because of periodic boundary conditions we aim to have relatively equal distances between each defect. As a compromise between computational speed and chemical accuracy, we choose a $2 \times 2 \times 1$ super-cell, with $c/a = 0.97$ and 72 atoms, which corresponds to a doping concentration of $\approx 1.4\,\%$.

Within this super cell we search for regions of empty space to accommodate possible interstitial atoms. In total, we find 76 potential positions, which together with the 24 vacancy locations results in an extremely large number of potential configurations. Thus we have to impose some restrictions: The maximum and minimum distance between two defect locations shall be $2r_I$ and $r_D < r_I$ respectively. Additionally, we consider 14 different stoichiometries ranging from 4 Li vacancies, to 4 F interstitials. To minimize sampling bias, we determine configurations with three different approaches for limitation:

1. Set the number of impurity atoms, set values for r_I and r_D, generate configurations, then change numbers for impurity atoms, r_I and r_D ("`number`").

2. Choose a charge compensation mechanism, then set r_I and r_D, generate configurations, then choose other mechanisms with different sets of r_I and r_D ("`choice`").

3. Same as 2. but measure r_I from Th only, thus making Th the center of the impurity ("`central`").
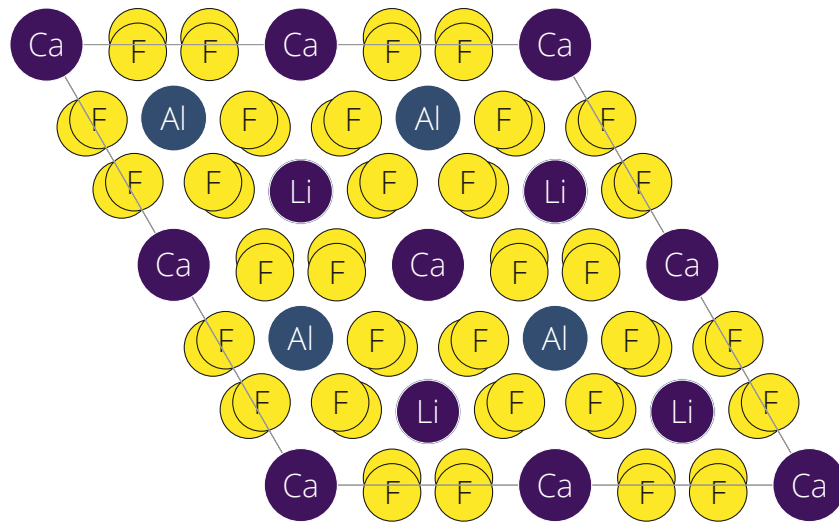
Figure 6.3: Visualization of the $2 \times 2 \times 1$ super structure. Notice the hexagonal arrangement of alternating Li and Al atoms with Ca in its center. In this perspective, behind each Al atom is a Li atom and vice versa. Note that in addition to Ca atoms at the corners and half points of the lattice vectors, there is a Ca atom at the center of the whole cell.

To clarify the difference of these datasets, we give an example in the following. Consider the possible charge compensating mechanism with $+1$ Th, -1 Al and -1 Li (which is neutral in charge because $+4 - 3 - 1 = 0$). Omitting the interstitial Th, which is always given, the number of impurity atoms is 2. For this count it is tantamount whether we create a vacancy or an interstitial atom. Now we define the maximum and minimum distances $2r_I$ and r_D between any two atomic impurity locations. Next we generate structures considering all possible charge compensation mechanisms where the number of impurity atoms is 2 and place atoms on the pre-defined interstitial positions, create vacancies or substitute cations while taking the overall symmetry into account. We call the generated configurations "`number`".

However, with this method it is not guaranteed whether all charge compensation mechanisms are contained in the dataset. It may very well be that the constraints of r_I and r_D are too strict for some stoichiometry to be generated. Thus we now create different sets of r_I and r_D such that each compensation pathway has at least several configurations created. For computational reasons we aim to keep this number below about 24 for each compensation pathway. We give these configurations the name "`choice`".

Since thorium is by far the most inert of all the LICAF constituents, we speculate that Th will be at the center of the impurity. So far this has not been re-

59

flected by our method since it would be possible that Th and another impurity atom are $2r_I$ apart. As such we change the meaning of r_I to be the maximum allowed distance of an impurity atom to the thorium position. Now we repeat the above mentioned procedure of choosing sets r_I and r_D for each compensation pathway. Note that the number of generated configurations shows a step-like behavior with respect to the distance parameters. We disregard compensating structures where this step is very high, i.e. much larger than 24. Also, we neglect configurations where $2r_I$ is a significant proportion of the LICAF cell. The generated configurations are named "`central`".

These datasets generate the following amounts of configurations: `number` contains 575, `choice` contains 396 and `central` contains 63, totaling at 1034. All structures are then relaxed with an accuracy of forces being smaller than $10^{-2}\,\mathrm{eV\,\AA^{-1}}$. In practice, this requires 25 to 425 ionic steps in the relaxation procedure per configuration (on average between 100 to 200).

Although this method reduces the number of combinatorial possibilities to a set of physically reasonable configurations, the remaining computational effort still presents the main constraint.

6.2.2 Obtaining Chemical Pathways

Outside of the crystal, the four elements Li, Ca, Al and F may form various different compounds. For this project, the challenge is to determine which combination of materials is the energetically most favorable.

A great number of compounds and corresponding energies can be found in the materials project database.[105] Determining chemical pathways for compensating atoms in this work is done by exhausting every possibility in a recursive search.

The fact that each compound may have different phases presents an additional difficulty. As an example, in Ca – F compounds we find a CaF structure, four CaF_2 phases, two CaF_3 phases and one Ca_2F structure in the materials project database. Naturally, the most favorable phase per stoichiometry is readily obtained by considering only the one with the lowest energy. Nonetheless, there is a question whether there are situations where one of the stoichiometries is preferred over the other. We aim to find an answer by choosing an ideal mixing ratio of the elements for the compounds, and then comparing its energy with that of the mixture.

As an example, we already know from previous knowledge that CaF_2 is the most stable phase. On the other hand, CaF may be created by $1/2CaF_2 + 1/2Ca$, however the latter is energetically preferred, hence CaF is disregarded. Generally, if a specific material is lower in energy than any combination of its building

blocks, we select it for consideration of Th:LICAF's charge compensation.

To determine chemical pathways, we assume that there is a type of bonding which is so strong, that it uses up all of the available atoms for one element. Then, this process is iterated with the elements left over until no atoms remain.

Although this method usually follows the energetic minimum, there are instances of co-existing phases, where the assumption is not enough to obtain the lowest energy. In this work, we find two examples of this peculiarity: $CaO + CaO_2 < Ca_2O_3$ as well as $4LiAl + Li_3Al_2 < Li_7Al_6$. The former case in particular can be problematic, because additionally $Ca_2O_3 < 2CaO + {}^1\!/_2 O_2$ and consequently we would have erroneously selected an unstable phase. In all other cases the predictions are, to our knowledge, correct within the computational limits.

By disregarding energetically unfavorable phases, the following remain:

- Singular compounds: solid Li, Ca, Al and molecular F_2.

- Binary compounds: AlF_3, Li_2Ca, CaF_2, LiF and $CaAl_2$, Ca_8Al_3, $Ca_{13}Al_{14}$ and LiAl, $LiAl_3$, Li_2Al, Li_3Al_2.

- Ternary compounds: $LiCa_2Al$, Li_3AlF_6 and $CaAlF_5$

- Quaternary compound: $LiCaAlF_6$.

6.2.3   DFT Results

Using preferred chemical paths per stoichiometry, we can compare energies of all calculations. The gap for lowest energy per stoichiometry is presented in Table 6.1 and in Figure 6.4.

It is interesting to note that out of all 14 stoichiometries, 2 with the lowest energy originated from the `number` dataset, 9 from `choice` and 3 from `central` datasets. Relative to the respective number of configurations 0.35 %, 2.27 % and 4.76 % of all calculations per `number`, `choice` and `central` turned out to be the lowest in energy. It seems that physical intuition helps in finding low-energy states, however the most favorable scheme originates from the `number` dataset.

6.2.4   AE-KS Wave Functions

Now that we have obtained the most probable configurations, we can also have a look at the possibility for electron-bridge processes. For this, a large value of the wave function at the nucleus position is a necessity.

| atom exchange | | | | |
in	out	E (eV)	Δ^+ (eV)	Path
	$-1Al - 1Li$	0.00	10.66	$2LICAF + {}^1/_3Li_3AlF_6 + {}^2/_3AlF_3$
	$-2Ca$	0.52	8.74	$2LICAF + 2CaF_2$
$+1F$	$-1Al$	0.67	11.08	$2LICAF + AlF_3$
$+2F$	$-1Ca$	0.78	10.06	$2LICAF + CaF_2$
$+1Li$	$-1Ca - 1Al$	2.19	8.93	$LICAF + 2CaAlF_5$
	$-4Li$	2.70	9.24	$2LICAF + 4LiF$
$+1F$	$-3Li$	2.89	9.63	$2LICAF + 3LiF$
$+1Ca$	$-2Al$	3.20	10.80	$LICAF + {}^1/_3Li_3AlF_6 + {}^8/_3AlF_3$
$+1F + 1Li$	$-2Ca$	3.38	9.19	$LICAF + CaAlF_5 + 2CaF_2+$
$+2F$	$-2Li$	3.70	10.53	$2LICAF + 2LiF$
$+3F$	$-1Li$	4.14	9.70	$2LICAF + LiF$
$+2F + 1Li$	$-1Al$	4.16	11.08	$LICAF + CaAlF_5 + AlF_3$
$+4F$		4.69	10.15	$2LICAF$
$+2Li$	$-2Al$	5.88	9.97	$2CaAlF_5 + 2AlF_3$

Table 6.1: Details for each stoichiometry in a chemical environment containing the $2 \times 2 \times 1$ LICAF structure, 4 F from the doping procedure, and an additional 2LICAF cells to compensate all generated stoichiometries. The first two columns denote the amount atom exchange for each compensation scheme, omitting Th. Next follows the relative energies and scaled band gap $\Delta^+ = \frac{12.65}{7.59}\Delta_{DFT}$ values. The rightmost column shows the energetically preferred chemical path for compensation outside of the crystal.
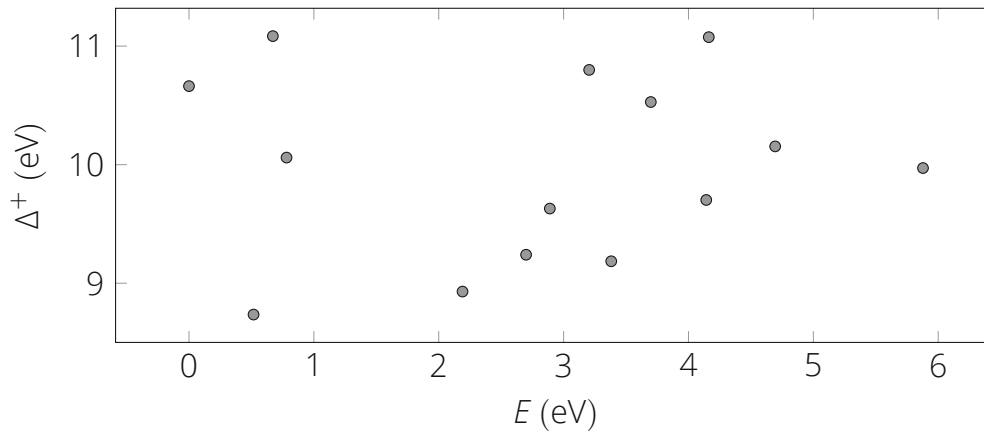
Figure 6.4: The energies of the best configurations per stoichiometry and scaled gap sizes are depicted. Neither show a trend, being spread out over the entire range. Gap sizes are in general relatively large, meaning that any of the proposed configurations could potentially be used as a nuclear clock.
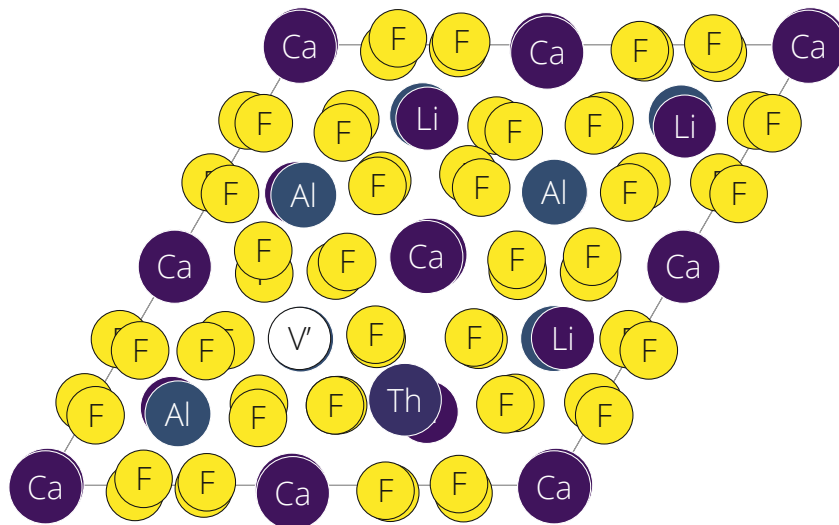

Figure 6.5: The energetically most favorable configuration with an Al and Li vacancy is depicted. After relaxation, the Th atom occupies the vacant Al position, while the Li vacancy, denoted by V', remains empty. Note that the initial position of Th was at an interstitial site, below the central Ca atom, i.e. directly in between the Al vacancy and the opposite Li site.

63

We investigate the energetically lowest configuration and identify valence band states lying directly above the band gap with localizations around the Th impurity, having dominantly f-character. In comparison to Th:CaF$_2$, there seem to be higher values of the wave function at the origin. We show the results in Table 6.2.
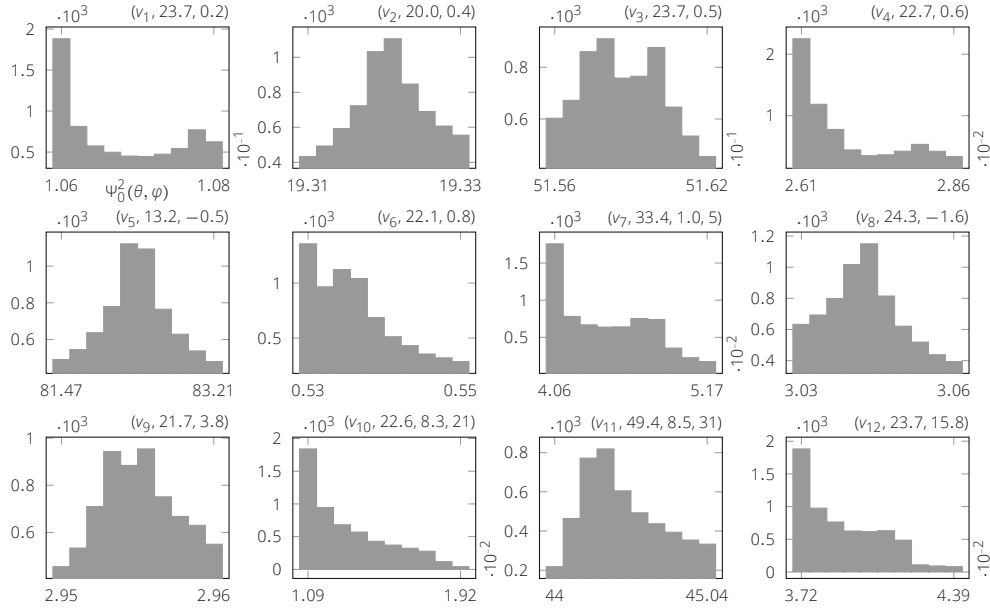
Figure 6.6: Numerical tests to estimate the uncertainty of the AE-KS reconstruction (Table 6.2) are shown. The figures are histograms for the wave function value at the origin Ψ_0^2 for the selected valence states on Th, where individual values are obtained from extrapolations along each (θ, φ) direction. Angular spacing is such that $\Delta\theta = \Delta\varphi = 3°$. Brackets on top of each plot are to be read as: (state label, uncertainty exponent n, $100 \times \Delta\Psi$). See subsection 5.2.3 for a definition of $\Delta\Psi$. For some states, the fourth number measures the percentage of extrapolations in (θ, φ) directions which do not coincide at the origin and are omitted in the histogram.

6.2.5 Neural Network Approach

Finding the most favorable configuration for a doped complex material such as LICAF requires a lot of computational resources, even when simplifying the problem and disregarding potential configurations. The tools of Machine Learning could in principle alleviate this issue to some degree. An accurate mapping of the structure to the energy with a neural network could speed up calculation
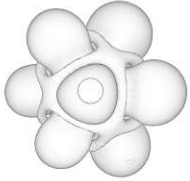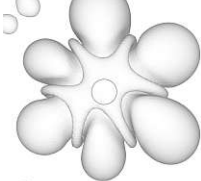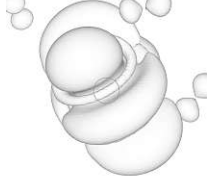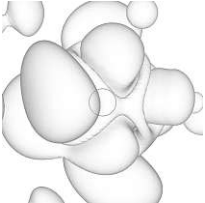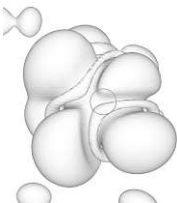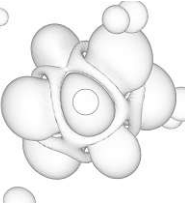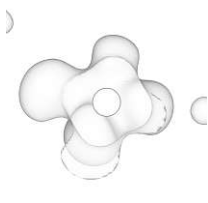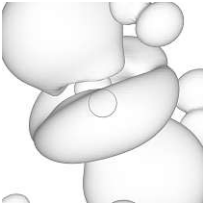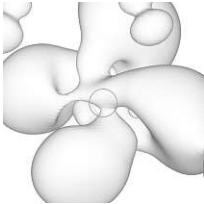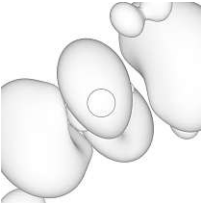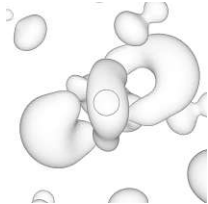
Band	v_1	v_2	v_3	v_4
E (eV)	5.887	6.006	6.157	6.220
Loc. (%)	98	96	96	96
$\rho(\mathbf{r})$				
Ψ_0^2 (Å^{-3})	0.11	19.32	5.16	0.03
Band	v_5	v_6	v_7	v_8
E (eV)	6.423	6.476	6.574	6.826
Loc. (%)	73	95	94	60
$\rho(\mathbf{r})$				
Ψ_0^2 (Å^{-3})	82.43	0.54	0.04	3.04
Band	v_9	v_{10}	v_{11}	v_{12}
E (eV)	7.356	7.759	8.072	8.118
Loc. (%)	69	49	42	13
$\rho(\mathbf{r})$				
Ψ_0^2 (Å^{-3})	2.96	0.01	49.42	0.93

Table 6.2: Energies, localizations, charge densities and the values of Ψ_0^2 of localized valence states for the most favorable Th:LICAF configuration are shown. In the charge density plots, Th is illustrated as having a black outline and surrounding p-states are in the same band but on F-positions.

time by a large amount, possibly making a more thorough search for suitable configurations and/or higher doping concentrations feasible.

In the following, we try to find the structure to energy mapping for Th:LICAF using the DFT data of the previous study. Considering each ionic step as a separate data point and removing high energy outliers, the dataset contains 196 833 configurations.
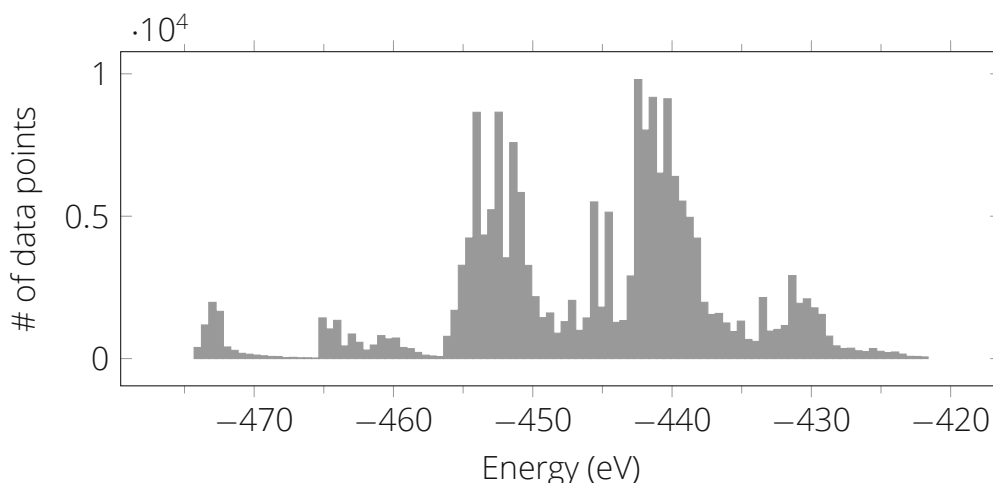
Figure 6.7: Energy distribution of all data points. Because the dataset has been generated using relaxations of different stoichiometries, the histogram is characterized by a distinctive peak structure. It must be noted that for the purposes of training a neural network, such peak structures are suboptimal and should rather be replaced by a more physically intuitive distribution, e.g. following Boltzmann-factors.

Atomic Fingerprint Calculation

The atomic fingerprints (AFPs) are calculated from the atomic coordinates, using the interatomic distances r_{ij}. In the crystal environment, these distances show an uneven distribution due to bond lengths and the resulting nearest neighbor shells, even though doping breaks the symmetry of the lattice. Arguably, this has an undesirable effect to the AFPs, which decreases the accuracy of the neural network. Of great importance is the parameter η as the width of the Gaussians:

- If η is large, the AFP values per atom tend to get very similar and consequently a structure to energy mapping is less obvious.

- If η is small, the AFP values per atom get spread out more, but tend to produce outliers, and/or produce a number very close to zero for a significant proportion of the dataset. Consequently, this may propagate an error through the neural network if not trained correctly.

Therefore, precise values for μ and η are essential to improve the training procedure. η should be as small as possible to accurately represent small deviations in the nearest-neighbor distances and the values for μ should be chosen accordingly. Because atoms can not get arbitrarily close, it is straightforward that central AFPs ($\mu = 0$) would require a very large η to give non-zero entries and are thus discarded entirely. From Figure 6.8 it is evident that η and μ need to be different for each chemical species in order to obtain AFPs which are mostly non-zero and spread out. Best results are obtained when μ is at peaks in the distribution for interatomic distances. For the cations Li, Ca, Al and Th, the nearest neighbor distances have a definite peak structure thus μ is readily obtained. Since the anions F are more spread out, the distances vary accordingly, making it more difficult to find suitable values for μ and η.

For cations Li, Ca, Al and Th we only probe the space around the nearest neighbor peak. We use four different μ around the peak: The first one has its maximum at the closest cation-anion distance and a relatively large width. The other three are located at the maximum value of the nearest neighbor peak and in between the "start" and "end" of it. The width of these Gaussians is chosen such that there is a small overlap over the whole range. Their purpose is to roughly sort distances into categories ranging from "near" to "far".

The distances of F atoms not only contain cation-anion distances but also F – F distances. Due to the ionic bonding, there should be a repulsive force which we also desire to capture. Cation-anion distances are roughly mapped with three AFPs: One which is sensitive to the closest distances with a large width and then two more to indicate Al/Li or Ca/Th bonding respectively. We then use 6 more Gaussians with varying width to scan the rest of the interatomic distances up to the cutoff radius. A visualization of radial AFPs with regards to interatomic distances can be found in Figure 6.8.

In the crystal environment, cation-anion pairs are found to exhibit octahedral structure, which means that interatomic angles are also not evenly distributed. We try to sort commonly found angles with angular AFPs including a phase shift and large values for ζ to increase their localization. We do not aim to accurately sort for interatomic distances in the angular AFPs, thus we set $\mu = \eta = 0$, making the cutoff function the only property which is influenced by the distance. The distribution of the angles as well as the angular AFPs are found in Figure 6.9.

The cutoff for both radial and angular AFPs for all cations is set to the end
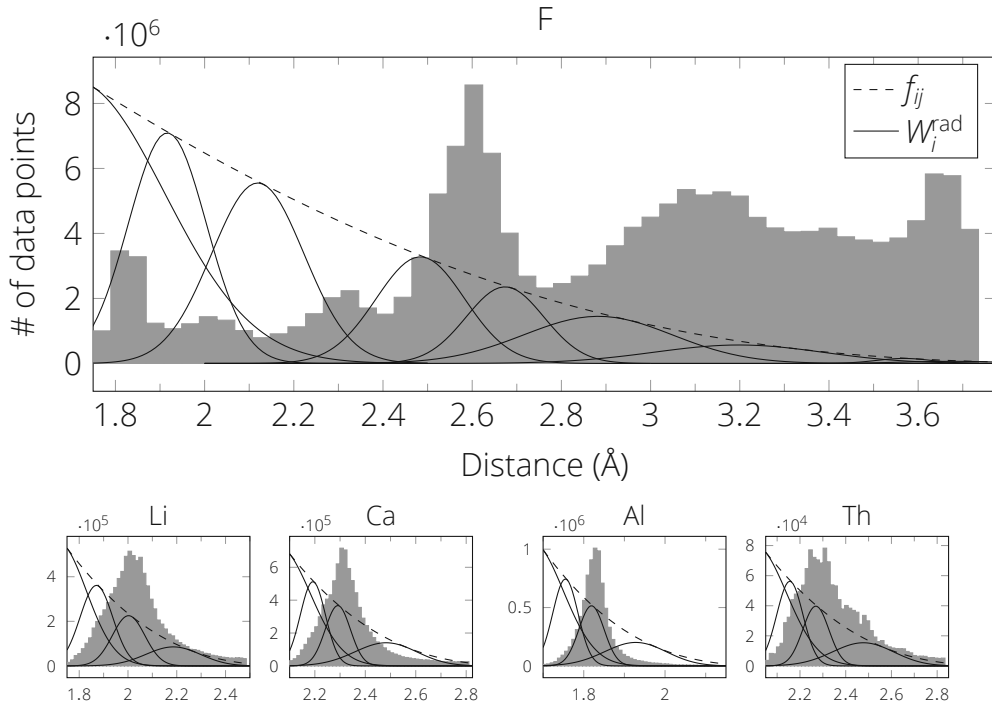
Figure 6.8: Histograms with neighbor distances r_{ij} per element in the dataset and the Gaussian AFPs with final parameters. Contrary to the anion F, histograms for the cations Li, Ca, Al and Th show a relatively well defined nearest neighbor distances peak.
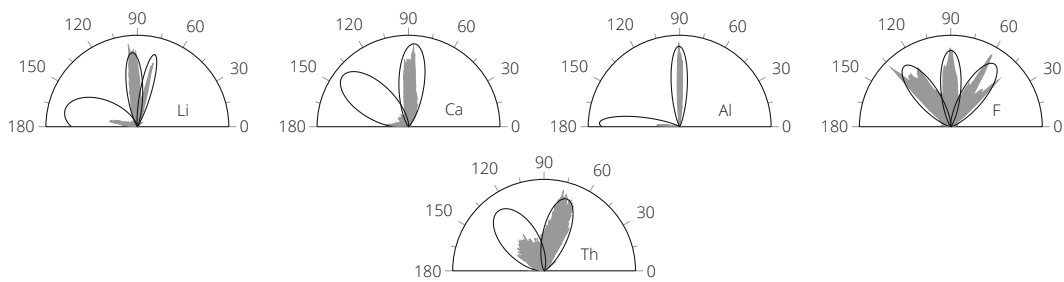
Figure 6.9: Histograms of angles for each element within r_C. Black lines are W_i^{ang} with different ζ and φ.

of the nearest neighbor shell, which is in units of Å 2.75, 3.10, 2.10 and 3.15 for Li, Ca, Al and Th respectively. For F, we use the maximum cation cutoff of 3.15 for angular AFPs to sort for angles to the cations only, while the radial AFPs use a larger cutoff of 4.15 to allow F-F probing.

Although we have attempted to make AFPs distinguishable to the neural network by flattening peak-like structures in their histograms, it was not always possible. The distribution of values for the AFPs for each element over 20000 random configurations are visualized in Figure 6.10–Figure 6.14.
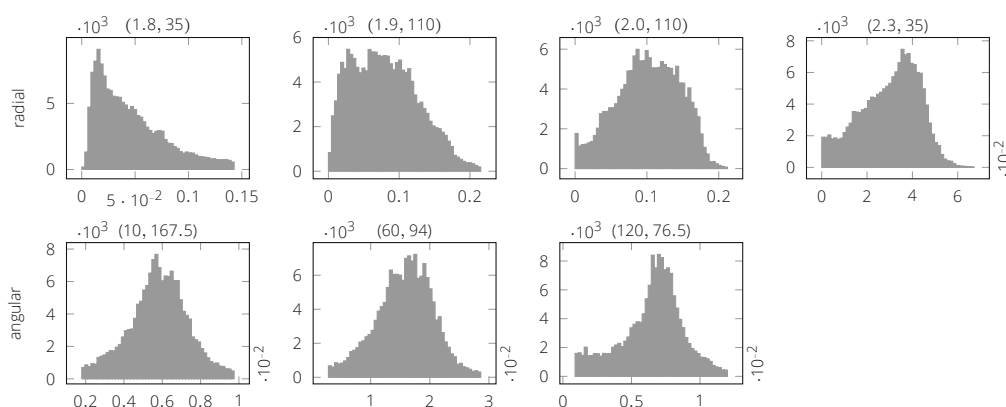
Figure 6.10: Distribution of AFPs for Li. Radial and angular AFPs are separated by rows and denoted by the label to the left. On top of each plot is a pair of parameters (μ, η) for radial AFPs and (ζ, φ) for angular AFPs.
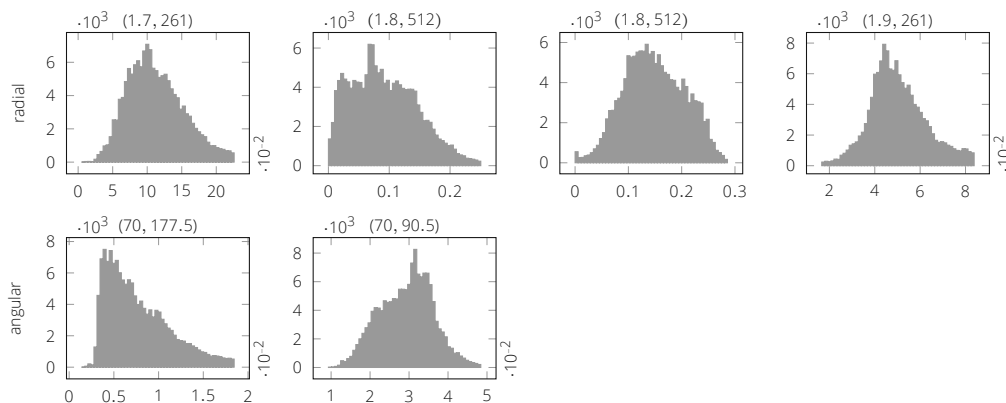
Figure 6.11: Distribution of AFPs for Ca. See caption of Figure 6.10 for reading instructions.
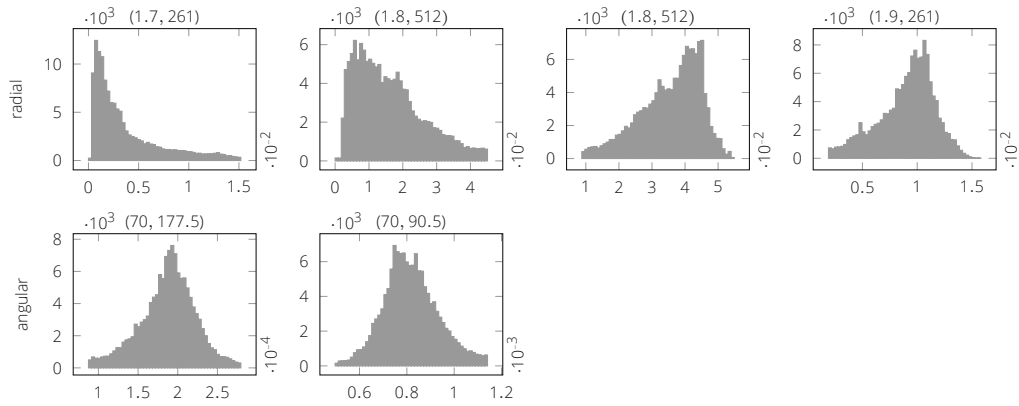
Figure 6.12: Distribution of AFPs for Al. See caption of Figure 6.10 for reading instructions.
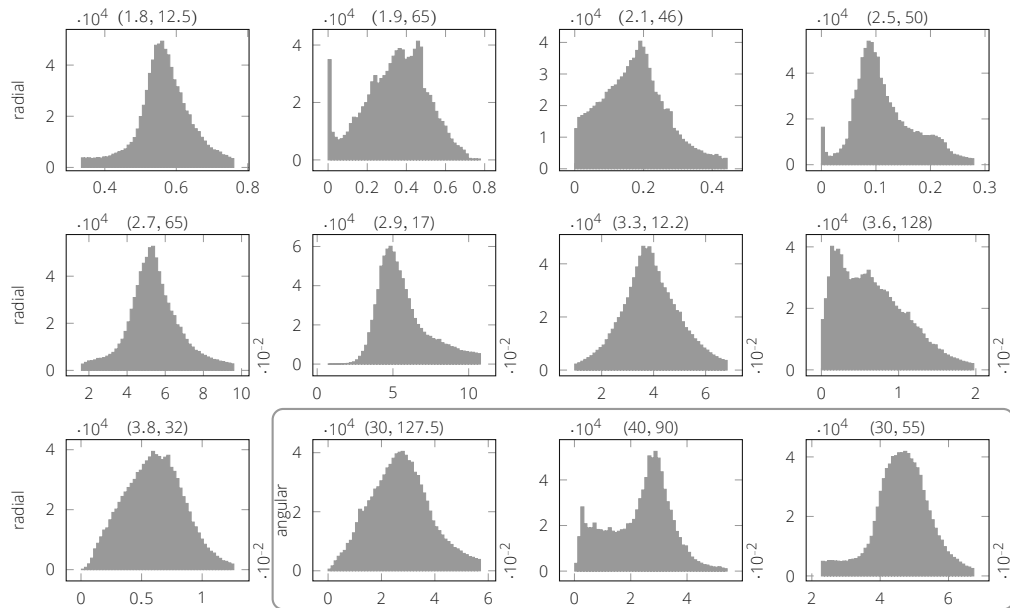
Figure 6.13: Distribution of AFPs for F. See caption of Figure 6.10 for reading instructions. Angular AFPs are found in the gray box.

radial

·10³ (1.7, 261)   ·10³ (1.8, 512)   ·10³ (1.8, 512)   ·10³ (1.9, 261)

angular

·10³ (70, 177.5)   ·10³ (70, 90.5)
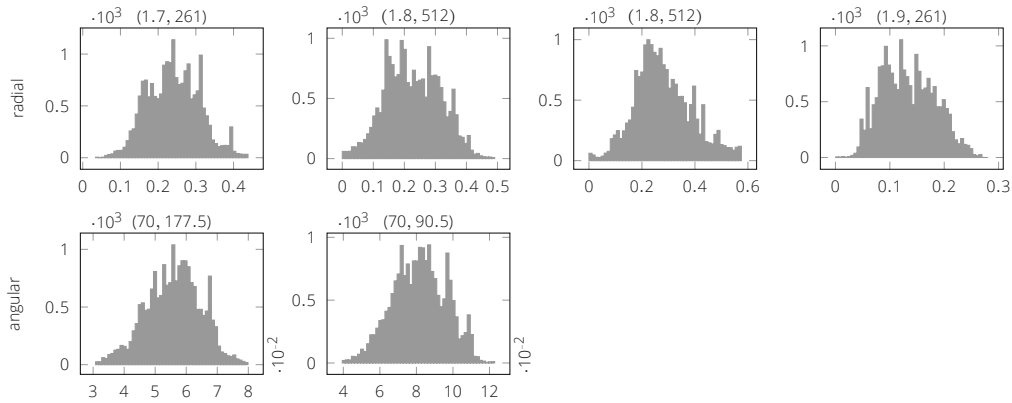
Figure 6.14: Distribution of AFPs for Th. See caption of Figure 6.10 for reading instructions.

Training

With these AFPs we train a neural network on the data using PyTorch.[106] We choose the size of the hidden layers such that for each of the five elements, its neural network has a number of parameters equal to $\frac{N_{\text{Samples}}}{N_{\text{Element}}} \frac{1}{\alpha(N_i + N_o)}$, where i and o denote "input" and "output".[107] We find best results for $\alpha = 2$. The number of hidden layers is chosen such that the maximum dimension is not many times larger than N_i, while keeping the number of hidden layers to a minimum.

	In	Hidden				
F	12	22	33	42	32	22
Li	7	12	17	21	16	11
Ca	6	12	17	23	18	12
Al	6	12	17	23	18	12
Th	6	10	8			

Table 6.3: Neural Network layers and their sizes. The input dimension is determined by the number of AFPs. Each element has a single output neuron representing the elements contribution to the total energy. Best results were obtained by using the SELU activation function.[108]

For the training procedure we separate the dataset into a training set with size $0.9 N_{\text{Samples}}$ which we validate on a validation set sized $0.05 N_{\text{Samples}}$ after each epoch and when training on these two datasets cannot be improved we validate again on the test set $0.05 N_{\text{Samples}}$. Remarkably, we find that the min-

imum error has a time dependence similar to $e^{e^{-kt}c_1+c_2}$, where t is the epoch number and k, c_1, c_2 are fit constants. We can thus estimate the final error in the limit $t \to \infty$, which is $\Delta E_\infty = e^{c_2}$. Results are shown in Figure 6.15, where we find $\Delta E_\infty = 2.9$ meV.
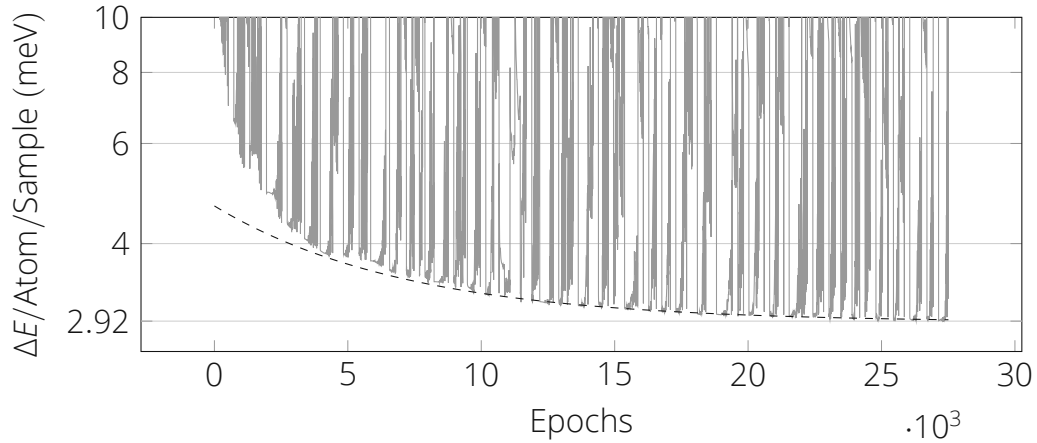
Figure 6.15: Average errors per epoch with minimum value 2.92 meV and an estimated final error of $\Delta E_\infty = 2.91$ meV. Only the last half of the data was used to arrive at ΔE_∞. Note the logarithmic y-axis.
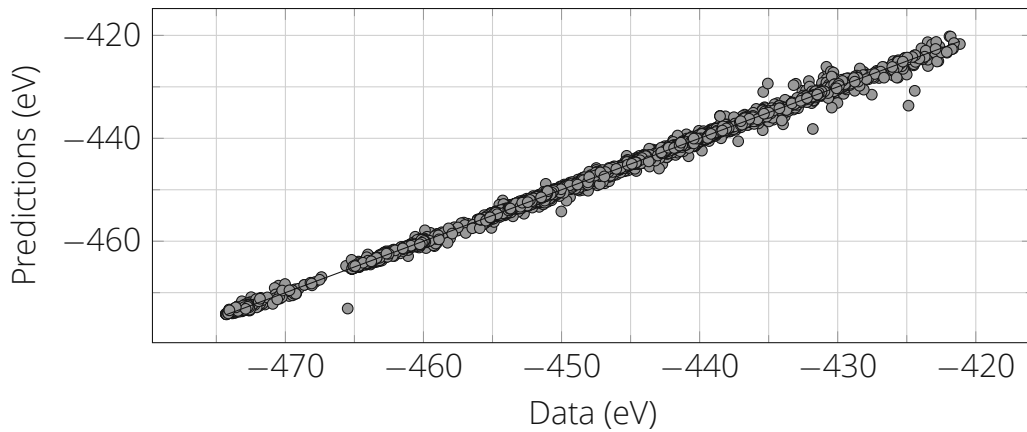
Figure 6.16: Energy values for configurations in the test set on the x-axis and predictions of the neural network on the y-axis. Superimposed is the main diagonal line.

Qualitative comparison of DFT and ANN

Now that the neural network has learned the energy mapping in our dataset, we aim to find out whether it could potentially determine favorable stoichiometries or even configurations.

To this end, we compare two approaches on the trained data. First, we let the neural network predict energies for the energetically lowest configuration in each stoichiometry in the dataset and compare these predictions with the actual DFT energies (i.e. the result of Table 6.1), where we calculate the mean absolute error (MAE) to be 0.2 eV. Second, we look at the reverse case, where we find minimum prediction energies per stoichiometry and compare these with DFT energies and find a MAE of 0.5 eV. The respective numerical values per stoichiometry are shown in Table 6.4 and a visualization of this data can be found in Figure 6.17.

In the first case, the error is small enough to allow the neural network to accurately predict the energetic ordering of the first few favorable stoichiometries, up to an energy of 2.7 eV. However, the magnitude of the error is far larger than what the convergence criterion for forces allows in a single relaxation run.

In the second case, even though the MAE is larger, the ordering is again correct, this time to about 2.9 eV. Note that the ANN did not predict the final relaxed configuration as having the lowest energy. This is because the energetic deviations between relaxation steps may be many orders of magnitude smaller than the average error of the test set (2.9 meV/atom).
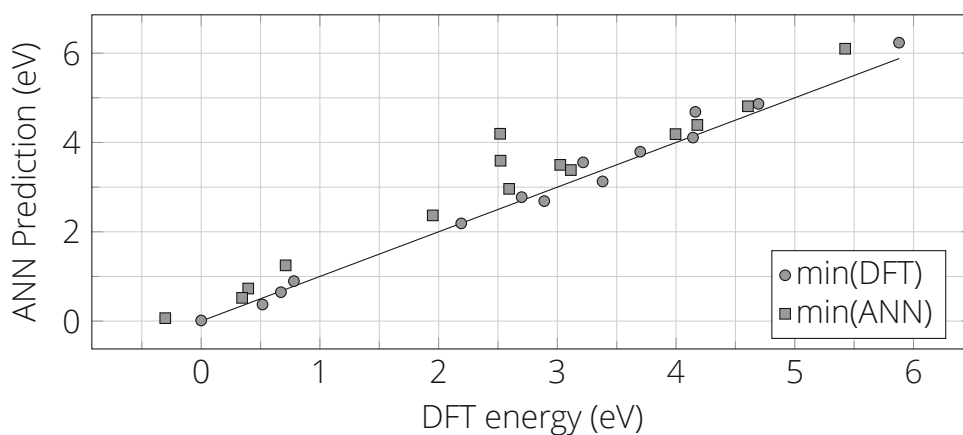
Figure 6.17: DFT energies versus ANN predictions from Table 6.4. Circles correspond to the minimum energy for each stoichiometry with DFT calculations, as shown in Figure 6.4, while squares denote the ANN prediction counterpart.

73

| DFT Energy (eV) | | ANN Energy (eV) | |
min(DFT)	min(ANN)	min(DFT)	min(ANN)
0.000	0.066	0.015	−0.303
0.517	0.521	0.371	0.345
0.672	0.730	0.647	0.396
0.781	1.249	0.895	0.711
2.191	2.367	2.188	1.951
2.700	2.962	2.776	2.594
2.890	3.592	2.687	2.522
3.217	3.499	3.555	3.024
3.381	3.383	3.128	3.114
3.698	4.195	3.792	2.518
4.142	4.187	4.109	3.995
4.163	4.392	4.686	4.179
4.694	4.811	4.864	4.606
5.878	6.099	6.235	5.424

Table 6.4: Comparison of predictions for the total energy of DFT and the ANN. In the first column is the DFT result as seen in Table 6.1, while in the second column are DFT energies for the ANN predicted most favorable configurations per stoichiometry. In the third column are ANN predicted energies for the result in Table 6.1 and finally in the fourth column are the ANN energies of its own predicted favorable configurations per stoichiometry.

Chapter 7

Conclusion

In this work we present various DFT results obtained with VASP of the doped large gap insulators MgF_2, CaF_2 and LICAF. Mainly we investigate thorium doping due to its proposed application as a nuclear clock. The three materials each have different structural properties, with MgF_2 showing a tetragonal lattice, CaF_2 a fcc-lattice and finally LICAF presents a major increase in structural complexity with its trigonal lattice.

Thorium has a different oxidation state than all the constituents of the investigated materials. Therefore the dopant is accompanied by charge compensating atoms, which we determine by studying the energy contributions of the impurity and the chemical environment outside of the doped crystal.

Th:MgF_2 and Th:CaF_2 were studied previously albeit with different computational parameters.[80,81,88] In several aspects, we increase the computational accuracy compared to these previous studies and confirm their qualitative results. Although Mg and Ca are in the same group in the periodic table, their different structures in fluoride crystals also favor different compensation mechanisms: A cation Mg vacancy in Th:MgF_2 and two interstitial F anions in Th:CaF_2. Substitutional thorium doping for the cations in both cases is energetically preferred. While the band gap of Th:MgF_2 is considerably reduced, the favorable configuration of Th:CaF_2 shows the largest band gap of all investigated compensation mechanisms.

Further, we determine the possibility that surplus fluorine atoms, originating from the doping procedure, create another defect in CaF_2 instead of leaving the crystal to be in the molecular F_2 arrangement. Our simulations indicate that it is favorable for any surplus fluorines to form groups of three around a central Ca atom. The energy penalty when compared to the gas phase is 0.4 eV/atom of fluorine, which corresponds to a Boltzmann factor at the crystallization point of 94.3 %. However, we do not estimate the band gap to reduce notably in this defect configuration.

75

Also we estimate the impact of lattice vibrations at finite temperature on the optical properties of Th:CaF$_2$ by assigning a score to each mode based on the vibrational displacements with respect to the thorium position and the interatomic distance. We identify several modes at around 9.8 THz and 10.1 THz, which we assume to have the greatest impact. Cooling the sample to 30 K should eliminate virtually all occupation of these modes.

An experimental verification that ^{229}Th is in its excited state may be done with nuclear quadrupole resonance spectroscopy. To aid in the calibration of the measurement devices, we calculate the electric field gradient of actinium, cerium and neptunium doped CaF$_2$. Again, we perform a charge compensation analysis and find that interstitial placements of one, two and three fluorines are energetically preferred respectively. When comparing the relaxed impurity structures for all dopants, we find that interstitial fluorines tend to form an angle of about 70° with the cation (except Ac:CaF$_2$, which has only one interstitial fluorine) and an approximate distance to the dopant of 2.2 Å.

Because of the above mentioned complexity of LICAF, a computational charge compensation analysis has not been published before this work. We develop a systematic approach concerning both the possible charge compensation placements and also the stoichiometries outside of the doped crystal. To achieve a convincing analysis, we calculate a sizable number of compensation schemes find that the favored compensation mechanism does not feature interstitial atom placements. Instead, thorium substitutes an Al in the vicinity of a Li vacancy. Band gap sizes for all compensation schemes range between 9 eV to 11 eV, with the systematic underestimation of DFT being considered via the scissors-operator.

Inspired by recent developments in the field of machine learning and its promising capabilities in computational materials science, we use the calculated configurations of LICAF to train a neural network on the structure to energy mapping, where we modify the atom centered symmetry functions as devised by Behler.[19] If the predictions are accurate enough it would greatly aid in the search for new promising charge compensation configurations and/or enable an increase of the doping concentration. Our best network was able to predict energies with an average error of 2.9 meV/atom, which is far smaller than the total energetic deviation in the dataset. Thus, the network would be able to categorize the configuration's energetic region, but it would be unable to identify whether a configuration is fully relaxed.

Since the ^{229}Th isomer transition is very close to the band gap energies in doped CaF$_2$ and LICAF, an electron bridge mechanism could transfer the energy of an excited electron to the thorium nucleus. In collaboration with the Max-Planck Institut für Kernphysik in Heidelberg we obtain transition rates for

this scheme in Th:CaF$_2$. The rates are calculated by using wave functions of the impurity and conduction band states obtained in this work. Because VASP uses the PAW-method and an accurate wave function in the core region is required, we calculate the all-electron Kohn-Sham (AE-KS) states from the pseudo wave functions. The results for Th:CaF$_2$ were published elsewhere and we also present the AE-KS states for the most probable configuration in Th:LICAF, where the impurity states show promising estimates for the wave function values at the nucleus but a conclusive investigation on electron-bridge rates has not yet been attempted.

In general, the quality of the results in the present work depends on the inherent properties of DFT: On the one hand, its efficiency allows us to perform relaxation of impurities with realistic doping concentrations or negligible long range interactions. On the other hand, we are mainly interested in the band gap, which DFT systematically underestimates. In particular, DFT can only perform calculations on the ground state; any true description of excitation effects is therefore out of the scope of this work. Additionally, the approximations in DFT are best suited for systems with low correlations. Insulating crystals do not fall into this category per se, however since the band gap is large and the form of the band structure does not change with SCAN or HSE approaches as compared to PBE, it is our assumption that systematic DFT errors are not an exceedingly serious concern for our purposes. In any case, it would be highly interesting to compare the results with other many body methods. Often such methods start from DFT relaxed ionic positions, as such this work provides the foundation for further research.

It is important to note that our charge compensation analysis may depend on the choice of the overall chemical environment, which we decide on by imagining doping via ThF$_4$ and additional unit cells of the host crystals as required to realize all charge compensation schemes. We include an analysis for oxygen impurities in Th:CaF$_2$ and Th:MgF$_2$ and conclude that it is unlikely for oxygen to take part in the impurity. However, should the sample be contaminated, e.g. exclusively with cations, the resulting chemical paths could tilt the energy balance in favor of other charge compensation mechanisms. To gain more confidence in our predictions, further research could be done by studying different chemical environments considering the actual crystallization procedure and comparing the results.

Also, the treatment of heavy elements makes relativistic effects more prominent, especially in the regions around the nuclei. By default VASP performs scalar relativistic calculations[109] but spin-orbit coupling has to be enabled by the user. Our main motivation was to calculate AE-KS wave functions, a feature that VASP does not supply. However we could not converge our structure using

other open source DFT packages and consequently we modified VASPs source code in order to extract the necessary projector functions. Our modification is not yet able to operate when spinors are calculated as is the case when considering spin-orbit coupling. Fixing this matter would enable a full relativistic calculation, which may give a more accurate estimation on electron-bridge transition rates. At least for the prediction of the electric field gradient on U:CaF$_2$, VASP results were not significantly altered by the inclusion of spin-orbit coupling.[98]

Finally, we conclude the application of artificial neural networks on our LICAF dataset with an ambiguous assessment. While we were able to minimize the mean average error by carefully choosing the atomic fingerprint parameters, the overall inaccuracy is still too large for determining highly favorable configurations with enough certainty. We want to point out that the dataset was not meant to be solely responsible for training the network, because first and foremost we determined the charge compensation mechanism of Th:LICAF. Therefore, a further improvement on the accuracy may be achieved by exploiting current knowledge about favorable stoichiometries and calculate structures closer to the ground state, possibly using Boltzmann-factors to choose new configurations and increase the overall quality of the input data. However, even with this dataset it may be conceivable to decide whether a generated configuration is not a likely candidate for a low energy structure; the neural network would then act as a binary classifier. In this sense, it could aid the search for reasonable configurations with the additional need to perform a DFT relaxation on them.

Part III

Appendix

A Convergence Studies and Total Energies

A.1 Introduction

The following sections contain a multitude of Figures and Tables concerning the convergence and experimental comparison of various compounds using the pseudopotentials of the respective elements. We perform several types of convergence studies:

1. Energy cutoff convergence: We calculate a reference energy with a cutoff far larger than what was used in the generation of the pseudopotential, i.e. `ENCUT` $\gg$ `ENMAX`. We then vary the cutoff and compute $\Delta_{\text{ref}}E = |E_{\text{ref}} - E_{\texttt{ENCUT}}|/N$, where N is the number of atoms in the cell. In the Figure axis labels, the index "ref" is replaced by the reference cutoff. We deem the cutoff as converged when $\Delta_{\text{ref}}E < 10\,\text{meV}$, which usually results in a value slightly larger than `ENMAX`.

2. **k**-mesh cutoff convergence (only for solid phases): In the same way as previously, we perform a reference calculation with a large grid size in reciprocal space and compute $\Delta_{\text{ref}}E$. The number of **k**-grid points in each direction is adjusted according to the relative size of the lattice vectors. A converged grid size has the same criteria as previously, i.e. $\Delta_{\text{ref}}E < 10\,\text{meV}$.

3. Equilibrium lattice constant determination (only for solid phases): For cubic lattices, we plot points of energy per atom over a volume scaling factor s. We choose the points for s in the following fashion: After the first three s points are calculated, the next calculation proceeds half way between the two s-points with the lowest energy. This process is iterated until the difference in energy between both points has reached a threshold (usually 10 meV but sometimes lower). We then interpolate these points with a Morse fit

$$E(s; s_0, D, a) = D\Big(1 - e^{-a(s-s_0)}\Big)^2, \qquad (7.1)$$

where the DFT equilibrium volume scaling factor s_0, the depth of the potential well D and the steepness of the slope a are the fit parameters. It is then possible to calculate the bulk modulus

$$B = V \left.\frac{\partial^2 E}{\partial V^2}\right|_{V=V_0} = 2Da^2V_0, \qquad (7.2)$$

which can be compared to the experiment via measured elastic constants $B = {}^1\!/\!3(C_{11} + 2C_{12})$.[110]

For lattices where $\mathbf{a} = \mathbf{b} \neq \mathbf{c}$, we have two scaling factors: One scales the c/a ratio while the other scales the volume as previously. The above mentioned routine is then performed for each scaling factor in a double loop. The convergence threshold is usually reduced to 1 meV. Next, for each fixed c/a we interpolate the volume scaling data points with a Morse potential and interpolate the fit parameters s_0, D and a of each c/a ratio with a quadratic spline. We then plot these results as a contour plot together with the energetic minimum.

4. Distance convergence (only for gaseous compounds): Since VASP uses periodic boundary conditions, we must calculate non-periodic systems by using a large unit cell with enough vacuum in between such that interactions are negligible. Therefore we must converge on the vacuum distance. To do this we again calculate a reference energy for a large distance and vary distances smaller than the reference to compute $\Delta_{\mathrm{ref}}E$. The convergence criteria is $\Delta_{\mathrm{ref}}E < 10$ meV. A further option is to interpolate on the calculated data points with the function

$$E(d; a, b, E_0) = 10^{-ad}b + E_0, \qquad (7.3)$$

where d is the length of periodicity and a, b and E_0 are fit parameters. In the limit $d \to \infty$, E_0 is the final energy. This is especially useful when it is hard to converge on the distance e.g. because the compound is ionized hence the interactions are long range.

Apart from convergence studies, we have a few additional remarks about notation:

- After convergence tests have been thoroughly performed we often seek an experimental comparison, which we denote as $\Delta_{expt}O = O_{\mathrm{VASP}} - O_{\mathrm{expt}}$, where O is an observable quantity.

- We denote the total free energy of our calculations with E^0. This is the value as stated in the last line of VASP's `OSZICAR` file, which we often reduce accordingly to represent a certain number of atoms.

- Usually we denote a pseudopotential by its `TITEL` flag but there are exceptions when we want to emphasize certain properties thereof. As an example Ca_{sv}^{267} denotes the `sv` type of the Ca pseudopotential which has a value `ENMAX` $= 267$.

A.2 Compensating Thorium Doped Magnesium Fluoride

Magnesium

In its metallic allotrope Magnesium forms a hexagonal close packed (hcp) lattice.[111] However, we find a discrepancy in the materials project database,[105] where the cubic fcc lattice (ID 1056702) is energetically preferred and labeled as stable, although it is noted that a high-pressure phase is considered.

We aim to find out whether this error stems from DFT by calculating the energy for both the hexagonal and the cubic lattice. Indeed, our calculations show that the hcp lattice is energetically preferred. It was also not possible to reproduce the final energy from the VASP input files of the materials project database.

			Pseudopotential		
			GW	pv_GW	sv_GW
PBE	E (eV)	fcc	−1.491	−1.488	−15.638
		hcp	−1.520	−1.515	−15.665
SCAN	E (eV)	fcc	−4.939	−4.967	−19.113
		hcp	−4.976	−4.996	−19.150

Table 7.1: Energy per atom for different pseudopotentials and crystal structures with different levels of DFT.

Fluorine

For the highly reactive Fluorine, VASP supplies seven pseudopotentials. A rough categorization may be done to separate two approaches: the PBE generation of the pseudopotential with types *default*, here also called `std`, `s` and `h`, as well as the GW generation with types `GW`, `GW_new`, `d_GW` and `h_GW`.

First, we determine the electron affinity with gaseous Fluorine. To further test the pseudopotentials, accuracy of forces are investigated for molecular Fluorine F_2. All studies were done with the PBE XC-functional except otherwise stated.

At standard conditions, Fluorine is a diatomic gas F_2 with a bond length of 1.4119 Å.[112] We also test the pseudopotentials on the molecular bond dissociation energy of $\Delta H = 158.670(96)$ kJ mol^{-1}.[113]

Following the convergence studies in Figure 7.2 and Figure 7.3 we determine the total energies for both the neutral and ionized states and calculate
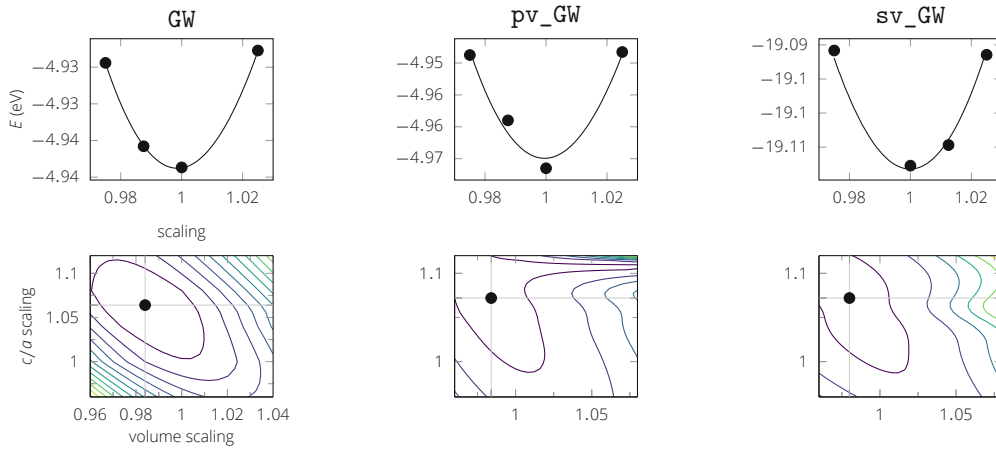
Figure 7.1: Final volume convergence tests for fcc (top) and hcp (bottom) Mg for different pseudopotentials `GW` (left), `pv_GW` (middle, the spike in contour lines is an interpolation artifact) and `sv_GW` (right). Convergence tests of the energy cutoff and k-points are not shown for the sake of brevity.

the electron affinities (see Table 7.2).

PP	E^0 (eV)	E^- (eV)	$\Delta_{\mathrm{expt}} E_{\mathrm{ea}}$ (eV)
std	−0.51	−5.06	1.16
s	−0.50	−5.05	1.15
h	−0.43	−4.96	1.13
GW	−0.43	−4.96	1.13
GW_new	−0.42	−4.97	1.15
d_GW	−0.42	−4.97	1.15
h_GW	−0.43	−4.99	1.16

Table 7.2: The results of the convergence studies are summarized. From left to right: pseudopotential type, converged total energy for the neutral atom, converged total energy for the anion, difference of the electron affinity as calculated with DFT to the experimental reference value of $E_{\mathrm{ea}} = 3.401\,189\,7(24)$ eV.[114] The calculated electron affinity has a mean systematic error of 1.15 eV. Between the pseudopotentials the differences are small compared to the systematic deviation. For the `h_GW` pseudopotential we also performed an HSE calculation and find $\Delta_{\mathrm{expt}} = 0.85$ eV.
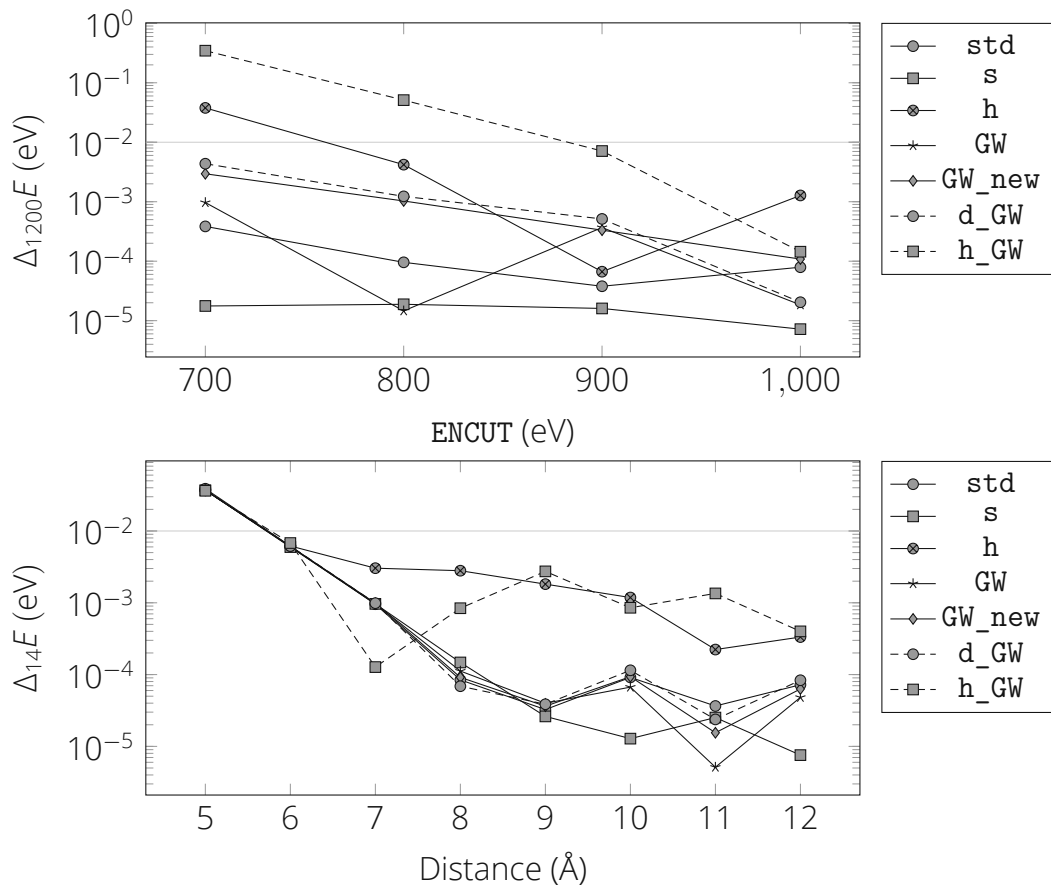
Figure 7.2: Top: Energy cutoff convergence study for gaseous Fluorine with the available pseudopotentials. The different types show great variability in convergence. Bottom: Vacuum convergence studies for all pseudopotentials. The greater variability of the hard pseudopotentials can be seen starting from 7 Å

84
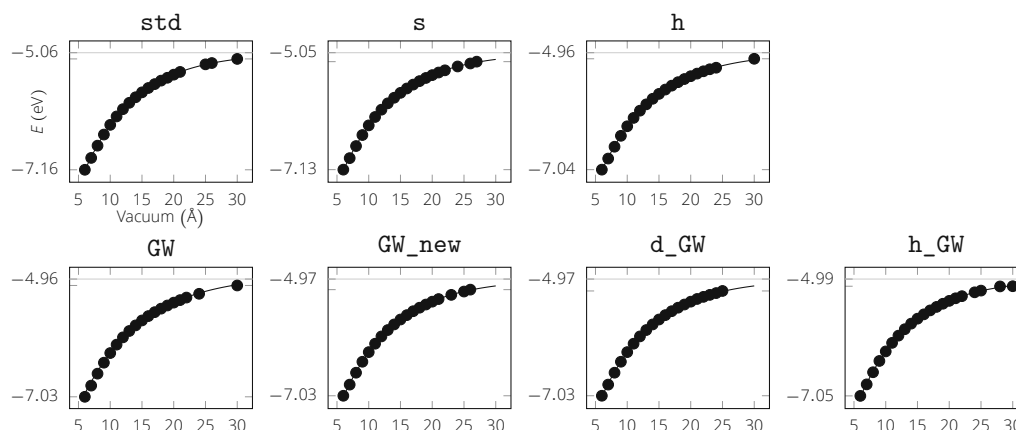
Figure 7.3: Convergence of vacuum size for every pseudopotential in the atomic F$^-$ state, where the dots represent individual calculation results and the solid line is an interpolation function.

PP	E^0 (eV)	$\Delta_{\text{expt}}d$ (Å)	$\Delta_{\text{expt}}dH$ (eV)
std	−3.782	−0.011	0.220
d_GW	−3.675	−0.003	0.192
GW	−3.650	−0.008	0.208
GW_new	−3.683	−0.002	0.187
h	−3.693	−0.002	0.185
h_GW	−3.695	−0.001	0.186
s	−3.649	−0.039	0.285
GW	−6.935	−0.009	
GW_new	−6.931	−0.009	

Table 7.3: Total energy E^0 and difference of bond length and bond dissociation energy when compared to the experiment. Calculations were done with PBE except for the last two rows, which were done with SCAN.
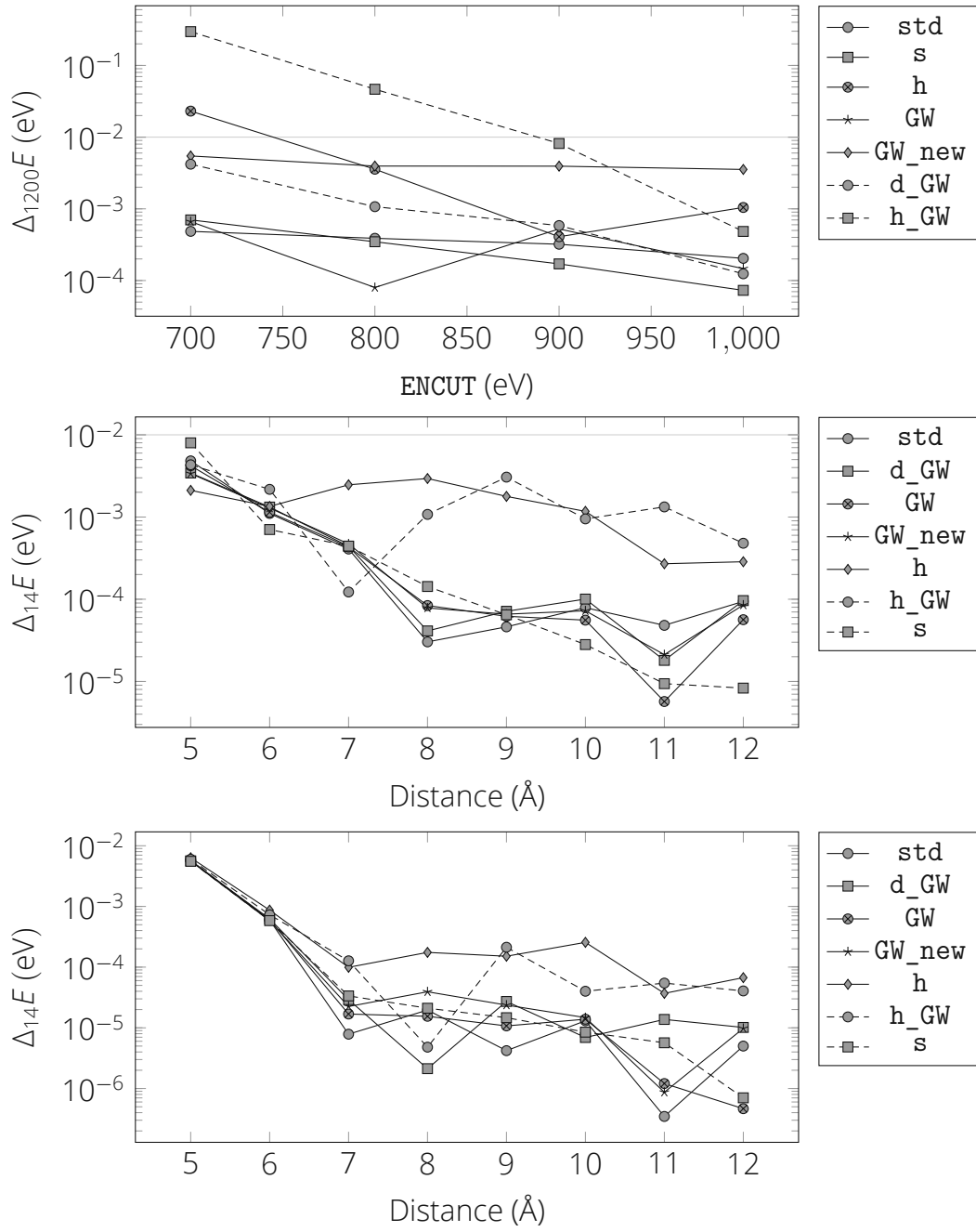
Figure 7.4: Convergence studies on F_2 for energy cutoff (top) and molecular distance on energy and bond length (middle, bottom).

Oxygen

Molecular oxygen is a diatomic molecule at standard conditions. It has an observed bond length of 1.207 Å and we find an enthalpy of formation of 249.18(10) kJ mol^{-1}.[79,115] One of its exceptional properties is the triplet ground state. We compare our calculated values to the experiment an obtain total energies as shown in Figure 7.5 and Figure 7.6.

PP	E_{O}^0 (eV)	$E_{\mathrm{O_2}}^0$ (eV)	$\Delta_{\mathrm{expt}}H$ (eV)	$\Delta_{\mathrm{expt}}\bar{d}$ (Å)
s	−1.606	−9.399	−0.511	0.084
h	−1.565	−10.028	−0.866	0.011
sv	−2042.442	−4091.768	−0.859	0.012
GW	−1.564	−9.925	−0.816	0.019
GW_new	−1.565	−9.997	−0.851	0.016
s_GW	−1.565	−9.508	−0.606	0.065
h_GW	−1.563	−10.027	−0.868	0.011
GW_new		−12.531		0.005

Table 7.4: Experimental comparison for all pseudopotentials of oxygen. Hard pseudopotentials show better bond lengths, whereas soft pseudopotentials are closer to the experiment w.r.t. the enthalpy of formation. Because the latter is more important for further considerations, the `s_GW` type is chosen due to its reasonable compromise between both observables. All calculations were done on a PBE level except the last row which was done with SCAN.

Oxygen Difluoride

OF_2 has a bent structure similar to the water molecule. The O–F bond length is 1.4 Å and the F–O–F angle is 103°. We find that for PBE calculations, OF_2 has a negative enthalpy of formation, whereas SCAN favors ½O_2 + F_2.

Level	E^0 (eV)	$\Delta_{\mathrm{ref}}d$ (Å)	$\Delta_{\mathrm{ref}}\angle$FOF (°)
PBE	−8.572	0.022	1.680
SCAN	−13.059	0.001	0.783

Table 7.5: Total energies for the OF_2 molecule for PBE (`O_s_GW`, `F_h_GW`) and SCAN (`O_GW_new`, `F_GW_new`).
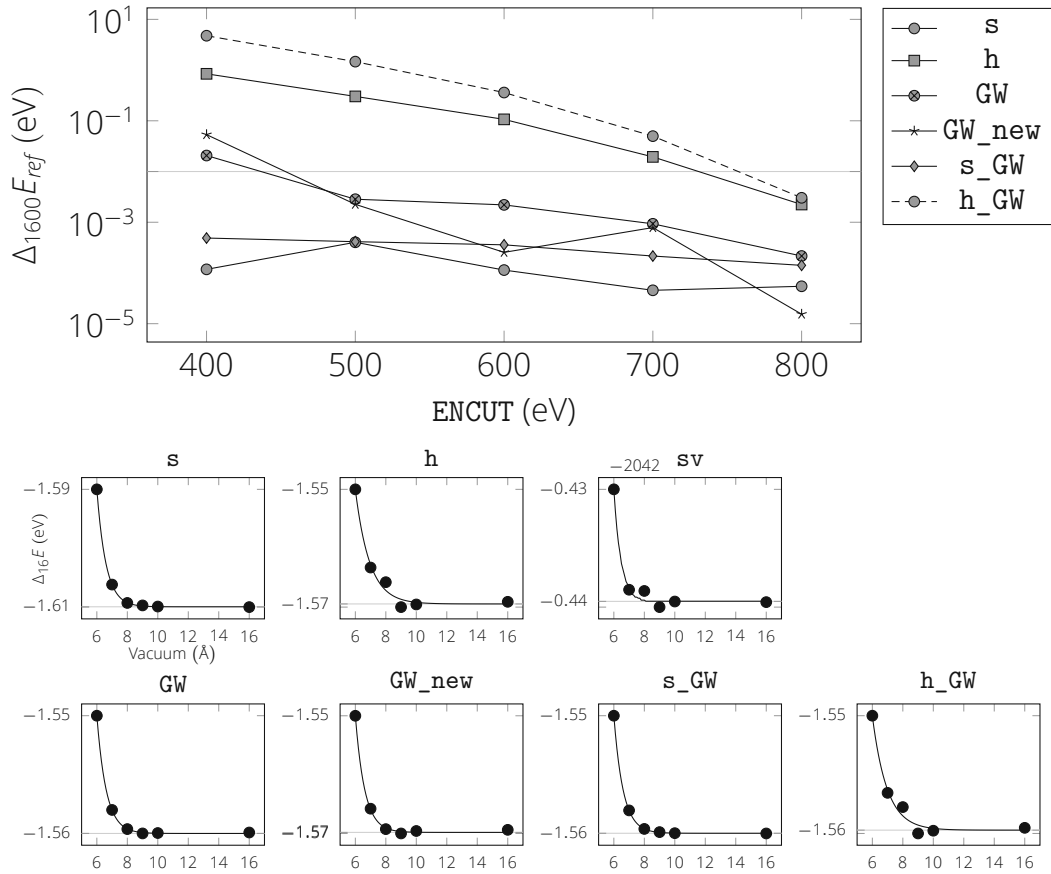
Figure 7.5: Top: Energy cutoff convergence study for the oxygen atom. Off the chart is the `sv` pseudopotential, which is only converged at the unusually high cutoff of 1600 eV, where the reference is 1800 eV. Bottom: Vacuum convergence studies for every pseudopotential. Softer pseudopotentials show smoother convergence with respect to the distance between atoms.
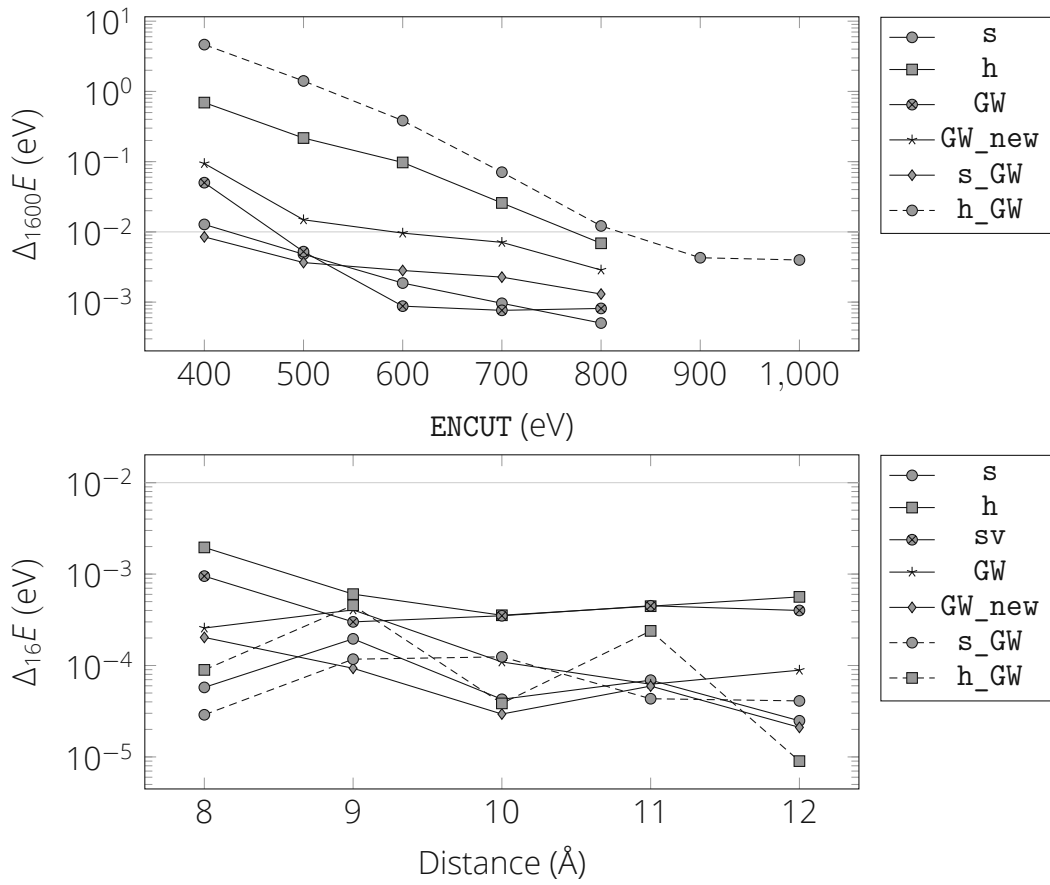
Figure 7.6: Top: Energy cutoff convergence study for the oxygen molecule. The reference cutoff energy is 1600 eV for all pseudopotentials except for the `sv` version, which requires 1800 eV and is converged at 1600 eV. Bottom: Vacuum convergence study.
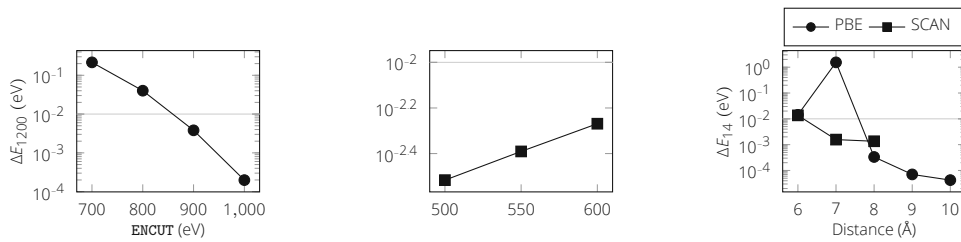
Figure 7.7: Convergence studies of OF_2 with SCAN were done with `O_GW_new` and `F_GW_new` pseudopotentials and PBE with the `O_s_GW` and `F_h_GW` variants. Left: Energy cutoff convergence study. Right: Vacuum convergence study.

Magnesium-Oxygen Compounds

For Mg–O compounds we find one stable phase MgO with its experimental lattice constant 4.213 Å[116] and Bulk modulus 163.447 GPa.[117]

ID	#Mg	#O	Space Group	atoms	E (eV)
1265	1	1	Fm-3m	2	−11.968
2589	1	2	Pa-3	12	−66.513

Table 7.6: Lowest energy phases of magnesium-oxygen compounds found in the materials project's database are listed.[105]

E (eV)				E (eV)
−11.968 =	MgO	<	$^1/_2$MgO$_2$ + $^1/_2$Mg	= −9.114
−16.628 =	MgO$_2$	>	MgO + $^1/_2$O$_2$	= −16.931

Table 7.7: Phases are deemed as stable when for an ideal mixing of its constituents it has a lower energy than all other possible combinations. In this table a < sign indicates a stable phase and > indicates an unstable phase and is disregarded in subsequent considerations.
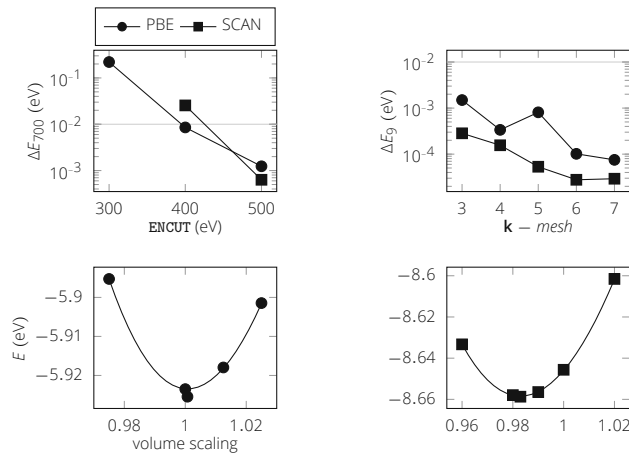
Figure 7.8: Convergence studies for MgO with PBE and SCAN with pseudopotentials `Mg_pv`, `O_s_GW` and `Mg_GW`, `O_GW_new` respectively.

Level	E^0 (eV)	$\Delta_{ref}a$ (Å)	$\Delta_{ref}B$ (GPa)
PBE	−11.851	0.047	−3.182
SCAN	−17.317	0.029	8.572

Table 7.8: Data for MgO on PBE and SCAN level. The total energy is given for two atoms MgO.

Magnesium-Fluorine Compounds

ID	#Mg	#F	Space Group	atoms	E (eV)
1249	1	2	$P4_2/mnm$	6	−31.975
1185862	1	3	I4/mmm	4	−15.497

Table 7.9: Stable phases of magnesium-fluorine compounds found in the materials project's database are listed.[105]

E (eV)			E (eV)
$-15.988 =$	MgF_2	$<$ $^2/_3MgF_3 + ^1/_3Mg$	$= -10.865$

Table 7.10: Phases are deemed as stable when for an ideal mixing of its constituents it has a lower energy than all other possible combinations. In this table a < sign indicates a stable phase and > indicates an unstable phase and is disregarded in subsequent considerations.

Mg_GW	F_GW	E^0 (eV)	$\Delta_{ref}a$ (Å)	$\Delta_{ref}c$ (Å)	$\Delta_{ref}dH$ (eV)
	new	−23.564	−0.019	−0.028	1.043
pv	new	−23.513	−0.019	−0.012	1.096
sv	new	−37.676	−0.019	−0.012	1.087

Table 7.11: Comparison of various pseudopotential combinations of F and Mg with experimental values and the total energy.
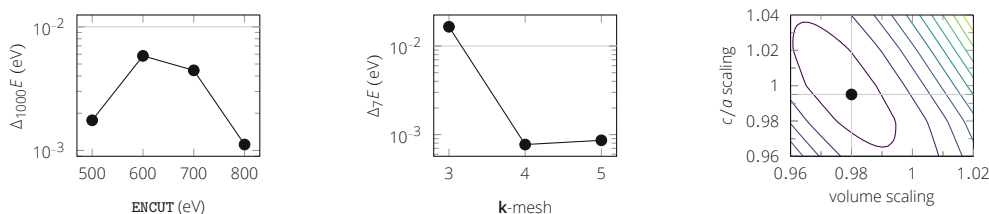
Figure 7.9: Convergence studies of MgF$_2$ for the combination of `F_GW_new` and `Mg_GW` pseudopotentials using the SCAN functional. Left: Energy cutoff convergence. Middle: K-mesh convergence, where the number of grid points in c direction was reduced according to the c/a ratio. Right: Finding the equilibrium geometry.

Table for Compensation Energies

Compound	E^0 (eV)	$\Delta H/Atom$ (eV)
Mg	−4.976	
F$_2$	−6.931	
O$_2$	−12.531	
OF$_2$	−13.059	0.069
MgO	−17.317	−3.038
MgF$_2$	−23.564	−3.886

Table 7.12: Summary of total energies for compounds needed for charge compensation analysis in Th:MgF$_2$ outside of the host crystal. Calculations were done with SCAN and pseudopotentials `Mg_GW`, `F_GW_new` and `O_GW_new`. Convergence studies and experimental comparisons are shown in the previous sections.

A.3 Compensating Thorium doped Calcium Fluoride

Calcium

Gaseous Ca For a gaseous Ca atom, the ionization energy is determined. First, a basic convergence study for the neutral atom was performed and then the interatomic distance between positively charged Ca$^+$ cations was varied and its energy extrapolated. The experimental data for ionization energies shows:[118] $I = 6.113$ eV, $II = 11.872$ eV and $III = 50.913$ eV.
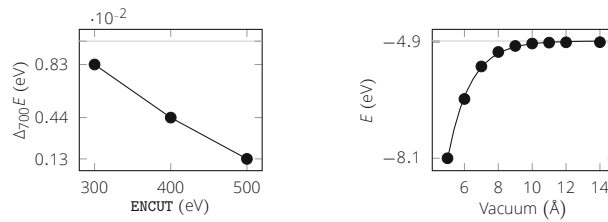
Figure 7.10: Convergence study for Ca gas. Left: Energy Cutoff study showing energy differences with respect to a reference calculation with a cutoff of 700 eV. Right: Vacuum size study with marks for calculation results and a continuous line showing an interpolation function with $E_0 = -4.90$ eV.
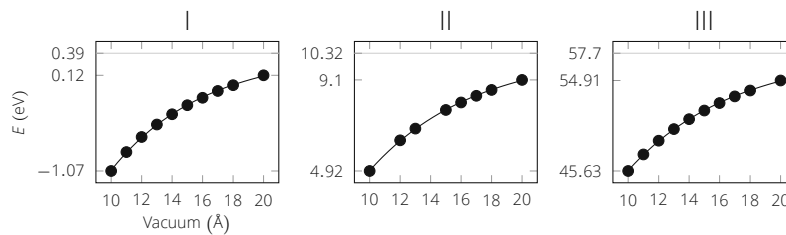
Figure 7.11: Extrapolation for the energy with respect to the vacuum size of an ionized Ca atom, where we interpolate data points. Left: Ionization I ($E_0 = 0.39$ eV), Middle: Ionization II ($E_0 = 10.32$ eV), Right: Ionization III ($E_0 = 57.70$ eV).

Ion.	E_{VASP} (eV)	$\Delta_{\text{expt}}E$ (eV)
I	5.29	0.82
II	9.93	1.94
III	47.38	3.54

Table 7.13: Ionization energies compared to the reference values for a Ca atom.

Crystal Ca The materials project database[105] determines several phases of single Ca crystals, where the cubic lattice has the lowest energy.
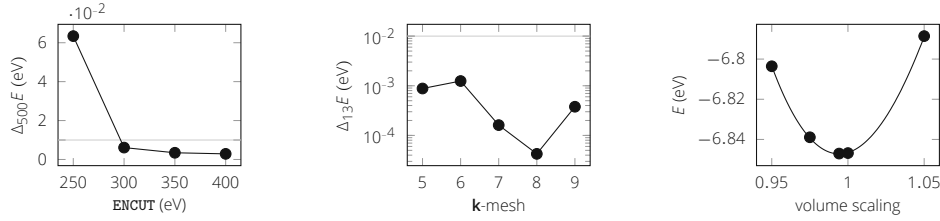
Figure 7.12: Convergence studies for solid Ca with the `Ca_sv_GW` pseudopotential. Left: Energy cutoff convergence. Middle: **k**-mesh convergence. Right: Volume convergence. The relaxed cell volume was taken from the materials project website.[105] We find good agreement with the database values; the minimum lies at 0.99.

The total energy for Ca crystal with the Ca_sv_GW pseudopotential is found to be −6.85 eV and the difference to experimental lattice constant is 0.06 Å.[111]

Calcium-Oxygen

ID	#Ca	#O	Space Group	atoms	E (eV)
2605	1	1	Fm-3m	2	−12.879
634859	1	2	I4/mmm	3	−18.521
1120811	2	3	P1	40	−248.126
1182382	1	10	4/mmm	22	−111.885

Table 7.14: Energetically favorable phases of calcium-oxygen compounds found in the materials project's database are listed.[105]

The final energy for two atoms in the CaO crystal with the `Ca_sv_GW` and `O_s_GW` pseudopotentials is −17.763 eV and its deviation to the experimental lattice vector is 0.023 Å.

Calcium Fluoride

The final total energy of the three CaF$_2$ constituents is −22.314 eV when using `Ca_sv_GW` and `F_h_GW` pseudopotentials. Bader Charge analysis shows an electron reduction on Ca sites by 1.673 and an increase in electron number on F sites by 0.836. We find a difference to the experimental lattice parameter

E (eV)					E (eV)
-12.879	$=$	CaO	$<$	$^1/_3Ca_2O_3 + {}^1/_3Ca$	$=$ -11.007
-18.521	$=$	CaO_2	$>$	$CaO + {}^1/_2O_2$	$=$ -17.841
-31.016	$=$	Ca_2O_3	$>$	$CaO + CaO_2$	$=$ -31.400
-55.943	$=$	CaO_{10}	$>$	$CaO_2 + 4O_2$	$=$ -58.221

Table 7.15: Phases are deemed as stable when for an ideal mixing of its constituents it has a lower energy than all other possible combinations. In this table a $<$ sign indicates a stable phase and $>$ indicates an unstable phase and is disregarded in subsequent considerations.
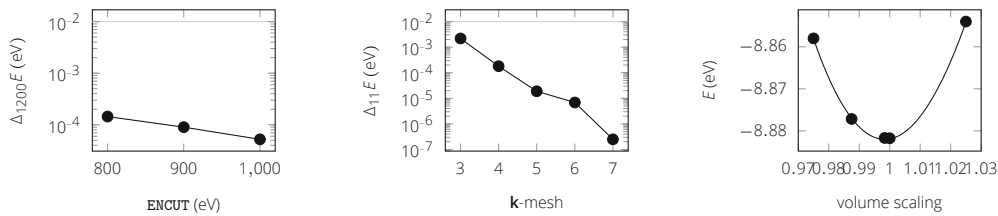
Figure 7.13: **ENCUT** convergence plot for the stable phase CaO. The relaxed cell volume was taken from the materials project website. We find good agreement with the database values, the minimum lies at 0.998.

ID	#Ca	#F	Space Group	atoms	E (eV)
1183545	1	1	$P6_3mc$	4	-18.121
2741	1	2	Fm-3m	3	-17.577
554355	1	2	P4/mmm	3	-16.857
560030	1	2	$Pmc2_1$	6	-34.061
10464	1	2	Pnma	12	-69.684
1183590	1	3	I4/mmm	4	-18.459
1183589	1	3	$P6_3/mmc$	8	-36.869
684949	2	1	Cm	15	-57.061

Table 7.16: All phases of calcium-fluorine compounds found in the materials project's database are listed.[105]

E (eV)				E (eV)
$-9.061 =$	CaF	$>$	$\frac{1}{2}CaF_2 + \frac{1}{2}Ca$	$= -9.792$
$-17.577 =$	CaF_2	$<$	$\frac{2}{3}CaF_3 + \frac{1}{3}Ca$	$= -12.974$
$-18.459 =$	CaF_3	$>$	$CaF_2 + \frac{1}{2}F_2$	$= -19.468$
$-11.412 =$	Ca_2F	$>$	$\frac{1}{2}CaF_2 + \frac{3}{2}Ca$	$= -11.798$

Table 7.17: Phases are deemed as stable when for an ideal mixing of its constituents it has a lower energy than all other possible combinations. In this table a $<$ sign indicates a stable phase and $>$ indicates an unstable phase and is disregarded in subsequent considerations.
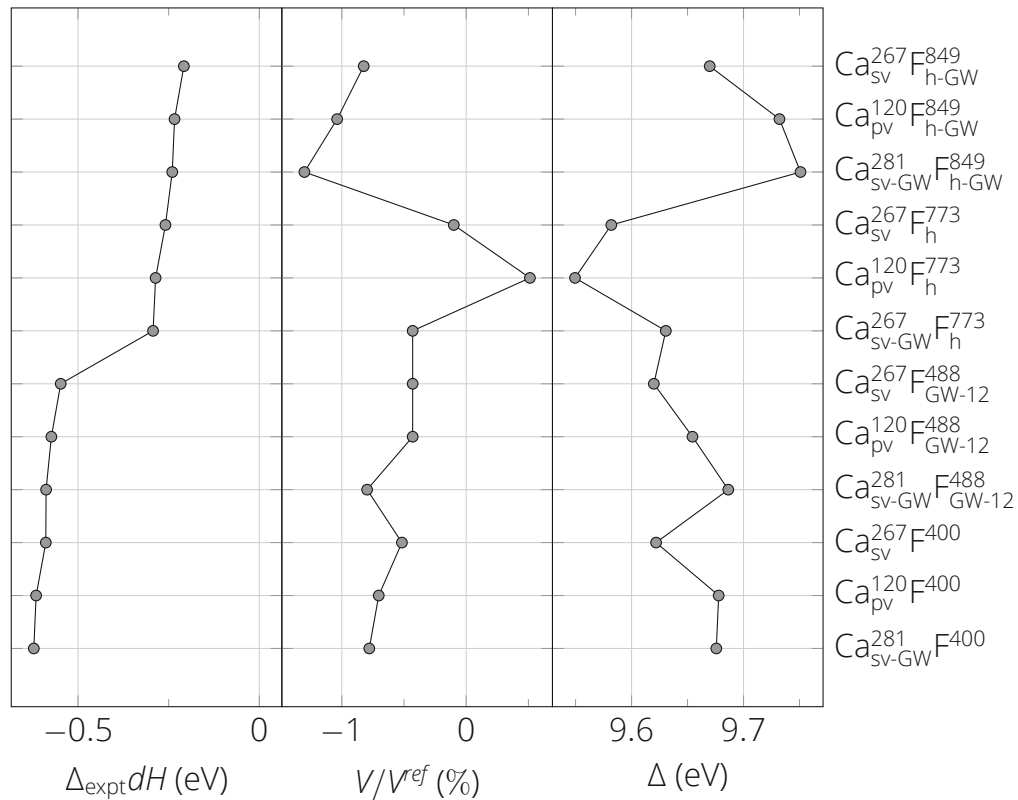

Figure 7.14: Different Pseudopotential combinations for enthalpy of formation (left), (volume) and band gap (right) for the SCAN mGGA.
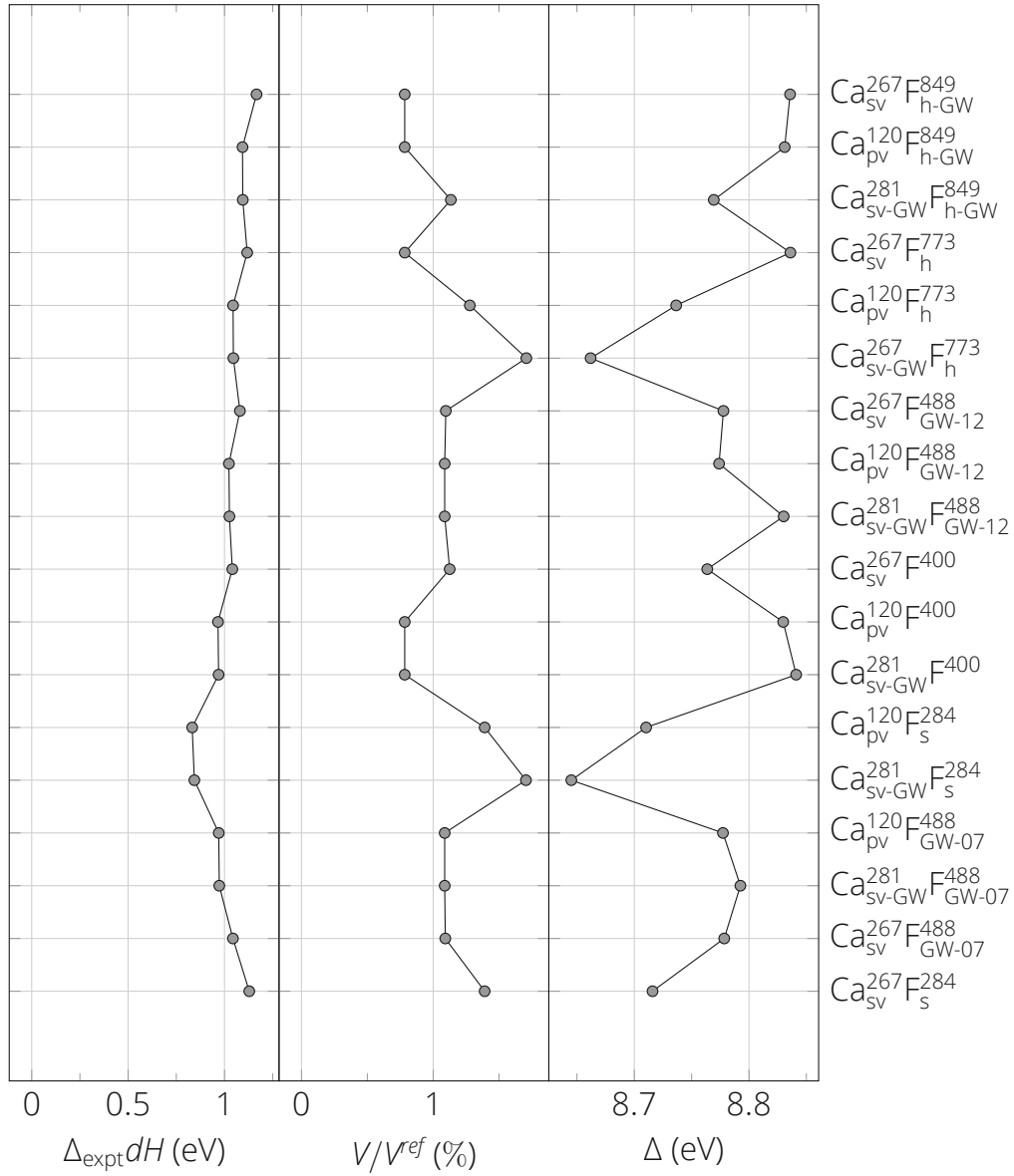
Figure 7.15: Different Pseudopotential combinations for enthalpy of formation (left), (volume) and band gap (right) for the PBE GGA.
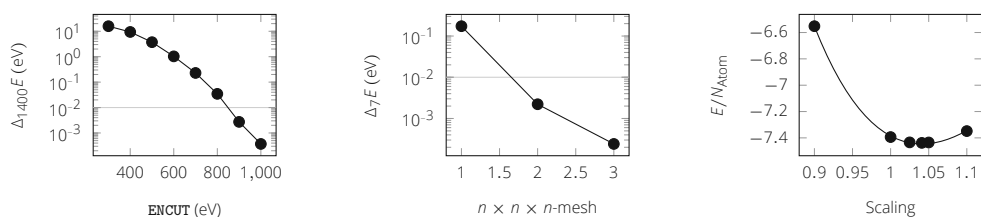
Figure 7.16: Convergence studies for CaF$_2$ with `Ca_sv_GW` and `F_h_GW` pseudopotentials.

of 0.061 Å and to the experimental Bulk modulus of -1.764 GPa.[82,83,117] For this combination of pseudopotentials, we calculate an enthalpy of formation of -11.772 eV, which is a difference to the experimental value of -0.122 eV.[119]

Table for Compensation Energies

Compound	E^0 (eV)	$\Delta H/Atom$ (eV)
Ca	−6.847	
F$_2$	−3.695	
O$_2$	−9.508	
OF$_2$	−8.572	−0.041
CaO	−17.763	−3.081
CaF$_2$	−22.314	−3.924

Table 7.18: Summary of total energies for compounds needed for charge compensation analysis in Th:CaF$_2$ outside of the host crystal. Calculations were done with PBE and pseudopotentials `Ca_sv_GW`, `F_h_GW` and `O_s_GW`. Convergence studies and experimental comparisons are shown in the previous sections.

A.4   Compensating Thorium Doped LICAF

Lithium

We obtain a total energy for one crystal Li atom with the `Li_GW` pseudopotential of -1.892 eV.

Aluminum

We obtain a converged total energy for the `Al_GW` pseudopotential of -3.742 eV

ID	Space Group	Atoms	E (eV)	E (eV/Atom)
51	Fm-3m	1	−1.906	0.003
135	Im-3m	1	−1.904	0.005
10173	$P6_3/mmc$	2	−3.813	0.002
1018134	R-3m	3	−5.727	0.000
1063005	P6/mmm	3	−5.671	0.019
976411	$P6_3/mmc$	4	−7.625	0.003
604313	$P4_132$	4	−6.589	0.262
567337	I-43d	8	−15.189	0.010
1103107	Cmce	12	−22.243	0.055

Table 7.19: Phases and PBE energies of Li on the materials project database.[105] All calculations are performed with the `Li_sv` pseudopotential. Contrary to what one might expect, the lowest lying energy is not the cubic but a trigonal lattice. In an experimental database, we find three different phases which do not turn out to be energetically lowest in DFT.[111] We speculate that the significance is very low, since there are several phases which are just a few meV apart and omit our own investigation into this manner.
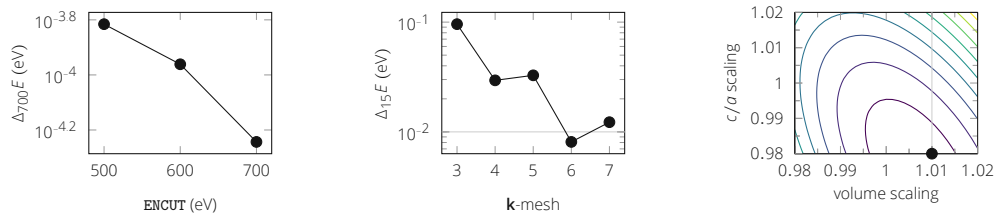
Figure 7.17: Convergence studies for the trigonal phase of solid Li. Left: Energy cutoff convergence. Middle: K-mesh convergence. The unit cell has a ratio $c/a > 7$. Thus, values on the x-axis are only for a and b dimensions in reciprocal space, whereas only a single k-point was used in c-direction. The reference values were obtained using a $15 \times 15 \times 2$ mesh. Right: Volume convergence. The relaxed cell volume was taken from the materials project website. The dot represents our lowest calculated value, the true minimum is obtained by Morse fits.

ID	Space Group	Atoms	E (eV)	E (eV/Atom)
134	Fm-3m	1	−3.746	0.000
998860	Im-3m	1	−3.653	0.093
1183144	P6$_3$/mmc	4	−14.937	0.011
1239196	I4/mmm	4	−13.774	0.302

Table 7.20: Phases and PBE energies of Al on the materials project database.[105] All calculations are performed with the `Al` pseudopotential. The lowest lying energy is the fcc cubic lattice.
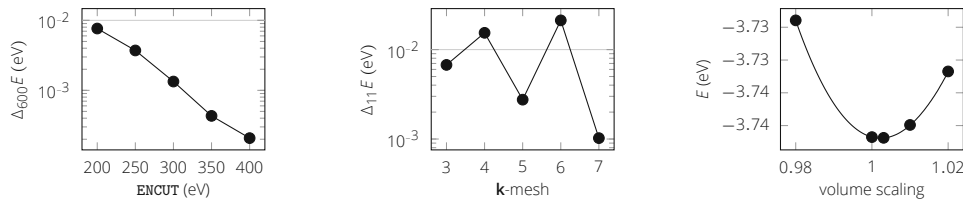
Figure 7.18: Convergence studies for solid Al. Left: Energy cutoff convergence. Middle: K-mesh convergence. Right: Volume convergence. The relaxed cell volume was taken from the materials project website.[105]

and differences to the experimental values of the lattice constant of $-0.002\,\text{Å}$ and Bulk modulus of $-1.089\,\text{GPa}$.[111,117]

Lithium-Calcium

ID	#Li	#Ca	Space Group	atoms	E (eV)
11644	2	1	Fd-3m	6	−11.717
570466	2	1	P6$_3$/mmc	12	−23.387
976075	3	1	I4/mmm	4	−7.550
975929	3	1	Fm-3m	4	−7.538
976272	1	3	I4/mmm	4	−7.634
1185350	1	3	P6$_3$/mmc	8	−15.341
1211157	1	4	Fd-3m	10	−16.713

Table 7.21: All phases of lithium calcium compounds found in the materials project's database are listed.[105]

E (eV)				E (eV)
$-5.858 =$	Li_2Ca	$<$	$2Li + Ca$	$= -5.823$
$-7.550 =$	Li_3Ca	$>$	$Li_2Ca + Li$	$= -7.767$
$-7.634 =$	$LiCa_3$	$>$	$^1/_2Li_2Ca + ^5/_2Ca$	$= -7.943$
$-7.670 =$	$LiCa_4$	$>$	$^1/_2Li_2Ca + ^7/_2Ca$	$= -9.949$

Table 7.22: Phases are deemed as stable when for an ideal mixing of its constituents it has a lower energy than all other possible combinations. In this table a $<$ sign indicates a stable phase and $>$ indicates an unstable phase and is disregarded in subsequent considerations.
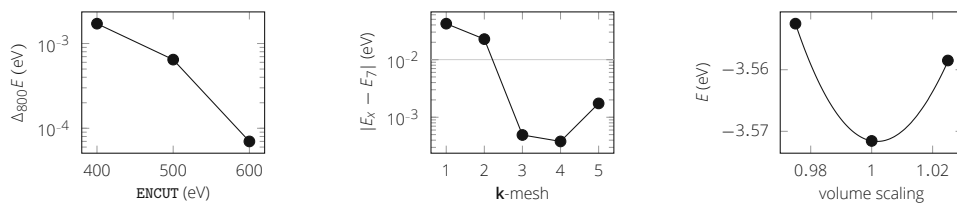
Figure 7.19: Convergence studies for the stable Li_2Ca phase. Left: Energy cut-off convergence. Middle: **k**-mesh convergence. Right: Determination of equilibrium volume. The relaxed cell volume was taken from the materials project website.[105]

101

The final energy for Li_2Ca with the `Li_GW` and `Ca_sv_GW` pseudopotentials is -10.698 eV.

Lithium-Aluminum

ID	#Li	#Al	Space Group	atoms	E (eV)
1067	1	1	Fd-3m	4	−12.020
1079240	1	1	P6$_3$/mmc	8	−23.346
1191737	1	1	Cmce	24	−68.592
1211134	1	2	Fd-3m	12	−34.711
10890	1	3	Pm-3m	4	−13.552
975906	1	3	I4/mmm	4	−13.466
1210753	2	1	Cmcm	6	−16.104
1210792	2	1	Fd-3m	12	−28.263
975868	3	1	I4/mmm	4	−9.791
16506	3	2	R-3m	5	−14.154
1212183	7	6	Cmmm	13	−14.983
568404	9	4	C2/m	13	−34.045

Table 7.23: All phases of lithium-aluminum compounds found in the materials project's database are listed.[105]

E (eV)				E (eV)
$-6.010 =$	LiAl	$<$	$^1/_3Li_3Al_2 + {}^1/_3Al$	$= -5.967$
$-8.678 =$	LiAl$_2$	$>$	$LiAl + Al$	$= -9.756$
$-13.552 =$	LiAl$_3$	$<$	$LiAl + 2Al$	$= -13.502$
$-8.052 =$	Li$_2$Al	$<$	$^1/_2Li_3Al_2 + {}^1/_2Li$	$= -8.032$
$-9.791 =$	Li$_3$Al	$>$	$Li_2Al + Li$	$= -9.961$
$-14.154 =$	Li$_3$Al$_2$	$<$	$^3/_2Li_2Al + {}^1/_2Al$	$= -13.951$
$-14.983 =$	Li$_7$Al$_6$	$>$	$^7/_3Li_3Al_2 + {}^4/_3Al$	$= -38.021$

Table 7.24: Phases are deemed as stable when for an ideal mixing of its constituents it has a lower energy than all other possible combinations. In this table a $<$ sign indicates a stable phase and $>$ indicates an unstable phase and is disregarded in subsequent considerations.

Note that the compound Li_7Al_6 is one of the rare instances where the algorithm fails to find the lowest energy solution since it is assumed that each ele-

ment is completely absorbed by only one compound. Li_7Al_6 in fact composes to

$$Li_3Al_2 + 4LiAl = -38.194\,eV, \tag{7.4}$$

which is impossible to find in our algorithm since none of these two compounds completely absorbs an element. Instead our algorithm erroneously gives the pathway

$$^7/_3Li_3Al_2 + {^4/_3}Al = -38.021\,eV. \tag{7.5}$$

It seems that in this case neither of the two phases are dominant.
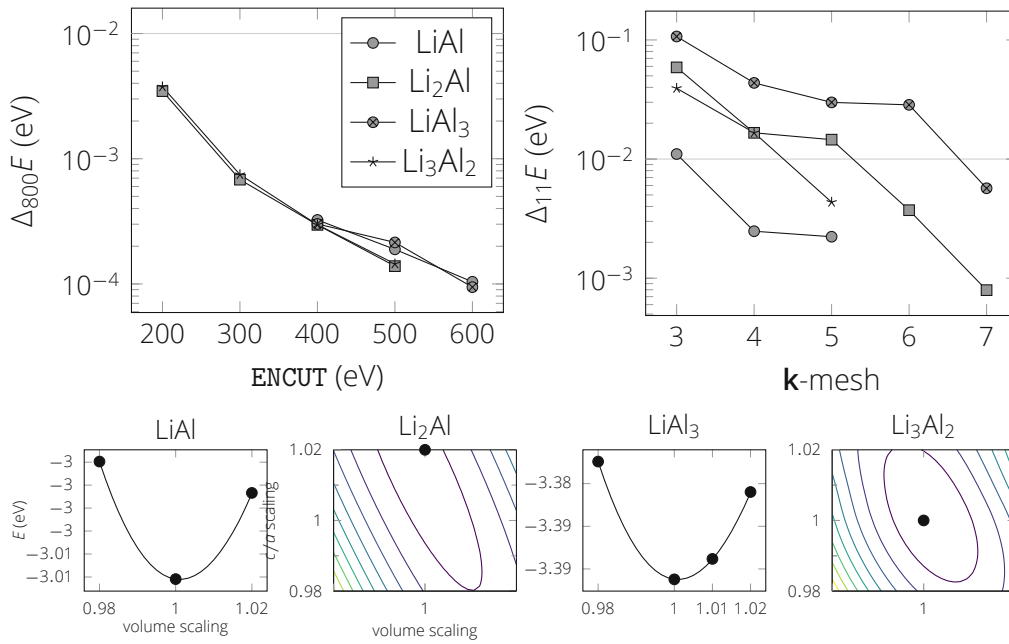
Figure 7.20: Convergence studies for the selected phases of Li – Al compounds with pseudopotentials `Li_sv_GW` and `Al_GW`. Cell parameters were obtained from the materials project database.[105] The black dot in the contour plot illustrates our calculation with the lowest energy. The true minimum may be obtained by the Morse fit.

Lithium-Fluorine

The final energy for LiF with pseudopotentials `Li_GW` and `F_h_GW` is $-9.611\,eV$ with differences in lattice parameter and Bulk modulus being $0.039\,\text{Å}$ and $-10.499\,GPa$ respectively.

Compound	E^0 (eV)	$\Delta_{ref}a$ (Å)	$\Delta_{ref}c$ (Å)
LiAl	−6.016	0.003	
LiAl$_3$	−13.565	0.016	
Li$_2$Al	−8.024		
Li$_3$Al$_2$	−14.097	−0.042	0.113

Table 7.25: Converged final energies for compounds with pseudopotentials `Li_GW` and `Al_GW` and differences to experimental lattice parameters if available.[120–122]

ID	#Li	#F	Space Group	atoms	E (eV)
1138	1	1	Fm-3m	2	−9.690
1009009	1	1	Pm-3m	2	−9.115
1185301	1	1	P6$_3$mc	4	−19.354
1185348	1	3	P6$_3$/mmc	8	−23.980

Table 7.26: All phases of lithium-fluorine compounds found in the materials project's database are listed.[105]

E (eV)				E (eV)
−9.690 =	LiF	<	$^1/_3$LiF$_3$ + $^2/_3$Li	= −5.269
−11.990 =	LiF$_3$	>	LiF + F$_2$	= −13.472

Table 7.27: Phases are deemed as stable when for an ideal mixing of its constituents it has a lower energy than all other possible combinations. In this table a < sign indicates a stable phase and > indicates an unstable phase and is disregarded in subsequent considerations.
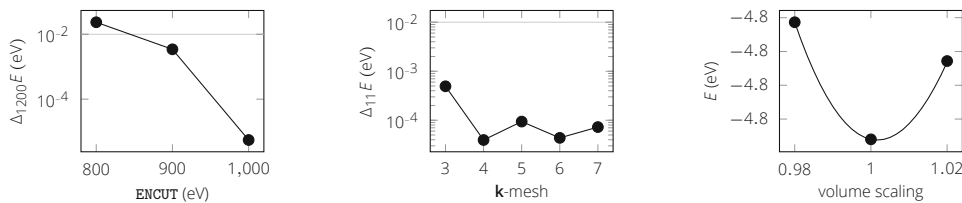

Figure 7.21: Convergence studies for LiF. Left: Energy cutoff convergence. Middle: **k**-mesh convergence. Right: Determination of equilibrium volume. The relaxed cell volume was taken from the materials project website.[105] We find good agreement with the database values; the minimum lies at 0.997.

Calcium-Aluminum

For Ca – Al compounds we find three stable phases $CaAl_2$, Ca_8Al_3 and $Ca_{13}Al_{14}$ with energies -15.319, -67.800 and -148.619 respectively in units of eV.

ID	#Ca	#Al	Space Group	atoms	E (eV)
2404	1	2	Fd-3m	6	-20.961
1749	1	4	I4/mmm/1	5	-17.962
1214044	4	1	Fd-3m	10	-20.134
1190736	8	3	P1	22	-57.964
1193055	13	14	C2/m	27	-85.527

Table 7.28: All phases of calcium-aluminum compounds found in the materials project's database are listed.[105]

E (eV)				E (eV)
$-10.480 =$	$CaAl_2$	$<$	$^1/_{13}Ca_{13}Al_{14} + {}^{12}/_{13}Al$	$= -10.037$
$-17.962 =$	$CaAl_4$	$>$	$CaAl_2 + 2Al$	$= -17.972$
$-10.067 =$	Ca_4Al	$>$	$^1/_3Ca_8Al_3 + {}^4/_3Ca$	$= -12.335$
$-28.982 =$	Ca_8Al_3	$<$	$^3/_{14}Ca_{13}Al_{14} + {}^{73}/_{14}Ca$	$= -28.787$
$-85.527 =$	$Ca_{13}Al_{14}$	$<$	$7CaAl_2 + 6Ca$	$= -85.398$

Table 7.29: Phases are deemed as stable when for an ideal mixing of its constituents it has a lower energy than all other possible combinations. In this table a $<$ sign indicates a stable phase and $>$ indicates an unstable phase and is disregarded in subsequent considerations.

Compound	E^0 (eV)
$CaAl_2$	-15.319
Ca_8Al_3	-67.800
$Ca_{13}Al14$	-148.619

Table 7.30: Converged final energies for Ca – Al compounds with pseudopotential `Ca_sv_GW` and `Al_GW`
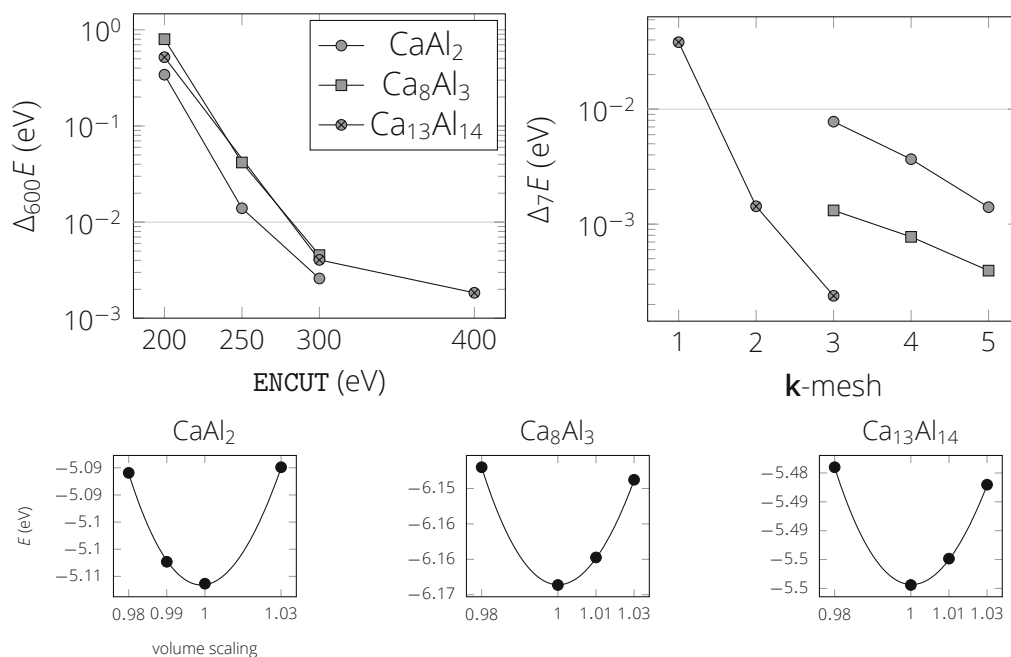
Figure 7.22: Convergence studies for stable phases of Ca – Al compounds. Top left: Energy convergence. Top right: **k**-mesh convergence. Bottom: Determination of the PBE equilibrium cell volume.

ID	Space Group	Atoms	E (eV)	E (eV/Atom)
8039	Pm-3m	4	−23.5729	0.0007
468	R-3c	8	−47.1510	0.0000
1183007	C2/c	8	−47.0766	0.0093
125276	Cmmm	8	−46.8699	0.0352
1251148	P2/m	8	−46.8618	0.0362
1182902	P1	8	−46.8186	0.0416
635425	P1	8	−44.9770	0.2718
110329	P321	12	−70.6916	0.0029
559871	Cmcm	24	−141.4193	0.0014
555026	P4/mbm	40	−235.5522	0.0051
1323	P4/nmm	64	−376.3264	0.0138

Table 7.31: Phases and PBE energies of AlF_3 on the materials project's database.[105] All calculations are performed with the `std` pseudopotentials. A few phases are very close in energy.

E (eV)				E (eV)
$-23.576 =$	AlF_3	$<$	$Al + {}^3/_2 F_2$	$= -9.419$

Table 7.32: Phases are deemed as stable when for an ideal mixing of its constituents it has a lower energy than all other possible combinations. In this table a $<$ sign indicates a stable phase and $>$ indicates an unstable phase and is disregarded in subsequent considerations.

Figure 7.23: Convergence studies if AlF_3. Left: Energy cutoff convergence. Middle: **k**-mesh convergence. The mesh has the same ratio $c/a = 2.506$ as the unit cell. Right: Determination of equilibrium volume where we observe interpolation artifacts. The relaxed cell volume was taken from the materials project website.[105]

Aluminum-Fluorine

The final converged energy for the most stable phase of AlF_3 with the `Al_GW` and `F_h_GW` pseudopotentials is -23.409 eV.

Lithium-Calcium-Aluminum

ID	#Li	#Ca	#Al	Space Group	atoms	E (eV)
1079781	1	1	3	$P6_3/m$	10	-28.289
862632	1	2	1	Fm-3m	4	-10.239
1185028	2	1	1	Fm-3m	4	-10.022
1096622	2	1	1	Immm	4	-3.928

Table 7.33: All phases of lithium-calcium-aluminum compounds found in the materials project's database are listed.[105]

The total energy for a $LiCa_2Al$ unit is -19.923 eV.

E (eV)				E (eV)
$-14.145 =$	$LiCaAl_3$	$>$	$LiAl + CaAl_2$	$= -16.490$
$-10.239 =$	$LiCa_2Al$	$<$	$^1/_4Ca_8Al_3 + {}^1/_4Li_2Al + {}^1/_2Li$	$= -10.213$
$-10.022 =$	Li_2CaAl	$>$	$^1/_2LiCa_2Al + {}^1/_2Li_2Al + {}^1/_2Li$	$= -10.100$

Table 7.34: Phases are deemed as stable when for an ideal mixing of its constituents it has a lower energy than all other possible combinations. In this table a $<$ sign indicates a stable phase and $>$ indicates an unstable phase and is disregarded in subsequent considerations.
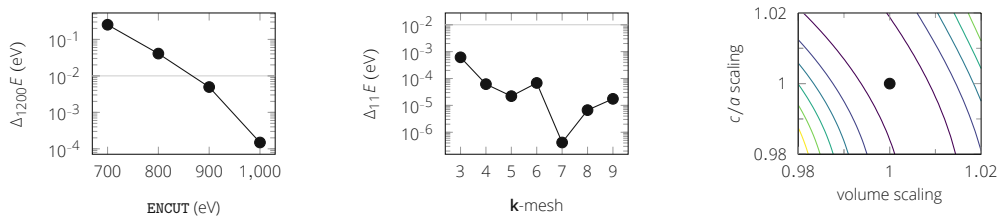

Figure 7.24: Convergence studies for $LiCa_2Al$. Left: Energy cutoff convergence. Middle: **k**-mesh convergence. Right: Determination of the PBE equilibrium cell volume.

Lithium-Aluminum-Fluorine

ID	Space Group	Atoms	E (eV)	E (eV/Atom)
1111291	Fm-3m	10	-51.3383	0.1658
556020	Pna2$_1$	40	-211.7593	0.0056
15254	C2/c	60	-317.9733	0.0000

Table 7.35: Phases and PBE energies of Li_3AlF_6 on the materials project database.[105] All calculations are performed with the `Li_sv` and `std` pseudopotentials. A few phases are very close in energy.

The final energy for the compound Li_3AlF_6 with pseudopotentials of type `Li_GW`, `Al_GW` and `F_h_GW` is -52.625 eV.

Lithium-Calcium-Fluorine

No stable Li – Ca – F compounds have been found.

E (eV)			E (eV)
$-52.996 =$	Li_3AlF_6	$<$ $3LiF + AlF_3$	$= -52.646$

Table 7.36: Phases are deemed as stable when for an ideal mixing of its constituents it has a lower energy than all other possible combinations. In this table a $<$ sign indicates a stable phase and $>$ indicates an unstable phase and is disregarded in subsequent considerations.
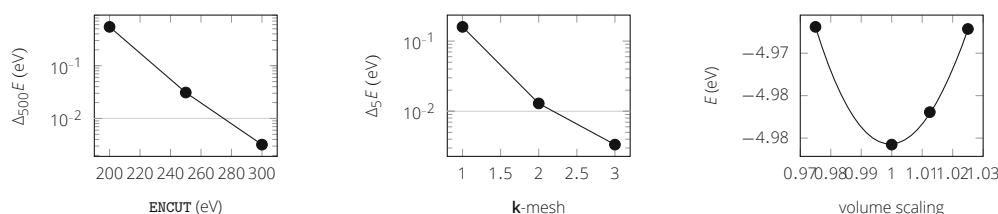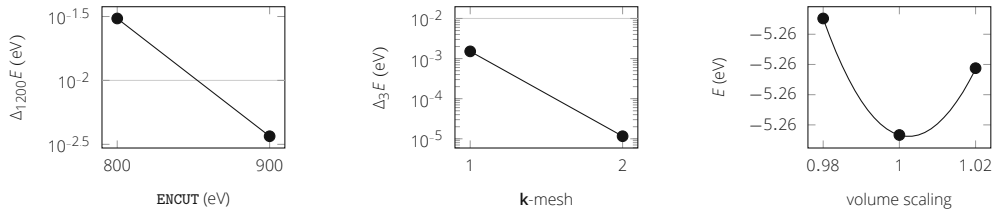

Figure 7.25: Convergence studies for Li_3AlF_6. Left: Energy cutoff convergence. Middle: **k**-mesh convergence. Right: determination of the PBE equilibrium cell volume.

ID	#Li	#Ca	#F	Space Group	atoms	E (eV)
1017626	1	1	3	Pm-3m	5	-26.331

Table 7.37: The only phase $LiCaF_3$ found in the materials project's database is shown.[105]

E (eV)			E (eV)
$-26.331 =$	$LiCaF_3$	$>$ $LiF + CaF_2$	$= -27.268$

Table 7.38: Phases are deemed as stable when for an ideal mixing of its constituents it has a lower energy than all other possible combinations. In this table a $<$ sign indicates a stable phase and $>$ indicates an unstable phase and is disregarded in subsequent considerations.

Calcium-Aluminum-Fluorine

ID	#Ca	#Al	#F	Space Group	atoms	E (eV)
8836	1	1	5	C2/c	14	−82.497
16795	1	1	5	$P2_1/c$	28	−164.903
1213962	1	2	8	C2/c	22	−128.148
1227363	1	2	10	C2	13	−67.219
29221	2	1	7	Pnma	40	−235.207

Table 7.39: All phases of calcium-aluminum-fluorine compounds found in the materials project's database are listed.[105]

E (eV)			E (eV)
$-41.248 =$	$CaAlF_5$	$< \quad {}^1\!/_2 Ca_2AlF_7 + {}^1\!/_2 AlF_3$	$= -41.189$
$-64.074 =$	$CaAl_2F_8$	$> \quad CaAlF_5 + AlF_3$	$= -64.824$
$-67.219 =$	$CaAl_2F_{10}$	$> \quad CaAlF_5 + AlF_3 + F_2$	$= -68.606$
$-58.802 =$	Ca_2AlF_7	$> \quad CaAlF_5 + CaF_2$	$= -58.826$

Table 7.40: Phases are deemed as stable when for an ideal mixing of its constituents it has a lower energy than all other possible combinations. In this table a $<$ sign indicates a stable phase and $>$ indicates an unstable phase and is disregarded in subsequent considerations.
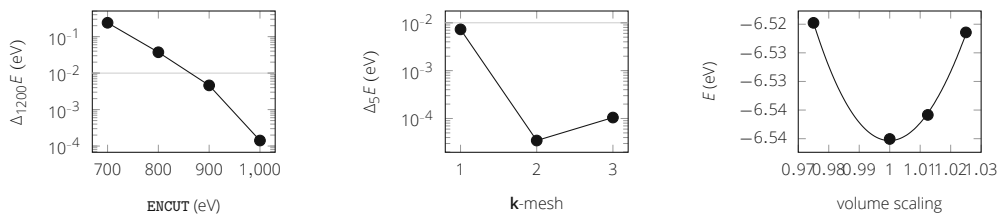

Figure 7.26: Convergence studies of $CaAlF_5$. The relaxed cell volume was taken from the materials project website.[105] We find good agreement with the database values, the minimum lies at 1.000.

The final converged total energy for $CaAlF_5$ with the `Ca_sv_GW`, `Al_GW` and `F_h_GW` pseudopotentials is −45.780 eV.

E (eV)				E (eV)
$-51.204 =$	$LiCaAlF_6$	$<$	$CaF_2 + \frac{1}{3}Li_3AlF_6 + \frac{2}{3}AlF_3$	$= -50.960$

Table 7.41: Phases are deemed as stable when for an ideal mixing of its constituents it has a lower energy than all other possible combinations. In this table a $<$ sign indicates a stable phase and $>$ indicates an unstable phase and is disregarded in subsequent considerations.
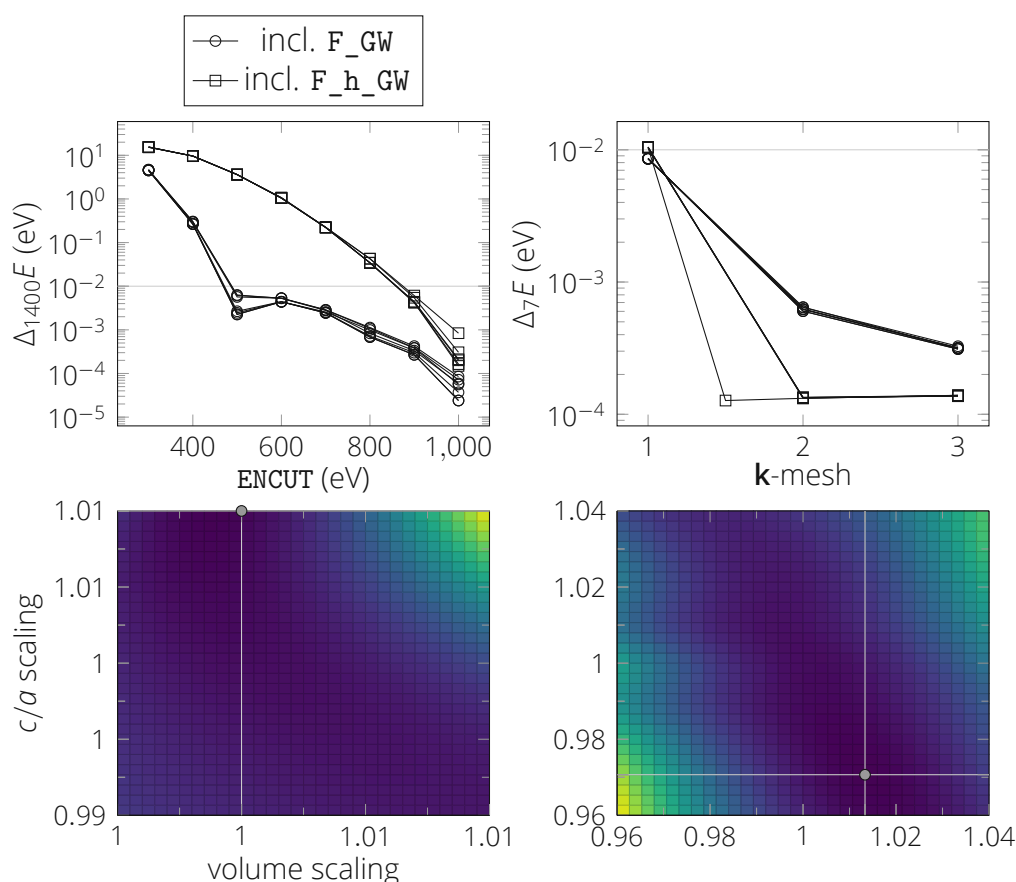
Figure 7.27: Top left: Energy cutoff convergence study. The convergence is entirely dependent on the choice of the pseudopotential for fluorine. Top right: K-mesh convergence study. The data point at 1.5 indicates a $2 \times 2 \times 1$ mesh, while other points were calculated with a $n \times n \times n$ mesh. Bottom left: Varying lattice constants for the LICAF unit cell. Bottom right: Varying the lattice constants for Th:LICAF with substitutional doping for Ca and +2F interstitials.

Lithium-Calcium-Aluminum-Fluoride

Because there are four different elements in LICAF, the number of all possible permutations of PPs is extremely large. Therefore, the number of convergence studies is reduced by disregarding PPs if they were not calculated with the GW method. In the case of fluorine the outdated GW-pseudopotential was also not considered. This reduces the number of possible pseudopotentials to three for Li one for Ca and two for Al and for F, respectively.

Name	Date	# e^-	ENMAX
Li_GW	11 May 2007	1	112
Li_AE_GW	25 Mar 2010	3	434
Li_sv_GW	25 Mar 2010	3	434
Ca_sv_GW	31 Mar 2010	10	281
Al_sv_GW	2 Feb 2008	11	411
Al_GW	19 Mar 2012	3	240
F_GW	19 Mar 2012	7	488
F_h_GW	20 May 2014	7	849

Table 7.42: Types of pseudopotentials for all elements in LICAF.

Compared to the reference values we find a discrepancy in length of the lattice vector $\Delta_{\text{expt.}}a = 0.077$ and $\Delta_{\text{expt}}c = 0.208$ in units of Å.[18] The final converged energy for LiCaAlF$_6$ is -55.714 eV. Considering the observations in Figure 7.27 and in Figure 7.28, we opt for the Li_GW, Al_GW, Ca_sv_GW and F_h_GW pseudopotentials, we set ENCUT = 900 and calculate only on the Γ point to generate the dataset.
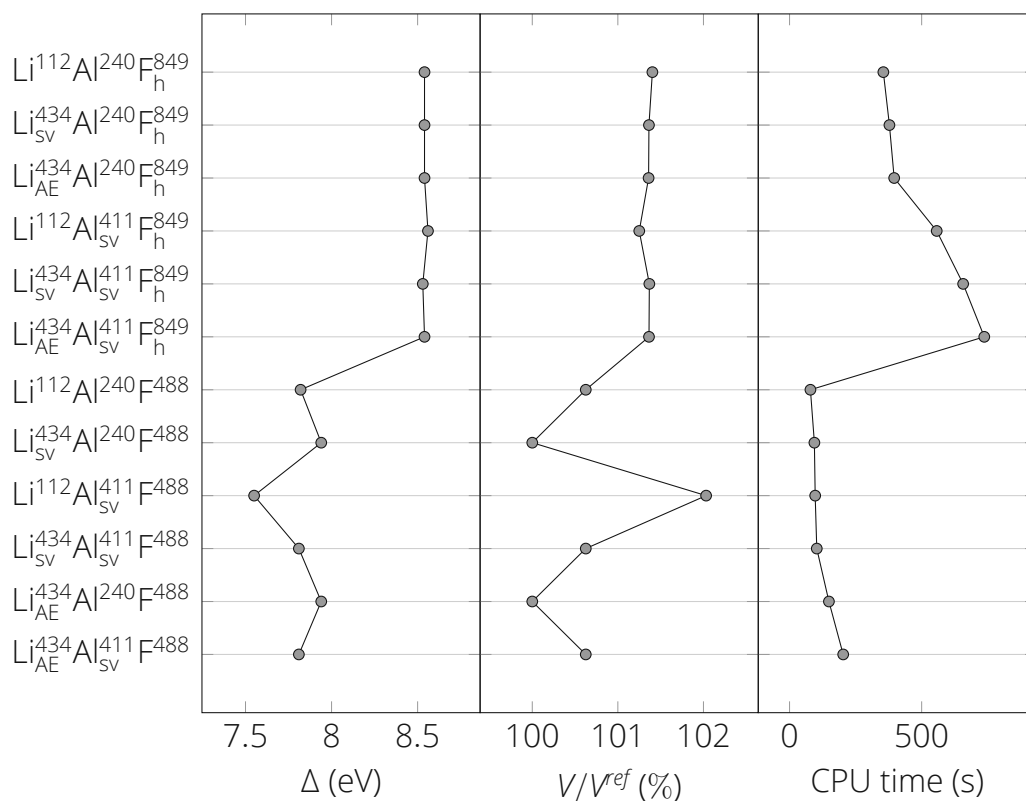
Figure 7.28: Comparison of combinations for pseudopotentials. Left: Energy Gap Δ, which shows a dependence on the fluorine pseudopotential. Since we want to counter the underestimation of the band gap as much as possible we use the hard pseudopotential. Middle: Volume with respect to the reference.[18] Right: CPU time of the unit cell on the cluster with 48 cores. Naturally, an increase in computational time can be observed when using a pseudopotentials with more electrons.

Table for Compensation Energies

Compound	E^0 (eV)
Li	−1.892
Ca	−6.847
Al	−3.742
F_2	−3.695
Li_2Ca	−10.698
LiAl	−6.016
$LiAl_3$	−13.565
Li_2Al	−8.024
Li_3Al_2	−14.097
LiF	−9.611
$CaAl_2$	−15.319
Ca_8Al_3	−67.800
$Ca_{13}Al_{14}$	−148.619
CaF_2	−22.314
AlF_3	−23.409
$LiCa_2Al$	−19.923
Li_3AlF_6	−58.060
$CaAlF_5$	−45.780
$LiCaAlF_6$	−55.714

Table 7.43: Summary of total energies for compounds needed for charge compensation analysis outside of the host crystal. Calculations were done with PBE and pseudopotentials `Li_GW`, `Ca_sv_GW`, `Al_GW` and `F_h_GW` convergence studies and experimental comparisons are shown in the previous sections.

A.5 Heavy Elements

Actinium

For Ac we find an experimental lattice constant at standard conditions for the fcc structure at 5.31 Å.[111] However, the corresponding entry 10018 in the materials project database[105] shows 5.66 Å which is a surprisingly large discrepancy. Indeed in our calculations we arrive at the roughly the same lattice constant as the materials project.
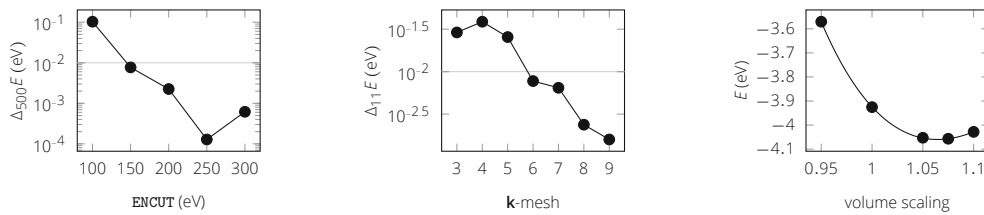
Figure 7.29: Convergence studies for a fcc Ac single crystal. Left: Energy cut-off convergence. Middle: K-mesh convergence. Right: Volume convergence. Compared against the experimental value for the lattice constant, the relative deviation is 1.07.

Cerium

Experimental data shows three phases of solid Ce. In particular, there are two fcc structures αCe and γCe where the γ variant exists at room temperature and the α phase at $-177\,°C$. We could compare against the experimental elastic moduli for the γ phase[123] but were unable to converge on it even when starting from the lattice parameters for γ. Nevertheless, the structure parameters are in good agreement with the experiment with the relative deviation being 1.79 %.
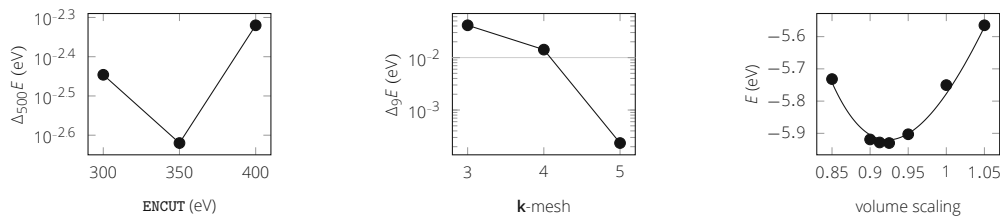
Figure 7.30: Convergence studies for a fcc Ce single crystal. Left: Energy cutoff convergence. Middle: K-mesh convergence. Right: Volume convergence. Note that the initial point, i.e. scaling $= 1$ is for the γCe phase, which is considerably larger than the αCe phase. Relative to the lattice vectors for the α phase, the minimum scaling factor is 0.98.

Neptunium

Solid Neptunium has a stable αNp phase at standard conditions. The differences for our calculated best configuration to the experimental lattice vectors are $\Delta_{expt}a = -0.056\,Å$, $\Delta_{expt}b = -0.091\,Å$ and $\Delta_{expt}c = -0.076\,Å$.
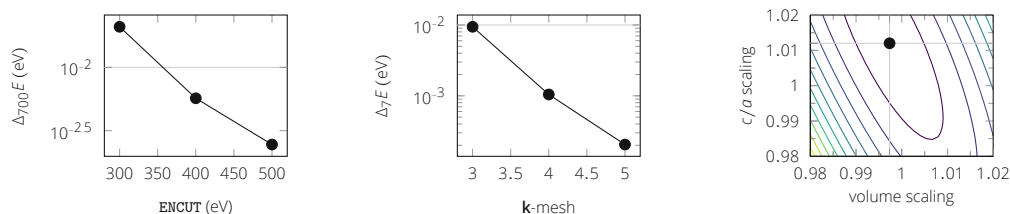
Figure 7.31: Convergence studies for solid αNp. The volume convergence was performed on the materials project values for the lattice constants.[105]

Thorium

VASP supplies two pseudopotentials for thorium, namely the *default*, here called `std` and a soft `s` version. We test the potentials on the ionization energies, lattice parameters and bulk modulus.

Gaseous Thorium   First the neutral atom's energy is calculated. Thereafter, the ionized atom is calculated to determine the ionization energy.
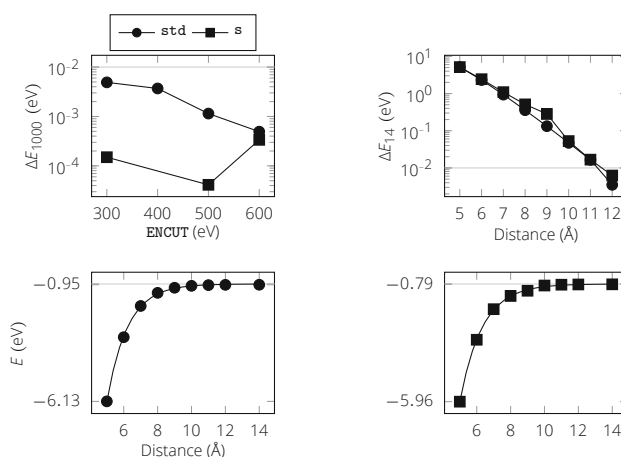
Figure 7.32: Top left: Energy cutoff convergence study for the available pseudopotentials for Thorium. Top right: Vacuum size convergence on the neutral atom. Bottom: same as top left but with an extrapolation.

Solid Thorium   At standard conditions, Th crystallizes into a fcc structure.
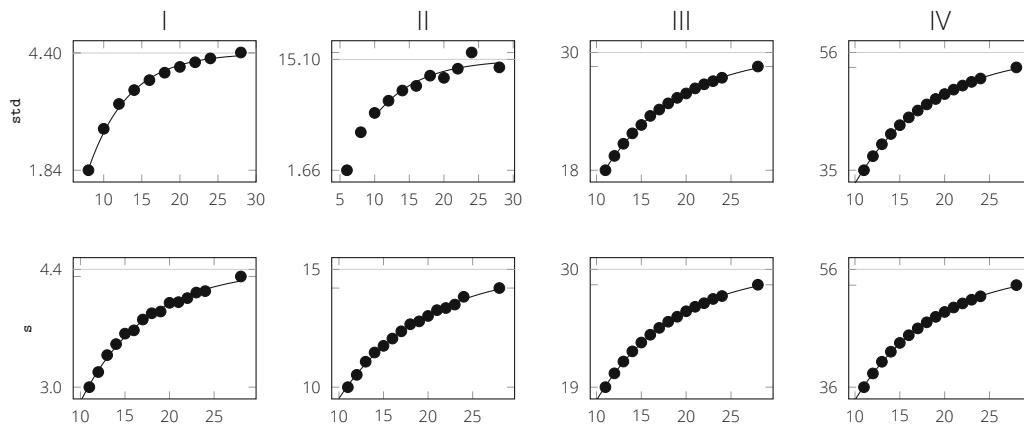
Figure 7.33: Vacuum convergence studies for ionized thorium atoms with both pseudopotentials. Extrapolated values are given at the top of the *y*-axis.

Ion	E_{VASP} (eV)	ΔE_{ref} (eV)	Ion	E_{VASP} (eV)	ΔE_{ref} (eV)
I	5.35	0.96	I	3.59	2.72
II	9.75	2.15	II	10.68	1.22
III	20.16	−0.16	III	15.05	4.95
IV	35.63	−6.83	IV	26.24	2.56

Table 7.44: Ionization Energies and comparison with the experimental values.[124] Left: `std`, Right: `s`-type pseudopotentials.
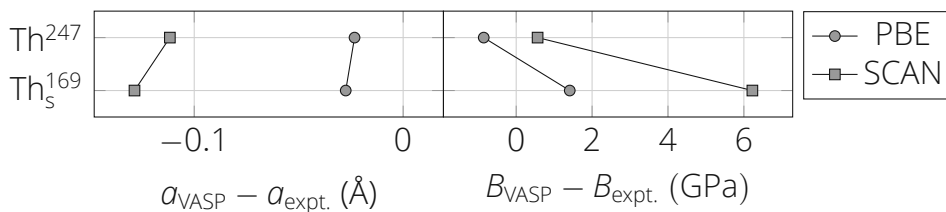
Figure 7.34: Difference in Lattice constant for the reference compared to the VASP calculation.[125,126]
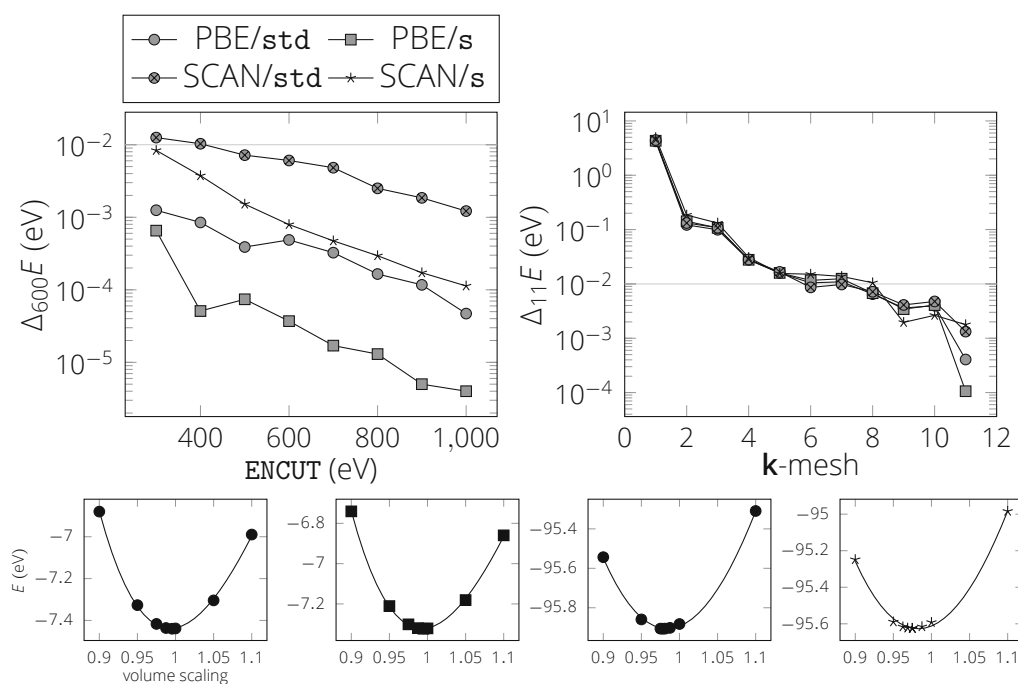
Figure 7.35: Convergence studies for solid Th. Top left: Energy cutoff convergence. Top right: k-mesh convergence. Bottom: Finding the DFT equilibrium volume where the calculations were done with PBE/std., PBE/s and SCAN/std, SCAN/s (from left to right).

A.6   Zinc Bromide

Zinc Bromide
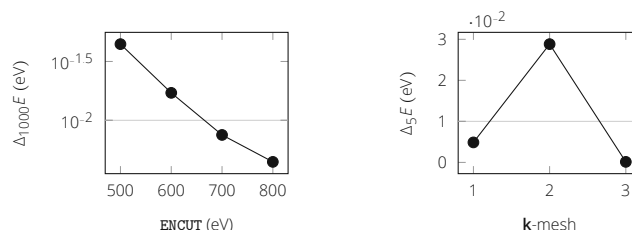
Figure 7.36: Convergence studies for $ZnBr_2$. Left: Energy cutoff convergence. Right: **k**-mesh convergence.

The electric quadrupole moment and nuclear spin of ^{81}Br and NQR spectra of $ZnBr_2$ with this isotope can be found in the literature,[127,128] which enables an experimental comparison of VASP's electric field gradient, since the NQR frequencies on ^{81}Br can be calculated as

$$\nu = \frac{eV_{zz}Q}{2h}\sqrt{1 + \frac{\eta^2}{3}}. \tag{7.6}$$

V_{zz} (V/Å^2)	η	ν (MHz)
−292.191	0.540	96.207
−293.584	0.530	96.509
−295.636	0.505	96.799
−297.335	0.492	97.161
−296.697	0.508	97.192
−297.466	0.501	97.338
−293.981	0.735	100.386
−293.709	0.739	100.376

Table 7.45: Unique electric field gradient values on Br positions for the experimental lattice parameters and calculated NQR frequencies for ^{81}Br. The experimental reference values are 81.425, 83.100 and 84.137 in units of MHz. The space group 142 of the $ZnBr_2$ crystal would allow four different Wyckoff positions for Br.

Description	N_A	N_e	**k**-mesh		ENCUT	EDIFF	ISMEAR	SIGMA	EDIFFG	ISPIN	Level
Figure 4.2	6	44	443	Γ	900	1e−7	0	0.1	0	1	SCAN
Figure 4.3	383	2056	111		500	1e−6	0	0.05	−1e−2	2	SCAN
Figure 5.2	12	96	999	MP	900	1e−6	0	0.01	0	2	PBE
Figure 5.3	3	24	999	MP	900	1e−6	0	0.01	0	2	PBE
Figure 5.3	3	24	999	MP	1000	1e−6	0	0.001	0	2	SCAN
Figure 5.3	3	24	555	MP	900	1e−6	0	0.01	0	2	HSE
Figure 5.4	326	2608	111		1000	1e−7	0	0.05	−1e−2	2	PBE
Figure 5.5	326	2608	111		1000	1e−10	0	0.05	−1e−5	2	PBE
Table 5.2	99	789	111		900	1e−6	0	0.2	−1e−2	2	PBE
Figure 5.8	326	2608	111		1000	1e−8	0	0.05	0	1	PBE
Figure 5.6	326	2608	111		1000	1e−10	0	0.05	0	2	PBE
Table 5.4	97	776	111		900	1e−7	0	0.1	−1e−2	2	PBE
Table 5.4	98	784	111		900	1e−7	0	0.1	−1e−2	2	PBE
Table 5.4	99	794	111		900	1e−6	0	0.2	−1e−4	2	PBE
Table 5.3	98	720	111		400	1e−6	0	0.001	0	2	HSE
Table 5.5	97	776	111		900	1e−7	0	0.1	−1e−2	2	PBE
Table 5.5	98	784	111		900	1e−9	0	0.1	0	2	PBE
Table 5.5	99	794	111		900	1e−6	0	0.2	0	2	HSE
Figure 6.2	18	112	221	Γ	900	1e−10	0	0.05	0	1	PBE
Table 6.1	71	456	111		900	1e−6	0	0.05	−1e−2	1	PBE
Table 6.2	71	456	111		900	1e−8	0	0.05	0	1	PBE

Table 7.46: The most relevant input parameters for a selection of calculations are listed in this table. In addition to this listing, we always set `LREAL=.FALSE.` and `PREC=A` and usually `LASPH = .TRUE.` and `GGA_COMPAT=.TRUE.` N_A is the total number of atoms (only approximately when describing multiple stoichiometries) and N_e the total number of electrons, which we used instead of the pseudopotential description for the sake of brevity. The **k**-mesh columns denote the number of grid points in *abc*-direction and Γ and MP stand for a Γ-centered grid or a Monkhorst-Pack[129] grid respectively. If the mesh size is 111, then a Γ-only calculation has been performed. When `EDIFFG` is listed as 0, no ionic relaxation has been performed.

Bibliography

[1] A. Derevianko and M. Pospelov. "Hunting for topological dark matter with atomic clocks". In: *Nature Physics* 10.12 (Nov. 2014), pp. 933–936. doi: 10.1038/nphys3137.

[2] P. G. Thirolf, B. Seiferle, and L. v. d. Wense. "Improving Our Knowledge on the 229mThorium Isomer: Toward a Test Bench for Time Variations of Fundamental Constants". In: *Annalen der Physik* 531.5 (2019), p. 1800381. doi: https://doi.org/10.1002/andp.201800381.

[3] V. V. Flambaum. "Enhanced Effect of Temporal Variation of the Fine Structure Constant and the Strong Interaction in ^{229}Th". In: *Phys. Rev. Lett.* 97 (9 Aug. 2006), p. 092502. doi: 10.1103/PhysRevLett.97.092502.

[4] G. E. Marti et al. "Imaging Optical Frequencies with 100μHz Precision and 1.1μm Resolution". In: *Phys. Rev. Lett.* 120 (10 Mar. 2018), p. 103201. doi: 10.1103/PhysRevLett.120.103201.

[5] C. J. Campbell et al. "Single-Ion Nuclear Clock for Metrology at the 19th Decimal Place". In: *Phys. Rev. Lett.* 108 (12 Mar. 2012), p. 120802. doi: 10.1103/PhysRevLett.108.120802.

[6] L. v. d. Wense and B. Seiferle. "The ^{229}Th isomer: prospects for a nuclear optical clock". In: *The European Physical Journal A* 56.11 (Nov. 2020). doi: 10.1140/epja/s10050-020-00263-0.

[7] T. Sikorsky et al. "Measurement of the ^{229}Th Isomer Energy with a Magnetic Microcalorimeter". In: *Phys. Rev. Lett.* 125 (14 Sept. 2020), p. 142503. doi: 10.1103/PhysRevLett.125.142503.

[8] *Magnesium Fluoride Optical Material*. accessed 2021-09-12. url: https://www.crystran.co.uk/optical-materials/magnesium-fluoride-mgf2.

[9] T. Tsujibayashi et al. "Spectral profile of the two-photon absorption co-efficients in CaF2 and BaF2". In: *Applied Physics Letters* 80.16 (2002), pp. 2883–2885. doi: 10.1063/1.1471939.

[10] G. W. Rubloff. "Far-Ultraviolet Reflectance Spectra and the Electronic Structure of Ionic Crystals". In: *Phys. Rev. B* 5 (2 Jan. 1972), pp. 662–684. doi: `10.1103/PhysRevB.5.662`.

[11] M. Kirm et al. "VUV spectroscopy of pure LiCaAlF6 crystals". In: *Nuclear Instruments and Methods in Physics Research Section A: Accelerators, Spectrometers, Detectors and Associated Equipment* 537.1 (2005). Proceedings of the 7th International Conference on Inorganic Scintillators and their Use in Scientific adn Industrial Applications, pp. 291–294. issn: 0168-9002. doi: `https://doi.org/10.1016/j.nima.2004.08.029`.

[12] T. Kozeki et al. "Observation of new excitation channel of cerium ion through highly vacuum ultraviolet transparent LiCAF host crystal". In: *Journal of Crystal Growth* 229.1 (2001). 1st Asian Conf. on Crystal Growth and Crystal Technology, pp. 501–504. issn: 0022-0248. doi: `https://doi.org/10.1016/S0022-0248(01)01217-9`.

[13] G. Kresse and J. Hafner. "Ab initio molecular dynamics for liquid metals". In: *Phys. Rev. B* 47 (1 Jan. 1993), pp. 558–561. doi: `10.1103/PhysRevB.47.558`.

[14] G. Kresse and J. Hafner. "Ab initio molecular-dynamics simulation of the liquid-metal–amorphous-semiconductor transition in germanium". In: *Phys. Rev. B* 49 (20 May 1994), pp. 14251–14269. doi: `10.1103/PhysRevB.49.14251`.

[15] G. Kresse and J. Furthmüller. "Efficiency of ab-initio total energy calculations for metals and semiconductors using a plane-wave basis set". In: *Computational Materials Science* 6.1 (1996), pp. 15–50. issn: 0927-0256. doi: `https://doi.org/10.1016/0927-0256(96)00008-0`.

[16] G. Kresse and J. Furthmüller. "Efficient iterative schemes for ab initio total-energy calculations using a plane-wave basis set". In: *Phys. Rev. B* 54 (16 July 1996), pp. 11169–11186. doi: `10.1103/PhysRevB.54.11169`.

[17] G. Kresse and D. Joubert. "From ultrasoft pseudopotentials to the projector augmented-wave method". In: *Phys. Rev. B* 59 (3 Jan. 1999), pp. 1758–1775. doi: `10.1103/PhysRevB.59.1758`.

[18] P. Villars and K. Cenzual, eds. *LiCaAlF6 Crystal Structure: Datasheet from "PAULING FILE Multinaries Edition – 2012" in SpringerMaterials*. Copyright 2016 Springer-Verlag Berlin Heidelberg & Material Phases Data System (MPDS), Switzerland & National Institute for Materials Science (NIMS), Japan. url: `https://materials.springer.com/isp/crystallographic/docs/sd_0310383`.

[19] Jörg Behler. "Constructing high-dimensional neural network potentials: A tutorial review". In: *International Journal of Quantum Chemistry* 115.16 (2015), pp. 1032–1050. doi: `https://doi.org/`10.1002/`qua.`24890.

[20] B. S. Nickerson et al. "Driven electronic bridge processes via defect states in [229]Th-doped crystals". In: *Phys. Rev. A* 103 (5 May 2021), p. 053120. doi: 10.1103/`PhysRevA.`103.053120.

[21] B. S. Nickerson et al. "Nuclear Excitation of the [229]Th Isomer via Defect States in Doped Crystals". In: *Phys. Rev. Lett.* 125 (3 July 2020), p. 032501. doi: 10.1103/`PhysRevLett.`125.032501.

[22] *The Nobel Prize in Physics 1914*. accessed 2020-03-02. url: `https://www.nobelprize.org/prizes/physics/`1914`/summary/`.

[23] *The Nobel Prize in Physics 1915*. accessed 2020-03-02. url: `https://www.nobelprize.org/prizes/physics/`1915`/summary/`.

[24] A.F. Wells. *Structural Inorganic Chemistry*. 4th ed. Clarendon Press, 1975. Chap. 1, p. 4. isbn: 9780198553540.

[25] R. Gross and A. Marx. *Festkörperphysik*. 1st ed. Oldenbourg Wissenschaftsverlag, 2012. Chap. 8, pp. 335–352. isbn: 9783486712940.

[26] N.W. Ashcroft and N.D. Mermin. *Solid State Physics*. 1st ed. Cengage Learning, 1976. Chap. 8, pp. 131–141. isbn: 9780030839931.

[27] N.W. Ashcroft and N.D. Mermin. *Solid State Physics*. 1st ed. Cengage Learning, 1976. Chap. 9, pp. 151–162. isbn: 9780030839931.

[28] Peter Hadley. *Empty lattice approximation for a face centered cubic crystal*. accessed 2021-01-16. url: `http://lampx.tugraz.at/~hadley/ss`1`/empty/dispfcc.html?`.

[29] Harald Ibach and Hans Lüth. *Solid-State Physics*. 4th ed. Springer-Verlag Berlin Heidelberg, 2009. Chap. 7, pp. 159–167. isbn: 978-3-540-93803-3. doi: 10.1007/`978-3-540-93804-0`.

[30] Feliciano Giustino. *Materials modeling using Density Functional Theory*. 1st ed. Oxford University Press, 2014. Chap. 1, pp. 1–18. isbn: ISBN 978–0–19–966244–9.

[31] Eberhard Engel and Reiner M. Dreizler. *Density Functional Theory*. 1st ed. Springer-Verlag Berlin Heidelberg, 2011. Chap. 1, pp. 1–5. isbn: 978-3-642-14089-1.

[32] Anatole von Lilienfeld. *Quantum Machine Learning*. 2017. url: `https://www.youtube.com/watch?v=gxeSGRo`8`XFU`.

[33] Wolfram Koch and Max C. Holthausen. *A Chemist's Guide to Density Functional Theory*. 2nd ed. Wiley-VCH Verlag GmbH, 2001, pp. VII–X. isbn: 3-527-30372-3.

[34] Axel D. Becke. "Perspective: Fifty years of density-functional theory in chemical physics". In: *The Journal of Chemical Physics* 140.18 (2014). doi: `10.1063/1.4869598`. eprint: `https://doi.org/10.1063/1.4869598`.

[35] *The Nobel Prize in Physics 1998*. accessed 2021-01-18. url: `https://www.nobelprize.org/prizes/chemistry/1998/summary/`.

[36] P. Hohenberg and W. Kohn. "Inhomogeneous Electron Gas". In: *Phys. Rev.* 136 (3B Nov. 1964), B864–B871. doi: `10.1103/PhysRev.136.B864`.

[37] Klaus Capelle. *A bird's-eye view of density-functional theory*. 2002. url: `https://arxiv.org/abs/cond-mat/0211443`.

[38] M. Born and R. Oppenheimer. "Zur Quantentheorie der Molekeln". In: *Annalen der Physik* 389.20 (1927), pp. 457–484. doi: `https://doi.org/10.1002/andp.19273892002`. eprint: `https://onlinelibrary.wiley.com/doi/pdf/10.1002/andp.19273892002`.

[39] *Libxc - a library of exchange-correlation functionals for density-functional theory*. accessed: 2021-02-016. url: `https://www.tddft.org/programs/libxc/functionals/`.

[40] Susi Lehtola et al. "Recent developments in libxc – A comprehensive library of functionals for density functional theory". In: *SoftwareX* 7 (2018), pp. 1–5. issn: 2352-7110. doi: `https://doi.org/10.1016/j.softx.2017.11.002`.

[41] Volker Eyert. *Electronic Structure of Crystalline Materials*. 2008. url: `http://myweb.rz.uni-augsburg.de/~eyert/esocs.shtml`.

[42] Martin Pimon. "VASP Simulation of Thorium doped Magnesium Fluoride". MA thesis. TU Wien, 2017, pp. 10–16.

[43] R. Gross and A. Marx. *Festkörperphysik*. 1st ed. Oldenbourg Wissenschaftsverlag, 2012. Chap. 5, pp. 177–196. isbn: 9783486712940.

[44] Peter Hadley. *1-d chain of atoms*. accessed: 2021-02-02. url: `http://lampx.tugraz.at/~hadley/ss1/phonons/1d/1dphonons.php`.

[45] M. Bartelmann et al. *Theoretische Physik*. Springer-Verlag Berlin Heidelberg, 2015. Chap. 6, pp. 233–234. doi: `10.1007/978-3-642-54618-1`.

[46] Peter Hadley. *1-d chain of atoms with two different masses*. accessed: 2021-02-02. url: `http://lampx.tugraz.at/~hadley/ss1/phonons/1d/1d2m.php`.

[47] Mike Peel. *Lattice Dynamics*. accessed: 2021-02-03. url: `http://www.mikepeel.net/physics/mphys/pc3352/3.%5C%20Lattice%5C%20Dynamics.pdf`.

[48] *6th order polynomial equation*. accessed 2021-03-16. url: `https://www.algebra-equation.com/solving-algebra-equation/graphing-inequalities/6th-order-polynomial-equation.html%5C#c=simplify_algstepssimplify%5C&v217=w%5C%255E6%5C%2520%5C%2B%5C%2520aw%5C%255E4%5C%2520%5C%2B%5C%2520bw%5C%255E2%5C%2520%5C%2B%5C%2520c%5C%2520%5C%253D%5C%25200%5C&v218=w`.

[49] Otfried Madelung. *Festkörpertheorie I*. Vol. 1. Springer-Verlag Berlin Heidelberg, 1972. Chap. 31, pp. 120–123. isbn: 3-540-05731-5.

[50] J. Rennie. *What is it about the "conduction band" of a material that is distinct from the valence band?* accessed: 2021-02-01, version: 2016-07-04. url: `https://physics.stackexchange.com/q/266119`.

[51] N.W. Ashcroft and N.D. Mermin. *Solid State Physics*. 1st ed. Cengage Learning, 1976. Chap. 19, pp. 376–379. isbn: 9780030839931.

[52] A.D. Franklin. "Statistical Thermodynamics of Point Defects in Crystals". In: *Point Defects in Solids*. Ed. by James H. Crawford Jr and Lawrence M. Slifkin. 1st ed. Vol. 1. Plenum Press. Chap. 1, p. 1. isbn: 978-1-4684-2972-5.

[53] Attila Szabo and Neil S. Ostlund. "Modern Quantum Chemistry". In: (1996), p. 231.

[54] Otfried Madelung. *Festkörpertheorie I*. Vol. 1. Springer-Verlag Berlin Heidelberg, 1972. Chap. 3, pp. 10–19. isbn: 3-540-05731-5.

[55] Attila Szabo and Neil S. Ostlund. "Modern Quantum Chemistry". In: (1996), pp. 108–119.

[56] Peter Mohn. *Magnetism in the Solid State*. 2nd ed. Springer-Verlag Berlin Heidelberg New York, 2006. Chap. 17, pp. 161–162.

[57] Otfried Madelung. *Festkörpertheorie I*. Vol. 1. Springer-Verlag Berlin Heidelberg, 1972. Chap. 11, pp. 39–45. isbn: 3-540-05731-5.

[58] Walter Grimus. *Einführung in die Statistische Physik und Thermodynamik*. Oldenbourg Verlag München, 2010. Chap. 4, p. 76. isbn: 978-3-486-70205-7.

[59] N.W. Ashcroft and N.D. Mermin. *Solid State Physics*. 1st ed. Cengage Learning, 1976. Chap. 2, pp. 29–36. isbn: 9780030839931.

[60] D. M. Ceperley and B. J. Alder. "Ground State of the Electron Gas by a Stochastic Method". In: *Phys. Rev. Lett.* 45 (7 1980), pp. 566–569. doi: 10.1103/PhysRevLett.45.566.

[61] Teepanis Chachiyo. "Communication: Simple and accurate uniform electron gas correlation energy for the full range of densities". In: *The Journal of Chemical Physics* 145.2 (2016), p. 021101. doi: 10.1063/1.4958669.

[62] John P. Perdew, Kieron Burke, and Matthias Ernzerhof. "Generalized Gradient Approximation Made Simple". In: *Phys. Rev. Lett.* 77 (18 Oct. 1996), pp. 3865–3868. doi: 10.1103/PhysRevLett.77.3865.

[63] Jianwei Sun, Adrienn Ruzsinszky, and John P. Perdew. "Strongly Constrained and Appropriately Normed Semilocal Density Functional". In: *Phys. Rev. Lett.* 115 (3 July 2015), p. 036402. doi: 10.1103/PhysRevLett.115.036402.

[64] J. Heyd, G. E. Scuseria, and M. Ernzerhof. "Hybrid functionals based on a screened Coulomb potential". In: *The Journal of Chemical Physics* 118.18 (2003), pp. 8207–8215. doi: 10.1063/1.1564060.

[65] D. J. Singh and Lars Nordström. *Planewaves, Pseudopotentials and the LAPW Method*. Springer US, 2006. doi: 10.1007/978-0-387-29684-5.

[66] P. E. Blöchl. "Projector augmented-wave method". In: *Phys. Rev. B* 50 (24 Dec. 1994), pp. 17953–17979. doi: 10.1103/PhysRevB.50.17953.

[67] P. Schwerdtfeger. "The Pseudo-potential Approximation in Electronic Structure Theory". In: *ChemPhysChem* 12.17 (2011), pp. 3143–3155. doi: 10.1002/cphc.201100387.

[68] Giuseppe Carleo et al. "Machine learning and the physical sciences". In: *Rev. Mod. Phys.* 91 (4 Dec. 2019), p. 045002. doi: 10.1103/RevModPhys.91.045002.

[69] 3Blue1Brown. *Neural networks*. accessed: 2021-02-16. url: https://youtube.com/playlist?list=PLZHQObOWTQDNU6R1_67000Dx_ZCJB-3pi.

[70] "wACSF–Weighted atom-centered symmetry functions as descriptors in machine learning potentials". In: *The Journal of Chemical Physics* 148.24 (2018). doi: 10.1063/1.5019667.

[71] *Sellaite*. accessed 2021-09-12. url: https://en.wikipedia.org/wiki/Sellaite.

[72] W. M. Haynes, ed. *CRC Handbook of Chemistry and Physics*. Ed. by David R. Lide. Ed. by Thomas J. Bruno. 97th ed. CRC Press, 2017. Chap. 4, p. 144. isbn: 9781498754293.

[73] P. Villars and K. Cenzual, eds. *MgF2 Crystal Structure: Datasheet*. Copyright 2016 Springer-Verlag Berlin Heidelberg & Material Phases Data System (MPDS), Switzerland & National Institute for Materials Science (NIMS), Japan. url: `https://materials.springer.com/isp/crystallographic/docs/sd_`1924933.

[74] L. J. Sham and M. Schlüter. "Density-Functional Theory of the Energy Gap". In: *Phys. Rev. Lett.* 51 (20 Nov. 1983), pp. 1888–1891. doi: 10.1103`/PhysRevLett.`51.1888`.

[75] J. P. Perdew and M. Levy. "Physical Content of the Exact Kohn-Sham Orbital Energies: Band Gaps and Derivative Discontinuities". In: *Phys. Rev. Lett.* 51 (20 Nov. 1983), pp. 1884–1887. doi: 10.1103`/PhysRevLett.`51.1884.

[76] G. Michalicek. *Why does Density Functional Theory (DFT) underestimate bandgaps?* Physics Stack Exchange. accessed 2021-03-28). url: `https://physics.stackexchange.com/q/`360454.

[77] R. W. Godby, M. Schlüter, and L. J. Sham. "Self-energy operators and exchange-correlation potentials in semiconductors". In: *Phys. Rev. B* 37 (17 June 1988), pp. 10159–10175. doi: 10.1103`/PhysRevB.`37.10159.

[78] Z. H. Levine and D. C. Allan. "Linear optical response in silicon and germanium including self-energy effects". In: *Phys. Rev. Lett.* 63 (16 Oct. 1989), pp. 1719–1722. doi: 10.1103`/PhysRevLett.`63.1719.

[79] W. M. Haynes, ed. *CRC Handbook of Chemistry and Physics*. Ed. by David R. Lide. Ed. by Thomas J. Bruno. 97th ed. CRC Press, 2017. Chap. 5, p. 1. isbn: 9781498754293.

[80] J. B. Barker. "Oxidation State of ^{229}Th Recoils Implanted into MgF_2 Crystals". In: *Science Journal of Chemistry* 6 (Jan. 2018), p. 66. doi: 10.11648`/j.sjc.`20180604.15.

[81] M. Pimon et al. "DFT calculation of 229thorium-doped magnesium fluoride for nuclear laser spectroscopy". In: *Journal of Physics: Condensed Matter* 32.25 (Apr. 2020), p. 255503. doi: 10.1088`/1361-648x/ab7c`90.

[82] P. Villars and K. Cenzual, eds. *CaF2 Crystal Structure: Datasheet*. Copyright 2016 Springer-Verlag Berlin Heidelberg & Material Phases Data System (MPDS), Switzerland & National Institute for Materials Science (NIMS), Japan. url: `https://materials.springer.com/isp/crystallographic/docs/sd_`0378096.

[83]   G. Chiarotti. *1.6 Crystal structures and bulk lattice parameters of materials quoted in the volume: Datasheet from Landolt-Börnstein - Group III Condensed Matter · Volume 24B: "Electronic and Vibrational Properties" in SpringerMaterials*. Ed. by G. Chiarotti. Copyright 1994 Springer-Verlag Berlin Heidelberg. doi: 10.1007/10086058_6.

[84]   M. Jaccaud et al. "Fluorine". In: *Ullmann's Encyclopedia of Industrial Chemistry*. American Cancer Society, 2000. isbn: 9783527306732. doi: https://doi.org/10.1002/14356007.a11_293.

[85]   *Electronegativities of the elements (data page)*. accessed 2021-03-24. url: https://en.wikipedia.org/wiki/Electronegativities_of_the_elements_(data_page).

[86]   N. N. Greenwood and A. Earnshaw. *Chemistry of the Elements*. 2nd ed. Butterworth-Heinemann, 1997. Chap. 2, p. 28.

[87]   *Oxidation State*. accessed 2021-10-04. url: https://en.wikipedia.org/wiki/Oxidation_state#List_of_oxidation_states_of_the_elements.

[88]   P. Dessovic et al. "229Thorium-doped calcium fluoride for nuclear laser spectroscopy". In: *Journal of Physics: Condensed Matter* 26.10 (Feb. 2014), p. 105402. doi: 10.1088/0953-8984/26/10/105402.

[89]   S. Stellmer et al. "Attempt to optically excite the nuclear isomer in [229]Th". In: *Phys. Rev. A* 97 (6 June 2018), p. 062506. doi: 10.1103/PhysRevA.97.062506.

[90]   T. D. Kühne et al. "CP2K: An electronic structure and molecular dynamics software package - Quickstep: Efficient and accurate electronic structure calculations". In: *The Journal of Chemical Physics* 152.19 (2020), p. 194103. doi: 10.1063/5.0007045.

[91]   Q. Sun et al. "PySCF: the Python-based simulations of chemistry framework". In: *WIREs Computational Molecular Science* 8.1 (2018), e1340. doi: https://doi.org/10.1002/wcms.1340.

[92]   Q. Sun et al. "Recent developments in the PySCF program package". In: *The Journal of Chemical Physics* 153.2 (2020), p. 024109. doi: 10.1063/5.0006074.

[93]   J. J. Mortensen, L. B. Hansen, and K. W. Jacobsen. "Real-space grid implementation of the projector augmented wave method". In: *Phys. Rev. B* 71 (3 Jan. 2005), p. 035109. doi: 10.1103/PhysRevB.71.035109.

[94] J. Enkovaara et al. "Electronic structure calculations with GPAW: a real-space implementation of the projector augmented-wave method". In: *Journal of Physics: Condensed Matter* 22.25 (June 2010), p. 253202. doi: 10.1088/0953-8984/22/25/253202.

[95] R. M. Feenstra and M. Widom. *WaveTrans*. accessed: 2021-10-05. url: https://www.andrew.cmu.edu/user/feenstra/wavetrans/.

[96] A Togo and I Tanaka. "First principles phonon calculations in materials science". In: *Scr. Mater.* 108 (Nov. 2015), pp. 1–5.

[97] W. M. Haynes, ed. *CRC Handbook of Chemistry and Physics*. Ed. by David R. Lide. Ed. by Thomas J. Bruno. 97th ed. CRC Press, 2017. Chap. 11, pp. 1–172. isbn: 9781498754293.

[98] Alexander Haas. "VASP Simulation of Thorium doped Magnesium Fluoride". MA thesis. TU Wien, 2020, p. 33.

[99] C. Lee, W. Yang, and R. G. Parr. "Development of the Colle-Salvetti correlation-energy formula into a functional of the electron density". In: *Phys. Rev. B* 37 (2 Jan. 1988), pp. 785–789. doi: 10.1103/PhysRevB.37.785.

[100] A. D. Becke. "Density-functional exchange-energy approximation with correct asymptotic behavior". In: *Phys. Rev. A* 38 (6 Sept. 1988), pp. 3098–3100. doi: 10.1103/PhysRevA.38.3098.

[101] S. H. Vosko, L. Wilk, and M. Nusair. "Accurate spin-dependent electron liquid correlation energies for local spin density calculations: a critical analysis". In: *Canadian Journal of Physics* 58.8 (1980), pp. 1200–1211. doi: 10.1139/p80-159.

[102] J. P. Perdew, M. Ernzerhof, and K. Burke. "Rationale for mixing exact exchange with density functional approximations". In: *The Journal of Chemical Physics* 105.22 (1996), pp. 9982–9985. doi: 10.1063/1.472933.

[103] M. A. Dubinskii et al. "Active Medium for All-Solid-State Tunable UV Laser". In: *Advanced Solid State Lasers*. OSA, 1993. doi: 10.1364/assl.1993.lm5.

[104] W. G. Rellergert et al. "Progress towards fabrication of229Th-doped high energy band-gap crystals for use as a solid-state optical frequency reference". In: *IOP Conference Series: Materials Science and Engineering* 15 (Nov. 2010), p. 012005. doi: 10.1088/1757-899x/15/1/012005.

[105] A. Jain et al. "Commentary: The Materials Project: A materials genome approach to accelerating materials innovation". In: *APL Materials* 1.1 (2013), p. 011002. doi: 10.1063/1.4812323.

[106] Adam Paszke et al. "PyTorch: An Imperative Style, High-Performance Deep Learning Library". In: *Advances in Neural Information Processing Systems 32*. Ed. by H. Wallach et al. Curran Associates, Inc., 2019, pp. 8024–8035. url: `http://papers.neurips.cc/paper/9015-pytorch-an-imperative-style-high-performance-deep-learning-library.pdf`.

[107] hobs (https://stats.stackexchange.com/users/15974/hobs). *How to choose the number of hidden layers and nodes in a feedforward neural network?* Cross Validated. accessed: 2021-10-07, version: 2021-05-05. url: `https://stats.stackexchange.com/q/`136542.

[108] G. Klambauer et al. "Self-Normalizing Neural Networks". In: *CoRR* (2017). url: `http://arxiv.org/abs/`1706.02515.

[109] T. Takeda. "The scalar relativistic approximation". In: *Zeitschrift für Physik B Condensed Matter and Quanta* 32.1 (Mar. 1978), pp. 43–48. doi: 10.1007/`bf`01322185.

[110] R. Gross and A. Marx. *Festkörperphysik*. 1st ed. Oldenbourg Wissenschaftsverlag, 2012. Chap. 4, pp. 161–164. isbn: 9783486712940.

[111] W. M. Haynes, ed. *CRC Handbook of Chemistry and Physics*. Ed. by David R. Lide. Ed. by Thomas J. Bruno. 97th ed. CRC Press, 2017. Chap. 12, pp. 16–19. isbn: 9781498754293.

[112] W. M. Haynes, ed. *CRC Handbook of Chemistry and Physics*. Ed. by David R. Lide. Ed. by Thomas J. Bruno. 97th ed. CRC Press, 2017. Chap. 9, p. 23. isbn: 9781498754293.

[113] W. M. Haynes, ed. *CRC Handbook of Chemistry and Physics*. Ed. by David R. Lide. Ed. by Thomas J. Bruno. 97th ed. CRC Press, 2017. Chap. 9, p. 75. isbn: 9781498754293.

[114] W. M. Haynes, ed. *CRC Handbook of Chemistry and Physics*. Ed. by David R. Lide. Ed. by Thomas J. Bruno. 97th ed. CRC Press, 2017. Chap. 10, p. 147. isbn: 9781498754293.

[115] W. M. Haynes, ed. *CRC Handbook of Chemistry and Physics*. Ed. by David R. Lide. Ed. by Thomas J. Bruno. 97th ed. CRC Press, 2017. Chap. 9, p. 27. isbn: 9781498754293.

[116] P. Villars and K. Cenzual, eds. *MgO Crystal Structure: Datasheet*. Copyright 2016 Springer-Verlag Berlin Heidelberg & Material Phases Data System (MPDS), Switzerland & National Institute for Materials Science (NIMS), Japan. url: `https://materials.springer.com/isp/crystallographic/docs/sd_`0561181.

[117] W. M. Haynes, ed. *CRC Handbook of Chemistry and Physics*. Ed. by David R. Lide. Ed. by Thomas J. Bruno. 97th ed. CRC Press, 2017. Chap. 12, pp. 36–37. isbn: 9781498754293.

[118] W. M. Haynes, ed. *CRC Handbook of Chemistry and Physics*. Ed. by David R. Lide. Ed. by Thomas J. Bruno. 97th ed. CRC Press, 2017. Chap. 10, p. 204. isbn: 9781498754293.

[119] Jr. Chase M. W. "NIST-JANAF Thermochemical Tables, Fourth Edition". In: *J. Phys. Chem. Ref. Data, Monograph 9* (1998).

[120] P. Villars and K. Cenzual, eds. *LiAl Crystal Structure: Datasheet*. Copyright 2016 Springer-Verlag Berlin Heidelberg & Material Phases Data System (MPDS), Switzerland & National Institute for Materials Science (NIMS), Japan. url: `https://materials.springer.com/isp/crystallographic/docs/sd_`1215789.

[121] P. Villars and K. Cenzual, eds. *Al3Li (LiAl3 rt) Crystal Structure: Datasheet*. Copyright 2016 Springer-Verlag Berlin Heidelberg & Material Phases Data System (MPDS), Switzerland & National Institute for Materials Science (NIMS), Japan. url: `https://materials.springer.com/isp/crystallographic/docs/sd_`0455391.

[122] P. Villars and K. Cenzual, eds. *Li3Al2 Crystal Structure: Datasheet*. Copyright 2016 Springer-Verlag Berlin Heidelberg & Material Phases Data System (MPDS), Switzerland & National Institute for Materials Science (NIMS), Japan. url: `https://materials.springer.com/isp/crystallographic/docs/sd_`1251359.

[123] W. M. Haynes, ed. *CRC Handbook of Chemistry and Physics*. Ed. by David R. Lide. Ed. by Thomas J. Bruno. 97th ed. CRC Press, 2017. Chap. 4, p. 114. isbn: 9781498754293.

[124] W. M. Haynes, ed. *CRC Handbook of Chemistry and Physics*. Ed. by David R. Lide. Ed. by Thomas J. Bruno. 97th ed. CRC Press, 2017. Chap. 10, p. 205. isbn: 9781498754293.

[125] *CRC Handbook of Chemistry and Physics, 97th Edition*. CRC Press, 2017. isbn: 1482208679.

[126] P. E. Armstrong, O. N. Carlson, and J. F. Smith. "Elastic Constants of Thorium Single Crystals in the Range 77–400°K". In: *Journal of Applied Physics* 30.1 (Jan. 1959), pp. 36–41. doi: 10.1063/1.1734971.

[127] T.J. Bastow and H.J. Whitfield. "Bromine nuclear quadrupole resonance in zinc bromide and in lead bromide". In: *Australian Journal of Chemistry* 27.7 (1974), p. 1397. doi: 10.1071/ch9741397.

[128]   W. M. Haynes, ed. *CRC Handbook of Chemistry and Physics*. Ed. by David R. Lide. Ed. by Thomas J. Bruno. 97th ed. CRC Press, 2017. Chap. 11, p. 31. isbn: 9781498754293.

[129]   H. J. Monkhorst and J. D. Pack. "Special points for Brillouin-zone integrations". In: *Phys. Rev. B* 13 (12 June 1976), pp. 5188–5192. doi: `10.1103/PhysRevB.13.5188`.